공학박사 학위논문

Electrokinetic Transport of DNA in Structurally/Chemically Modified Solid-State Nanopore

구조적/화학적으로 변형된 솔리드 스테이트 나노포어에서 DNA의 전기동역학적 수송에 관한 연구

2020년 2월

서울대학교 대학원

재료공학부

이 기 단

Electrokinetic Transport of DNA in Structurally/Chemically Modified Solid-State Nanopore

지도 교수 김 기 범

이 논문을 공학박사 학위논문으로 제출함

2020년 2월

서울대학교 대학원

재료공학부

이 기 단

이기단의 공학박사 학위논문을 인준함

2020년 2월

위 원 장 도 준 상 (인)

부위원장 김 기 범 (인)

위 원 김 성 재 (인)

위 원 이 태 걸 (인)

위 원 이 재 훈 (인)

Abstract

Electrokinetic Transport of DNA in Structurally/Chemically Modified Solid-State Nanopore

Lee Kidan
Department of Materials Science and Engineering
The Graduate School
Seoul National University

In this thesis, the current issues in solid-state nanopore and were discussed and electrokinetic approaches to the issues were introduced with physical analysis on the DNA transport through the nanopores. The active subfields of solid-state nanopore research include (1) enhancing DNA sensitivity, (2) improving the reliability of the device, and (3) searching for a new biotechnological application of solid-state nanopore or fabricated nanoporous structures other than electrical sensing. The previous studies on the subjects were summarized in the thesis, with the state-of-art improvements on the electrical noise properties of the nanopore devices. Nevertheless, the reports mainly were based on simple and empirical ideas to examine the raised issues, thus the research field still required more systematic and physical approaches to improve the performance of the solid-state nanopore platform.

First, to enhance the DNA sensitivity of the device, a structural modification named 'guide structure' was introduced to the nanopore device. Further, the effect of the inserted structure on DNA translocations was systematically analyzed in electrokinetics simulations using the finite element method. The goal of improving DNA sensitivity was to increase the translocation signal magnitude (ΔG) and duration (t_d) of DNA molecules. ΔG was increased in the presence of the guide structure, which geometrically hindered the ionic movement with the DNA segments in the guide structure waiting

for translocation. The simulations identified a strong electroosmotic flow inside the guide structure in the opposite direction to the translocation, and the fluid flow acted as an extra drag on the remaining DNA parts to slow down its translocation.

Secondly, as an advanced approach to the device reliability over the previous reports, plasma polymerization of poly(ethylene glycol) (PEG) was selected to prepare the polymeric coating on the nanopore membrane instead of the liquid phase self-assembly method. The gas-phase deposition was well known for its advantages in fabrication efficiency, controllability, and reproducibility over the self-assembly method. To assess the anti-DNA adsorption properties of the plasma-polymerized PEG (PP-PEG) and the bare silicon nitride (SiN_x) surface in consideration of actual nanopore experiment situations, time to adsorption concept was designed and compared on the two surfaces. As a result, the functionalized surface was stable against DNA adsorptions for ~2 times longer time than the bare surface. The repulsive interaction between PP-PEG and DNA affected to the increased reliability, and induced changes in DNA translocation behaviors that exhibited fast translocations of fully stretched molecules. In addition, a physical and microscopic analysis of the DNA adsorption onto the nanopore surface was conducted, considering the interaction between the surface and DNA.

Thirdly, the electrophoretic nucleic acid preparation method was introduced, which was derived from the electrical translocations of DNA through solid-state nanopores. In the new application, nucleic acids from a biosample were allowed to pass through a fabricated nanoporous structure, nanofilter membrane, when other molecules with positive charges or sizes larger than the nanoporous structure stayed in the biosample. After establishing the system to realize the physical idea, the principle and the stability of the electrophoretic operation were confirmed in the electrical transport experiment of microRNA. Further, the clinical applicability of the electrophoretic preparation system was validated by demonstrating liquid biopsy process with clinical human blood serum.

The analysis provided physical and structural understandings and application of the electrokinetic DNA transports in solid-state nanopore and its derived platform. Conversely, from this thesis, it was made clear that analyzing the physical contributions to DNA translocations was a key to systematic manipulations and improvements to the solid-state nanopore performances.

Keyword : solid-state nanopore, nanofilter membrane, electrokinetics, DNA translocation, antifouling membrane, nucleic acid preparation
Student Number : 2013-20612

Table of Contents

List of Figures

Chapter 1 Introduction

List of Tables

Chapter 4 Development and Clinical Application of Electrophoretic Nucleic Acid Preparation System using Nanofilter Membrane Device

Chapter 1

Introduction

1.1 Introduction to Solid-State Nanopore and Nanofilter Platforms

Nanopore is an emerging high-throughput single-molecular biosensing technology, of which the detection target includes DNA, RNA, protein, DNA-protein and protein-protein complexes, and small organic molecules.[1-5] When a bias voltage is applied across a membrane of a nanometer-scale thickness with a few nanometers-large pore embedded, an electrically charged biomolecule is drawn to the nanopore region to pass through the short channel. The passage or translocation of a biomolecule is detected as an electrical signal which carries the physical information of the translocating biomolecule including the size and the electrical charge of the molecule.[6, 7]

Figure 1-1 depicts 2 classes of nanopores: biological nanopore and solid-state nanopore. The nanopore was first introduced in 1996 by Kasianowicz, Brandin, Branton, and Deamer.[8] This first nanopore was constructed using lipid bilayer and alpha(α)-hemolysin, both are organic materials found in biology. Specifically, α-hemolysin is a toxin protein secreted by *Staphylococcus aureus*, which is a protein channel embedded in the membrane of a victim cell to bring inner cell components out of the cell and eventually to kill it.[8, 9] In the nanopore application, the molecular transport path was used as a channel confinement for the target molecule of detection.

Based on the protein channel structure with fine confinement in ~1 nm scale, the biological nanopore has demonstrated high sensitivity and a high throughput in single-stranded DNA (ssDNA) detection.[8, 10] Nevertheless, the platform had a low versatility of target biomolecules from the fixed dimensions of the confining channel.[5] In addition, the lipid bilayer membrane was extremely vulnerable to fracture, making the handling of the device very difficult.

To overcome the drawbacks of the biological nanopore, solid-state nanopore was first reported individually in 2001 (nanopore fabricated using focused ion beam (FIB))[11] and 2003 (fabricated using transmission electron microscope (TEM)).[12] The

design of the fabricated platform was inspired by the structure of its biological counterpart and created as a ~20-nm thick silicon nitride (SiN_x) freestanding membrane supported by silicon (Si) substrate, with a ~5-nm nanopore connecting both sides of the membrane. The direct perforation method enabled sculpting of the nanopore, widening the detection target of the nanopore to double-strand DNA (dsDNA), protein, DNA-protein complex, protein-protein complex, and small molecules. Moreover, the robust materials greatly enhanced the mechanical stability of the device compared to the biological nanopores.[5]

For almost 2 decades after the first appearance, the solid-state nanopore was studied in various aspects including device fabrication, electrical characterization of the device, improvements on the detection performances, and specific applications of the platform. In the rest of the introduction chapter, the previous works will be briefly summarized and the current issues in the solid-state nanopore field will be discussed. Extending the discussions on the single nanopore devices further, the significance and the emergence of multiple-nanopore structure will be addressed as an introduction to the nanofilter platform. First of all, the principle of the nanopore detection will be explained as the basis of the introductory discussions mentioned.

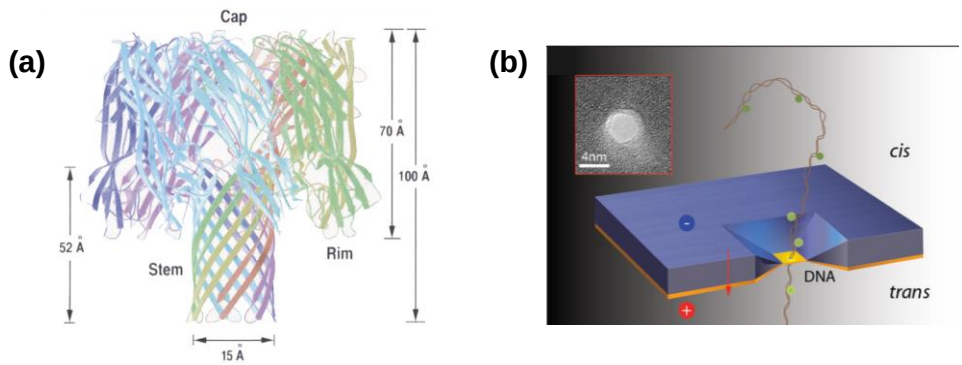

Figure 1-1 Schematics of the nanopores: biological nanopore and solid-state nanopore. (a) biological nanopore (α-hemolysin) embedded in a lipid bilayer, with the narrowest confinement at the boundary of vestibule and β-barrel. (b) solid-state nanopore device with a DNA molecule translocating through a nanopore in the membrane. The inset is a TEM image of a nanopore of 4 nm diameter. Figures were adapted with permission from (a) ref.[13], Copyright 2006 Elsevier Ltd. All rights reserved; (b) ref.[14]. Copyright 2016 American Chemical Society.

1.2 Principle of Biomolecule Detection in Nanopore based on Electrokinetic Transport

Figure 1−2 illustrates the fundamental principle of biomolecular detection in nanopore devices. The physical principle works the same in both the biological and the solid−state nanopores.

On the left of Figure 1−2, an electrolyte is filled in 2 chambers (named *cis* and *trans*) separated by the membrane and a nanopore. Driven by an external voltage across the membrane, an ionic conductance can be detected from the ionic flow generated inside the nanopore. The ionic current is constant over time with a finite noise of the current baseline, which will be discussed in section 1.4.

On the right of Figure 1−2, negatively charged DNA molecules are injected into the *cis* chamber and a positive bias voltage is applied at the opposite chamber. Therefore, the molecules are forced by the electric field to move to the *trans* chamber. From the small pore size comparable to the cross−section diameter of DNA, the charged biomolecules can only translocate through the nanopore one molecule at a time. The ionic flow through the nanopore is temporarily and partly blocked by the translocating DNA. This situation is detected as a current drop peak in the current (I)−time (t) recordings of the nanopore ionic current.

Information on a translocation peak signal, the magnitude (ΔI) and the duration (dwell time or t_d) of the current drop, implies the physical characteristics of the translocating molecule. ΔI is directly related to the volume fraction that the molecule occupies in the nanopore during translocation. As in Figure 3, the relationship between the molecular size and ΔI can be modeled using Ohm's law and assuming that the nanopore and the translocating molecule are a cylindrical resistor and a hard cylinder, respectively. The baseline ionic current (open pore current, I_0) and ΔI are expressed as Equation 1−1 and Equation 1−2:

$$I_0 = V\sigma\left(\frac{4L}{\pi d^2} + \frac{1}{d}\right)^{-1} \qquad (1-1)$$

and

$$\Delta I = I_0 - V\sigma\left(\frac{4L}{\pi d_{\mathrm{eff}}^2} + \frac{1}{d_{\mathrm{eff}}}\right)^{-1} \quad (1-2)$$

where V is the applied voltage, σ is the ionic conductivity of the electrolyte, L and d are the length and the diameter of the nanopore, and d_{eff} is the effective diameter of the nanopore during translocation, $d_{\mathrm{eff}} = \sqrt{d^2 - d_{\mathrm{mol}}^2}$ with molecular cross-section diameter d_{mol}.[15] The 1/d terms in the equations represent the access resistance of the nanopore entrance and the exit.[15, 16] The relationship between d_{mol} and ΔI is clear from Equation 1-2: ΔI increases with d_{mol}. Based on this principle, the ultimate goal of the nanopore detection has been set as high-throughput DNA next-generation sequencing (NGS) ever since the emergence of the research field. Conceptually, the DNA bases, adenine (A), thymine (T), guanine (G), and cytosine (C), could produce signals of different characteristic ΔI from the small differences in their molecular structures. Therefore, the information of the DNA sequence could be deciphered by reading the ionic current signal of a translocating DNA molecule.[4, 17]

Influencing factors for t_{d} include the chain length,[18] conformation,[19] and the effective electrical charge[20] of the translocating polymer. Experimental factors such as the interaction between the biomolecule and the nanopore surface,[21, 22] electrolyte viscosity,[23] and nanopore diameter[24] also affect t_{d}. Specific effects of each contribution are very complex; for instance, only an empirical power law could be identified for the chain length effect on t_{d}.[25]

For the detection of the biomolecule translocation signals using nanopores, a measurement system such as the flow cell assembly in Figure 1-4 is utilized.[5] Electrolyte, usually buffered 1 M potassium chloride (KCl) solution for the DNA detection, is filled in the flow cells to create an ionic channel through the solid-state nanopore. On each side of the solid-state nanopore device, a

polydimethylsiloxane (PDMS) block with a ~3 mm diameter hole in its center is inserted between the cell. The roles of the elastomer blocks are to define *cis* and *trans* chambers and prevent leakage of the electrolyte. A pair of silver/silver chloride (Ag/AgCl) electrodes is immersed in each chamber to connect the cell to a current amplifier.

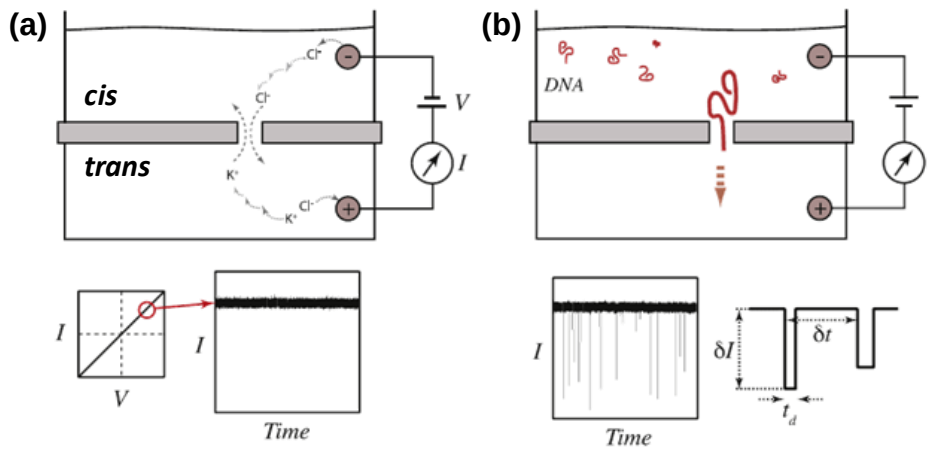

Figure 1−2 Principle of biomolecule detection using nanopores. (a) in the open pore stage, an ionic current is measured across the nanopore by the ionic transport according to the bias voltage. The $I-V$ curve is generally in a linear form. (b) as charged biomolecules are inserted, the molecule passes the nanopore one by one, temporarily blocking the nanopore and generating a peak signal. δI (ΔI in the text), t_{d}, and δt represent the size, duration, and interval of the translocation peak, respectively. Figure was adapted with permission from ref. [3], Copyright 2012 Elsevier B.V. All rights reserved.

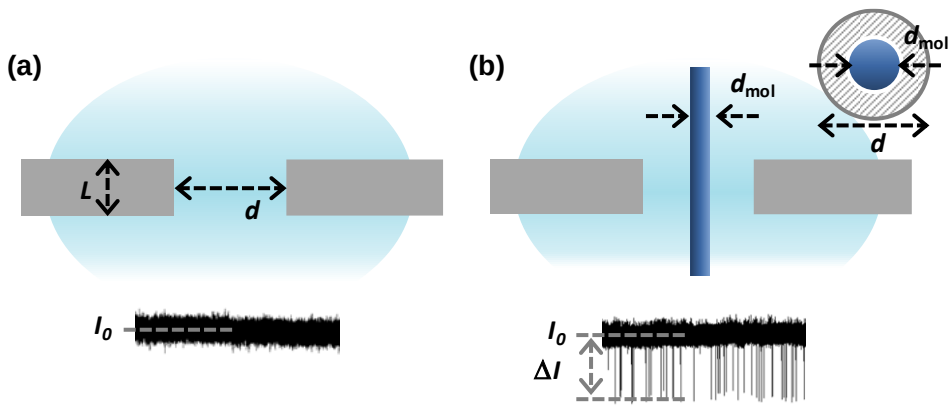

Figure 1-3 Cylindrical resistor model of the solid-state nanopore. (a) a cross-section view of the open pore state, where gray bars represent the nanopore membrane. (b) a conceptual snapshot of a biomolecule translocation. The image at the top right is the top view of a molecule passing through the nanopore. The ionic current trace in (b) was from ref.[26] - Adapted by permission of the Royal Society of Chemistry.

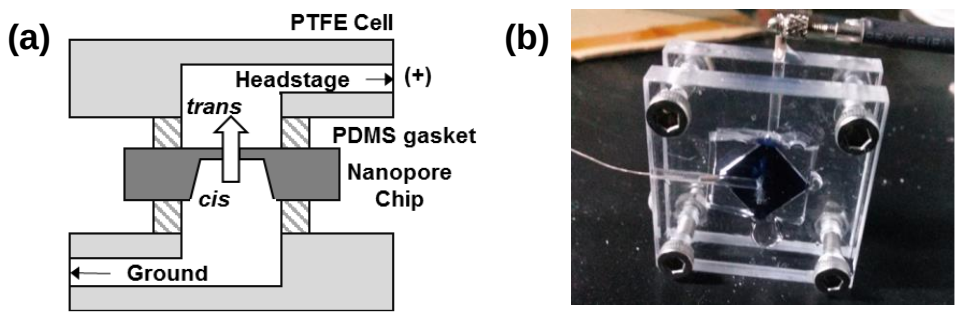

Figure 1-4 Solid-state nanopore experiment setup. (a) a schematic of a flow cell and solid-state nanopore device assembly. Each part is labeled in the figure with the arrow indicating the direction of DNA translocation. (b) an actual assembly of the setup connected to the current amplifier via Ag/AgCl electrodes. (a) was adapted with permission from ref.[5]. Copyright 2018 WILEY-VCH Verlag GmbH & Co. KGaA, Weinheim.

1.3 Conventional Fabrication Technique of the Solid-State Nanopore Device

The fabrication procedure of the solid-state nanopore device was originated from the semiconductor fabrication technique, including film deposition, photolithography, and film etching. The process of fabricating a conventional Si/SiN_x nanopore device is presented in Figure 1-5(a).[1] Low-stress SiN_x thin film is deposited using a low-pressure chemical vapor deposition (LPCVD) method on a double-side polished Si wafer. On one side of the wafer, the freestanding nanopore membrane area is photolithographed, followed by SiN_x dry etching and Si anisotropic wet etching to expose the membrane.

The most important step in the nanopore device fabrication is the pore formation. Since its introduction in 2003, TEM nanoporing has been set as the standard process to create nanopores (Figure 1-5(b)).[12] This method is advantageous for controlling the shape and size of nanopores, capable of sculpting nanopores as small as 2 nm. However, the poring process can only be done one sample by one sample. In addition, the microscope is a heavy and expensive utility, and the accessibility to a TEM machine could depend on laboratories and institutions.

As an alternative, a controlled dielectric breakdown (CDB) method has been reported in 2014.[27] In this protocol, a high electric field of ~100 MV/m was applied to induce mechanical breakdown across the closed membrane.[27, 28] The current measured across the membrane is continuously monitored, and if it reaches a preset threshold determined using Equation 1-1, the electrical power source is shut down (Figure 1-5(c)).[27] CDB technique can overcome the accessibility issue of the TEM-based method, but the protocol is incapable of locating and shaping a nanopore.

Glass nanopipette is another noteworthy form of the fabricated solid-state nanopore (Figure 1-5(d), Figure 1-5(e)). To create the nanopipettes, a ~μm-thick glass nanowire is pulled upon heating by a glass puller machine.[29-31] 2 pipettes are fabricated at

once, having a needle-like structure as it approaches the heated end. The glass pulling is the most efficient method of solid-state nanopore fabrication in terms of time and cost required. Nevertheless, the glass nanopipettes are relatively large nanopores of ~10-nm diameter, in which the size and the effective length of the nanopores are difficult to be controlled during the pulling process.

Apart from the fabrication strategies, various materials have been applied in creating the solid-state nanopore devices. Oxides including silicon dioxide (SiO_2),[24] aluminum oxide (Al_2O_3),[32] and hafnium oxide (HfO_2)[22] have been used as the substrate, additional supporting layer, or the nanopore membrane, respectively. Other classes of materials, namely metals,[33] 2-dimensional (2D) materials,[34-38] and polymers,[39, 40] are utilized in nanopore devices for enhanced sensitivity and functionality, which will be discussed in the next 3 chapters.

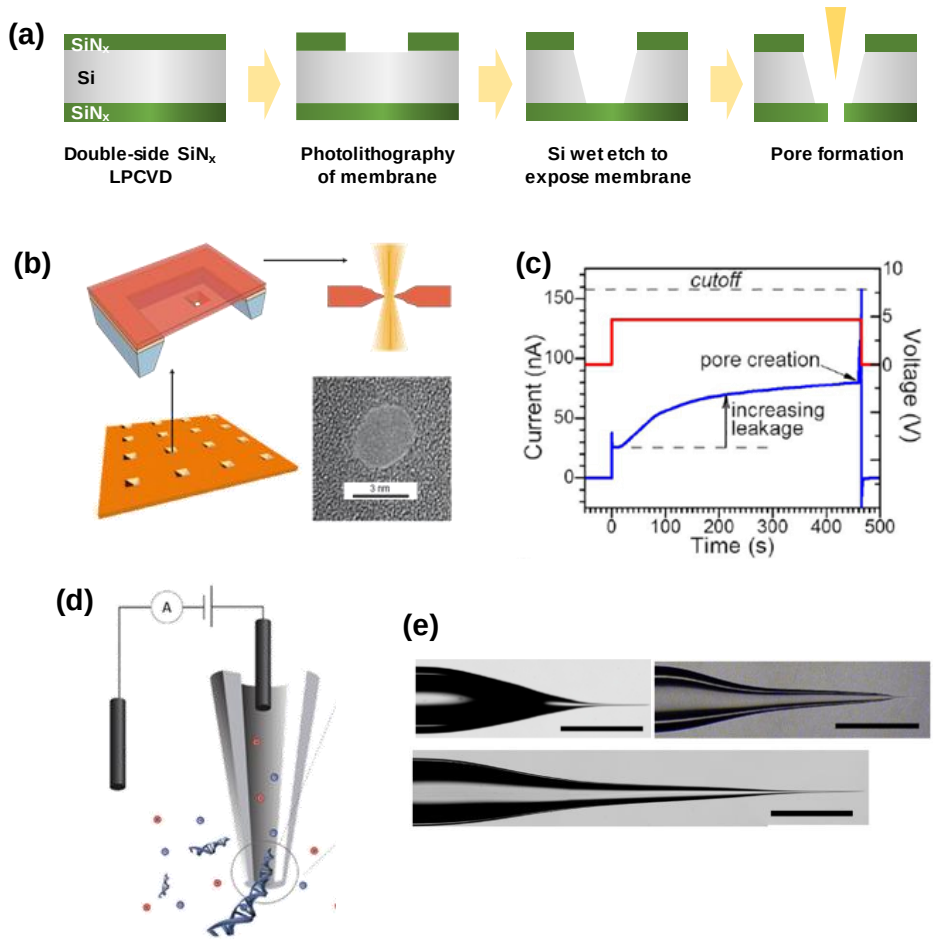

Figure 1-5 Solid-state nanopore fabrication methods. (a) the conventional fabrication process of SiN_x/Si nanopore chip. (b) schematics of solid-state nanopore fabrication using TEM. (c) time-current and time-voltage recordings during a CDB nanopore formation. (d) schematics of DNA detection using glass nanopipette. (e) image of the fabricated glass nanopipettes. The scale bar indicates 1 mm. Figures were adapted with permission from (b) ref.[1]. Copyright 2007, Springer Nature; (c) ref.[27] under the terms of the Creative Commons Attribution License (CC-BY). Copyright 2014 Kwok *et al.*; (d) ref.[41]. Copyright 2015 Royal Society of Chemistry; (e) ref.[42] under the terms of the Creative Commons Attribution License (CC-BY). Copyright 2016 Bafna, Soni.

1.4 Basic Characterizations of the Solid-State Nanopore Device

A solid-state nanopore device fabricated using the previously described process is usually characterized electrically before moving onto biomolecule translocation experiments. To perform the basic electrical characterizations, the flow cell assembly in section 1.2 is connected to a pair of Ag/AgCl electrodes, and the external voltage is applied through the electrodes, without injecting biomolecules in the flow cell

The characteristics to analyze are ionic conductance and electrical noise of the nanopore, as graphically presented in Figure 1-6. In measuring nanopore ionic conductance, the applied voltage is swept and the slope of the $I-V$ graph represents the conductance value. As assumed in section 1.2, a stable nanopore normally follows Ohm's law, exhibiting a linear $I-V$ curve. Therefore, if the nanopore dimension is ambiguous, it can be electrically determined using the measured ionic conductance value and Equation 1-1.

The electrical noise is obtained from an $I-t$ recording at a fixed voltage. Fast Fourier Transformation (FFT) is performed on the recording, and a frequency (f)-noise power spectrum density (PSD) graph can be constructed for the device and the applied voltage.

An example PSD graph is shown in Figure 1-7. The graph can be decomposed into 4 components, flicker, thermal, dielectric, and amplifier noises, respectively. The total noise S_{total} and its 4 noise components, S_{flicker}, S_{thermal}, $S_{\text{dielectric}}$, and $S_{\text{amplifier}}$ are mathematically expressed as in Equation 1-3 to Equation 1-7:

$$S_{\text{total}} = S_{\text{flicker}} + S_{\text{thermal}} + S_{\text{dielectric}} + S_{\text{amplifier}} \quad (1-3)$$

$$S_{\text{flicker}} = A\left(\frac{I^2}{f^{\beta}}\right) = \left(\frac{\alpha}{N_c}\right)\left(\frac{I^2}{f^{\beta}}\right) \quad (1-4)$$

$$S_{\text{thermal}} = \frac{4kT}{R_{\text{P}}} \quad (1-5)$$

$$S_{\text{dielectric}} = 4kTC_{\text{D}}D_{\text{D}}(2\pi f) \quad (1-6)$$

and

$$S_{\text{amplifier}} \approx (2\pi f(C_{\text{D}} + C_{\text{W}} + C_{\text{A}})v_{\text{n}})^2 \quad (1-7)$$

where A is flicker noise power, β is a fitting parameter of ~1, α is the Hooge parameter of the membrane material, N_{c} is the number of charge carriers inside the nanopore, k is the Boltzmann constant, T is the absolute temperature, R_{p} is the nanopore resistance, C_{D} and D_{D} are the capacitance and the dielectric loss of the nanopore device, C_{W} and C_{A} are the electrode wiring and the amplifier capacitances, and v_{n} is the input-referred voltage noise density of the amplifier (V $\text{Hz}^{-1/2}$ unit).[5, 43]

S_{flicker} is a dominant component in the frequency range of <100 Hz. This term is related to the nanopore dimensions (determining I) and the material characteristic of the membrane. For flicker noise, several sources related to the membrane surface state were suggested: inhomogeneous surface charge,[44] carbon contaminations,[45] or imperfect hydrophilicity in the SiN_x surface.[5, 46] S_{thermal} is the noise offset also dependent on the nanopore dimensions (pore resistance R_{p}) and irrelevant of the frequency. $S_{\text{dielectric}}$ and $S_{\text{amplifier}}$ are strongly dependent on the capacitances of the nanopore device and the current amplifier. Particularly, $S_{\text{dielectric}}$ is the major noise component among the 4 factors, dominating the PSD curve in the wide frequency range of 1-100 kHz. On the other hand, $S_{\text{amplifier}}$ is active above 100 kHz, which is the frequency range usually higher than the bandwidths of the lowpass filters (10-100 kHz) applied in the current signal processing in common nanopore experiments.[5]

Therefore, $S_{\text{dielectric}}$ has been the main target to reduce for a low-noise and a high-throughput biomolecule detection platform. The strategies to reduce the dielectric noise in materials and

fabrication aspects are summarized in Figure 1-8. Accordingly, silicon oxide (SiO_2), with lower C_d and D_d than Si, was inserted between the Si substrate and the SiN_x membrane to lower the total device capacitance (Figure 1-8(a)).[24, 43] The most effective improvements in reducing the dielectric noise were reported with replacing the Si substrate to dielectric materials including PDMS and SiO_2.[47, 48] Notably, the glass substrate exhibited 20-times lower $S_{dielectric}$ compared to the conventional Si substrate, still with a compatibility with the semiconductor fabrication technique in creating such devices (Figure 1-8(b), Figure 1-8(c)). As a result, the glass-based nanopore devices showed 1 order of magnitude lower root-mean-square (rms) noise level than the conventional nanopore.[48] Here, the rms noise level I_{rms} was calculated according to Equation 1-8:[49]

$$I_{rms} = \sqrt{\int S_{total}\, df} \quad . \tag{1-8}$$

With the significant improvement in the noise characteristic, elaborate tasks such as DNA base discrimination,[48, 50] protein-protein interaction analysis,[7, 51] and protein sequencing[52] could be successfully demonstrated using the glass substrate nanopores. In the next section, the other issues still remaining in the solid-state nanopore field will be introduced, which are targets of this thesis to be discussed in the next chapters.

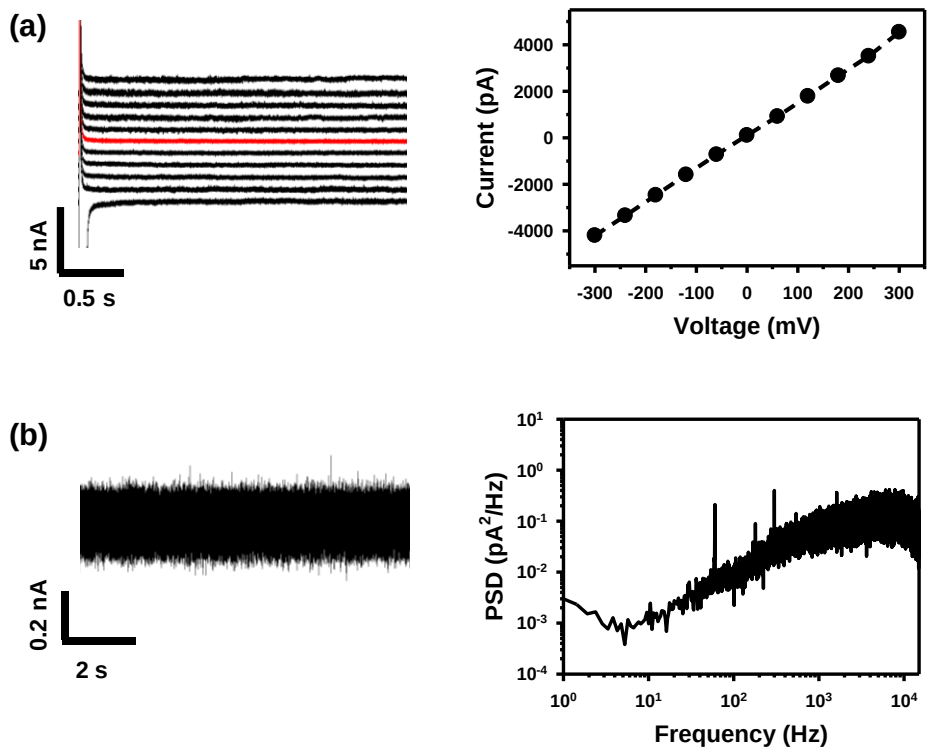

Figure 1-6 Electrical characterization of solid-state nanopore device. (a) voltage sweep current measurement (left) and corresponding $I-V$ plot (right). The red line indicates the current measured at 0 mV. (b) continuous current measurement at 0 mV (left) and corresponding noise PSD curve after FFT (right).

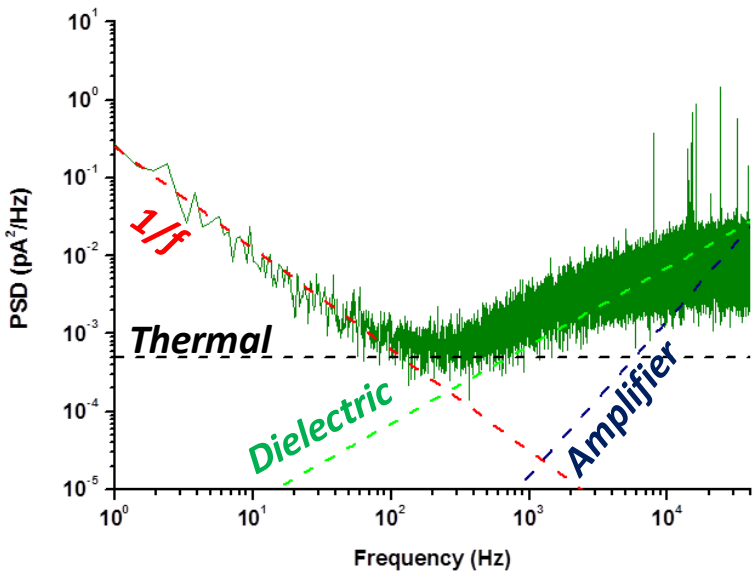

Figure 1-7 Noise in the solid-state nanopore. On the model PSD curve of Si-substrate nanopore, the contributions of each noise component, S_{flicker}, S_{thermal}, $S_{\text{dielectric}}$, and $S_{\text{amplifier}}$, are labeled. Figure was adapted with permission from ref.[5]. Copyright 2018 WILEY-VCH Verlag GmbH & Co. KGaA, Weinheim.

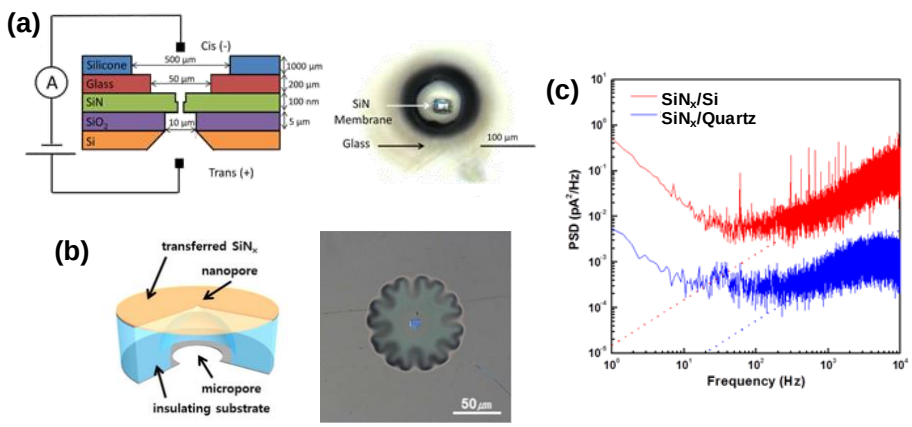

Figure 1-8 Dielectric noise improvements in the solid-state nanopore. (a)-(b) schematics (left) and membrane image (right) of (a) SiO_2 layer inserted nanopore and (b) quartz substrate nanopore. (c) PSD plots of a SiN_x/Si nanopore device (red) and a SiN_x/quartz nanopore device (blue). The dashed lines denote the dielectric noise fitting to each PSD curve. Figures were reproduced with permission from (a) ref.[53]. Copyright 2014 American Chemical Society; (b) ref.[48] under the terms of the Creative Commons Attribution License (CC-BY). Copyright 2014 Springer Nature. (c) was adapted with permission from ref.[48] under the terms of the Creative Commons Attribution License (CC-BY). Copyright 2014 Springer Nature.

1.5 Current Issues in Solid-State Nanopore (Outline of this thesis)

The 3 major issues currently being researched in the solid-state nanopore field are (1) increasing the detection sensitivity, (2) strengthening the device reliability, and (3) extending the application of the platform in other fields of biotechnology (Figure 1-9).

There have been mainly 3 approaches to improve the detection sensitivity of the nanopore: increasing the signal-to-noise ratio (SNR), the spatial sensitivity, and the temporal sensitivity of the translocating molecule.[5] The reduction in the electrical noise of the devices was also favorable for achieving high SNR. The spatial sensitivity of nanopore detection is about how small the device can resolve or distinguish. It is necessary to fabricate the nanopore membrane as thin as possible to detect or resolve a small feature in a molecule.[52, 54, 55] For the high temporal sensitivity of the nanopore, methods to slow down the biomolecule translocations have been studied. Currently, DNA or protein translocation speeds are too fast for stable detection of the translocation signals.[2] The excessively fast passages can be ignored if the data acquisition speed of the amplifier is lower than the translocation speed. Even if not, when the translocation time is comparable to the inverse of the filter bandwidth frequency, the acquired translocation signals can be distorted from the raw data.[43, 56] Therefore, retarding the biomolecule translocation is essential to achieve stable detections and high temporal sensitivity.

Secondly, the device reliability issue is originated from nonspecific adsorptions of biomolecules onto the membrane surfaces frequently occurring during the nanopore experiments. The unwanted adherence often induces temporary or permanent damage to the device, physically blocking a nanopore and further translocations of other free molecules.[57] To prevent the nonspecific adsorptions, surface functionalization using antifouling materials such as poly(ethylene glycol)(PEG) have been reported.[58, 59] Thirdly,

there have been attempts to extend the application of the solid-state nanopore devices from the originally intended electrical DNA sequencing.[33, 60-62]

In this thesis, the 3 issues in the solid-state nanopore research will be explained in detail. The target molecule in this thesis is focused on nucleic acids, which are biomolecules commonly detected and analyzed in solid-state nanopore research. Previous reports on each theme will be summarized, and electrokinetics based analysis will be presented with the experimental results and discussions based on the result.

The approaches taken in this thesis are physical and structural, focusing on the electrokinetics surrounding the nanopore and translocating DNA. In detail, chapter 2 will discuss the sensitivity issue in both aspects of the SNR and slow DNA translocations. The electrokinetic environment in the nanopore region was physically modeled, and structural modification to enhance the DNA sensitivity was designed. Enhancement in the reliability of the nanopore device will be presented in chapter 3. Here, a gas-phase PEG deposition method, plasma polymerization, on the nanopore membrane was utilized instead of self-assembly previously used in the nanopore field. In addition, the anti-adsorption properties of the PEG deposited surface were evaluated relative to the bare SiN_x membrane. Chapter 4 will present a new application of a nanoporous membrane device on nucleic acid preparation. Particularly, the expansion of the solid-state nanopore application field has been focusing on the multiplexing of the nanopore structure to increase operation throughput. Following the same research direction, in this work, the structure and fabrication of nanofilter membrane device were derived from solid-state nanopore device structure and its fabrication method. Similar to the nanopore experiments, an electric potential was applied across the nanofilter membrane to facilitate the transport of charged biomolecules in a sample. The concept and feasibility of the electrophoretic nucleic acid preparation will be discussed, and the performance of the new preparation system will be evaluated by comparing it to that of the conventional protocol.

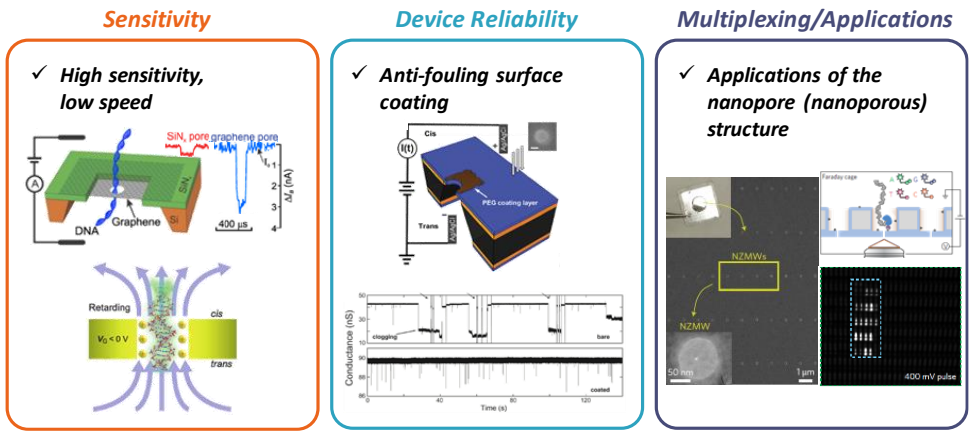

Figure 1-9 Summary of the current issues in the solid-state nanopore. Figures were adapted with permission from ref.[63]. Copyright 2013 Garaj *et al.*; ref.[64]. Copyright 2011 American Chemical Society (sensitivity); ref.[58]. Copyright 2014 WILEY-VCH Verlag GmbH & Co. KGaA, Weinheim (device reliability); ref.[60]. Copyright 2017 Springer Nature (multiplexing/applications).

References

1. Dekker, C., Solid-state nanopores. *Nat. Nanotechnol.* 2007, *2* (4), 209-215.

2. Venkatesan, B. M.; Bashir, R., Nanopore sensors for nucleic acid analysis. *Nat. Nanotechnol.* 2011, *6* (10), 615-624.

3. Wanunu, M., Nanopores: A journey towards DNA sequencing. *Physics of life reviews* 2012, *9* (2), 125-58.

4. Deamer, D.; Akeson, M.; Branton, D., Three decades of nanopore sequencing. *Nature biotechnology* 2016, *34*, 518.

5. Lee, K.; Park, K. B.; Kim, H. J.; Yu, J. S.; Chae, H.; Kim, H. M.; Kim, K. B., Recent Progress in Solid-State Nanopores. *Advanced Materials* 2018, *30* (42), 1704680.

6. Steinbock, L. J.; Krishnan, S.; Bulushev, R. D.; Borgeaud, S.; Blokesch, M.; Feletti, L.; Radenovic, A., Probing the size of proteins with glass nanopores. *Nanoscale* 2014, *6* (23), 14380-7.

7. Kwak, D. K.; Chae, H.; Lee, M. K.; Ha, J. H.; Goyal, G.; Kim, M. J.; Kim, K. B.; Chi, S. W., Probing the Small-Molecule Inhibition of an Anticancer Therapeutic Protein-Protein Interaction Using a Solid-State Nanopore. *Angewandte Chemie International Edition in English* 2016, *55* (19), 5713-7.

8. Kasianowicz, J. J.; Brandin, E.; Branton, D.; Deamer, D. W., Characterization of individual polynucleotide molecules using a membrane channel. *Proceedings of the National Academy of Sciences of the United States of America* 1996, *93* (24), 13770-13773.

9. Branton, D., *et al.*, The potential and challenges of nanopore sequencing. *Nature biotechnology* 2008, *26* (10), 1146-53.

10. Akeson, M.; Branton, D.; Kasianowicz, J. J.; Brandin, E.; Deamer, D. W., Microsecond Time-Scale Discrimination Among Polycytidylic Acid, Polyadenylic Acid, and Polyuridylic Acid as Homopolymers or as Segments Within Single RNA Molecules. *Biophysical journal* 1999, *77* (6), 3227-3233.

11. Li, J.; Stein, D.; McMullan, C.; Branton, D.; Aziz, M. J.; Golovchenko, J. A., Ion-beam sculpting at nanometre length scales.

Nature 2001, *412* (6843), 166-169.

12. Storm, A. J.; Chen, J. H.; Ling, X. S.; Zandbergen, H. W.; Dekker, C., Fabrication of solid-state nanopores with single-nanometre precision. *Nature materials* 2003, *2* (8), 537-540.

13. Rhee, M.; Burns, M. A., Nanopore sequencing technology: nanopore preparations. *Trends in biotechnology* 2007, *25* (4), 174-81.

14. Gilboa, T.; Torfstein, C.; Juhasz, M.; Grunwald, A.; Ebenstein, Y.; Weinhold, E.; Meller, A., Single-Molecule DNA Methylation Quantification Using Electro-optical Sensing in Solid-State Nanopores. *ACS Nano* 2016, *10* (9), 8861-8870.

15. Kowalczyk, S. W.; Grosberg, A. Y.; Rabin, Y.; Dekker, C., Modeling the conductance and DNA blockade of solid-state nanopores. *Nanotechnology* 2011, *22* (31), 315101.

16. Hall, J. E., Access resistance of a small circular pore. *The Journal of General Physiology* 1975, *66* (4), 531-532.

17. Clarke, J.; Wu, H. C.; Jayasinghe, L.; Patel, A.; Reid, S.; Bayley, H., Continuous base identification for single-molecule nanopore DNA sequencing. *Nat. Nanotechnol.* 2009, *4* (4), 265-70.

18. Jiali, L.; David, S. T., The distribution of DNA translocation times in solid-state nanopores. *Journal of Physics: Condensed Matter* 2010, *22* (45), 454129.

19. Fologea, D.; Brandin, E.; Uplinger, J.; Branton, D.; Li, J., DNA conformation and base number simultaneously determined in a nanopore. *Electrophoresis* 2007, *28* (18), 3186-3192.

20. Kowalczyk, S. W.; Wells, D. B.; Aksimentiev, A.; Dekker, C., Slowing down DNA Translocation through a Nanopore in Lithium Chloride. *Nano Letters* 2012, *12* (2), 1038-1044.

21. Banerjee, S.; Wilson, J.; Shim, J.; Shankla, M.; Corbin, E. A.; Aksimentiev, A.; Bashir, R., Slowing DNA Transport Using Graphene-DNA Interactions. *Advanced Functional Materials* 2015, *25* (6), 936-946.

22. Larkin, J.; Henley, R.; Bell, D. C.; Cohen-Karni, T.; Rosenstein, J. K.; Wanunu, M., Slow DNA transport through

nanopores in hafnium oxide membranes. *ACS Nano* 2013, *7* (11), 10121−8.

23. Fologea, D.; Uplinger, J.; Thomas, B.; McNabb, D. S.; Li, J., Slowing DNA translocation in a solid−state nanopore. *Nano Letters* 2005, *5* (9), 1734−1737.

24. Carson, S.; Wilson, J.; Aksimentiev, A.; Wanunu, M., Smooth DNA Transport through a Narrowed Pore Geometry. *Biophysical journal* 2014, *107* (10), 2381−2393.

25. Wanunu, M.; Sutin, J.; McNally, B.; Chow, A.; Meller, A., DNA Translocation Governed by Interactions with Solid−State Nanopores. *Biophysical journal* 2008, *95* (10), 4716−4725.

26. Lee, K.; Lee, H.; Lee, S.−H.; Kim, H.−M.; Kim, K.−B.; Kim, S. J., Enhancing the sensitivity of DNA detection by structurally modified solid−state nanopore. *Nanoscale* 2017, *9* (45), 18012−18021.

27. Kwok, H.; Briggs, K.; Tabard−Cossa, V., Nanopore Fabrication by Controlled Dielectric Breakdown. *PLOS ONE* 2014, *9* (3), e92880.

28. Matsui, K.; Yanagi, I.; Goto, Y.; Takeda, K.−i., Prevention of Dielectric Breakdown of Nanopore Membranes by Charge Neutralization. *Scientific reports* 2015, *5* (1), 17819.

29. Steinbock, L. J.; Bulushev, R. D.; Krishnan, S.; Raillon, C.; Radenovic, A., DNA Translocation through Low−Noise Glass Nanopores. *ACS Nano* 2013, *7* (12), 11255−62.

30. Li, W.; Bell, N. A.; Hern□ndez−Ainsa, S.; Thacker, V. V.; Thackray, A. M.; Bujdoso, R.; Keyser, U. F., Single protein molecule detection by glass nanopores. *ACS Nano* 2013, *7* (5), 4129−4134.

31. Gong, X.; Patil, A. V.; Ivanov, A. P.; Kong, Q.; Gibb, T.; Dogan, F.; deMello, A. J.; Edel, J. B., Label−Free In−Flow Detection of Single DNA Molecules using Glass Nanopipettes. *Analytical Chemistry* 2014, *86* (1), 835−841.

32. Chen, P.; Mitsui, T.; Farmer, D. B.; Golovchenko, J.; Gordon, R. G.; Branton, D., Atomic layer deposition to fine−tune the surface properties and diameters of fabricated nanopores. *Nano Letters* 2004, *4* (7), 1333−1337.

33. Pitchford, W. H.; Kim, H.-J.; Ivanov, A. P.; Kim, H.-M.; Yu, J.-S.; Leatherbarrow, R. J.; Albrecht, T.; Kim, K.-B.; Edel, J. B., Synchronized Optical and Electronic Detection of Biomolecules Using a Low Noise Nanopore Platform. *ACS Nano* 2015, *9* (2), 1740-1748.

34. Garaj, S.; Hubbard, W.; Reina, A.; Kong, J.; Branton, D.; Golovchenko, J. A., Graphene as a subnanometre trans-electrode membrane. *Nature* 2010, *467* (7312), 190-193.

35. Schneider, G. F.; Kowalczyk, S. W.; Calado, V. E.; Pandraud, G.; Zandbergen, H. W.; Vandersypen, L. M. K.; Dekker, C., DNA Translocation through Graphene Nanopores. *Nano Letters* 2010, *10* (8), 3163-3167.

36. Zhou, Z.; Hu, Y.; Wang, H.; Xu, Z.; Wang, W.; Bai, X.; Shan, X.; Lu, X., DNA Translocation through Hydrophilic Nanopore in Hexagonal Boron Nitride. *Scientific reports* 2013, *3* (1), 3287.

37. Liu, K.; Feng, J.; Kis, A.; Radenovic, A., Atomically Thin Molybdenum Disulfide Nanopores with High Sensitivity for DNA Translocation. *ACS Nano* 2014, *8* (3), 2504-2511.

38. Feng, J.; Liu, K.; Bulushev, R. D.; Khlybov, S.; Dumcenco, D.; Kis, A.; Radenovic, A., Identification of single nucleotides in MoS2 nanopores. *Nat. Nanotechnol.* 2015, *10* (12), 1070-6.

39. Wanunu, M.; Meller, A., Chemically modified solid-state nanopores. *Nano Letters* 2007, *7* (6), 1580-1585.

40. Kim, H.-J.*, et al.*, Translocation of DNA and protein through a sequentially polymerized polyurea nanopore. *Nanoscale* 2019, *11* (2), 444-453.

41. Sze, J. Y. Y.; Kumar, S.; Ivanov, A. P.; Oh, S.-H.; Edel, J. B., Fine tuning of nanopipettes using atomic layer deposition for single molecule sensing. *Analyst* 2015, *140* (14), 4828-4834.

42. Bafna, J. A.; Soni, G. V., Fabrication of Low Noise Borosilicate Glass Nanopores for Single Molecule Sensing. *PLOS ONE* 2016, *11* (6), e0157399.

43. Rosenstein, J. K.; Wanunu, M.; Merchant, C. A.; Drndic, M.; Shepard, K. L., Integrated nanopore sensing platform with sub-

microsecond temporal resolution. *Nature methods* 2012, *9* (5), 487–U112.

44. Hoogerheide, D. P.; Albertorio, F.; Golovchenko, J. A., Escape of DNA from a Weakly Biased Thin Nanopore: Experimental Evidence for a Universal Diffusive Behavior. *Phys. Rev. Lett.* 2013, *111* (24), 248301.

45. Radenovic, A.; Trepagnier, E.; Csencsits, R.; Downing, K. H.; Liphardt, J., Fabrication of 10 nm diameter hydrocarbon nanopores. *Applied Physics Letters* 2008, *93* (18), 183101.

46. Beamish, E.; Kwok, H.; Tabard-Cossa, V.; Godin, M., Precise control of the size and noise of solid-state nanopores using high electric fields. *Nanotechnology* 2012, *23* (40), 405301.

47. Jain, T.; Guerrero, R. J. S.; Aguilar, C. A.; Karnik, R., Integration of solid-state nanopores in microfluidic networks via transfer printing of suspended membranes. *Analytical chemistry* 2013, *85* (8), 3871-3878.

48. Lee, M. H.; Kumar, A.; Park, K. B.; Cho, S. Y.; Kim, H. M.; Lim, M. C.; Kim, Y. R.; Kim, K. B., A low-noise solid-state nanopore platform based on a highly insulating substrate. *Scientific reports* 2014, *4* (1), 7448.

49. Park, K.-B.; Kim, H.-J.; Kim, H.-M.; Han, S. A.; Lee, K. H.; Kim, S.-W.; Kim, K.-B., Noise and sensitivity characteristics of solid-state nanopores with a boron nitride 2-D membrane on a pyrex substrate. *Nanoscale* 2016, *8* (10), 5755-5763.

50. Venta, K.; Shemer, G.; Puster, M.; Rodriguez-Manzo, J. A.; Balan, A.; Rosenstein, J. K.; Shepard, K.; Drndic, M., Differentiation of Short Single-Stranded DNA Homopolymers in Solid-State Nanopores. *ACS Nano* 2013, *7* (5), 4629-4636.

51. Chae, H.; Kwak, D.-K.; Lee, M.-K.; Chi, S.-W.; Kim, K.-B., Solid-state nanopore analysis on conformation change of p53TAD–MDM2 fusion protein induced by protein–protein interaction. *Nanoscale* 2018, *10* (36), 17227-17235.

52. Yu, J.-S.; Hong, S. C.; Wu, S.; Kim, H.-M.; Lee, C.; Lee, J.-S.; Lee, J. E.; Kim, K.-B., Differentiation of selectively labeled peptides using solid-state nanopores. *Nanoscale* 2019, *11* (5), 2510-2520.

53. Balan, A.; Machielse, B.; Niedzwiecki, D.; Lin, J.; Ong, P.; Engelke, R.; Shepard, K.; Drndic, M., Improving signal−to−noise performance for DNA translocation in solid−state nanopores at MHz bandwidths. *Nano Letters* 2014, *14* (12), 7215−7220.

54. Rodríguez−Manzo, J. A.; Puster, M.; Nicolaï, A.; Meunier, V.; Drndić, M., DNA Translocation in Nanometer Thick Silicon Nanopores. *ACS Nano* 2015, *9* (6), 6555−6564.

55. Rena, A.; Takanobu, H.; Toshiyuki, H.; Itaru, Y.; Takeshi, O.; Hirotaka, H.; Tomio, I.; Takahide, Y.; Takashi, A., Slowing single−stranded DNA translocation through a solid−state nanopore by decreasing the nanopore diameter. *Nanotechnology* 2014, *25* (27), 275501.

56. Larkin, J.; Henley, R. Y.; Muthukumar, M.; Rosenstein, J. K.; Wanunu, M., High−Bandwidth Protein Analysis Using Solid−State Nanopores. *Biophysical journal* 2014, *106* (3), 696−704.

57. Niedzwiecki, D. J.; Grazul, J.; Movileanu, L., Single−Molecule Observation of Protein Adsorption onto an Inorganic Surface. *Journal of the American Chemical Society* 2010, *132* (31), 10816−10822.

58. Tang, Z.; Lu, B.; Zhao, Q.; Wang, J.; Luo, K.; Yu, D., Surface modification of solid−state nanopores for sticky−free translocation of single−stranded DNA. *Small* 2014, *10* (21), 4332−4339.

59. Schneider, G. g. F.; Xu, Q.; Hage, S.; Luik, S.; Spoor, J. N. H.; Malladi, S.; Zandbergen, H.; Dekker, C., Tailoring the hydrophobicity of graphene for its use as nanopores for DNA translocation. *Nature Communications* 2013, *4*, 2619.

60. Larkin, J.; Henley, R. Y.; Jadhav, V.; Korlach, J.; Wanunu, M., Length−independent DNA packing into nanopore zero−mode waveguides for low−input DNA sequencing. *Nat. Nanotechnol.* 2017, *12* (12), 1169.

61. Jadhav, V.; Hoogerheide, D. P.; Korlach, J.; Wanunu, M., Porous Zero−Mode Waveguides for Picogram−Level DNA Capture. *Nano Letters* 2019, *19* (2), 921−929.

62. Wang, R.; Gilboa, T.; Song, J.; Huttner, D.; Grinstaff, M. W.; Meller, A., Single−Molecule Discrimination of Labeled DNAs and

Polypeptides Using Photoluminescent-Free TiO2 Nanopores. *ACS Nano* 2018, *12* (11), 11648-11656.

63. Garaj, S.; Liu, S.; Golovchenko, J. A.; Branton, D., Molecule-hugging graphene nanopores. *Proceedings of the National Academy of Sciences of the United States of America* 2013, *110* (30), 12192-12196.

64. He, Y.; Tsutsui, M.; Fan, C.; Taniguchi, M.; Kawai, T., Controlling DNA translocation through gate modulation of nanopore wall surface charges. *ACS Nano* 2011, *5* (7), 5509-5518.

Chapter 2

Enhancement of DNA Detection Sensitivity in Solid-State Nanopore by Structural Modification

- Based on the publication K. Lee,† H. Lee†, *et al.*, Enhancing the sensitivity of DNA detection by structurally modified solid-state nanopore, *Nanoscale* 2017, 9 (45), 18012-18021.[1]

2.1 Introduction

As discussed in the previous chapter, enhancing the SNR, spatial sensitivity, and temporal sensitivity are 3 major approaches to resolve the sensitivity issue of the solid-state nanopore. Among the 3 subjects, the spatial sensitivity is mainly determined by the thickness of the nanopore membrane. Ideally, a nanopore as thin as the spatial interval between nucleobases in DNA, 0.34 nm, is needed for the discrimination of the bases and for DNA sequencing.[2] Similarly, a thin nanopore is also advantageous for detecting small molecules such as single nucleobases[3] and short peptides.[4] The membrane, however, has an inherent limitation: high level of the electrical noise induced by mechanical fluctuation and structural defects of the thin membrane.[5, 6]

Discussions on the other 2 topics, the SNR and the temporal sensitivity, are more complex than the simple and geometry-dependent spatial sensitivity issue. The SNR and the DNA translocation time are affected by the experimental conditions, external forces, and the electrokinetic environment surrounding the translocating DNA, as well as the nanopore dimensions.[7-10] Therefore, the goal of this chapter is to present a physical and systematic analysis of the DNA sensitivity of the solid-state nanopore and to suggest a structural approach to enhance the sensitivity based on the analysis. This chapter will begin with a summary of the previous works on improving device performance, which began with simple and evident approaches to deal with the issues.

2.1.1 Previous Studies on the Signal Magnitude Enhancement of the Solid-State Nanopore

The means to increase the SNR in the solid-state nanopore is 1) to increase the signal magnitude and 2) to decrease the electrical noise of the device. The electrical noise was discussed in detail in chapter 1, so only the methods to increase the signal magnitude will be presented in this section.

The simplest physical interpretation of the signal magnitude was based on the resistor model in section 1.2. In Equation 1-2, ΔI was explained using the nanopore dimensions, the applied voltage, the ionic conductivity of the electrolyte, and the size of the translocating molecule. With the fixed target molecule (dsDNA), the electrolyte concentration and the voltage dependences of ΔI were experimentally confirmed.[7, 11]

Figure 2-1 explains the nanopore dimension dependence of ΔI calculated using Equation 1-2. In the calculation, nanopore length L or nanopore diameter d were fixed to 20 nm and 5 nm respectively, which were selected from the conventional structure of a solid-state nanopore. Likewise, the applied voltage and the electrolyte were set to 200 mV and 1 M KCl to reflect the typical experimental conditions for DNA detection using the solid-state nanopore. When d was changed from 20 nm to 2.2 nm (d_{mol} for dsDNA), ΔI increased by a factor of 2.41 (Figure 2-1(a)). The effect of L was more dramatic; in Figure 2-1(b), ΔI from a 1-nm long nanopore was 7.47 times larger than that from a nanopore in a 20-nm thick membrane.

From this analysis, the previous works to achieve large SNR in nanopore detection focused on fabricating thin membranes for nanopores. The reports are summarized in Figure 2-2. Meanwhile, thinning the membrane was the same methodology taken to enhance the spatial sensitivity of nanopores. To fabricate a thin membrane, the SiN_x membrane was locally thinned down to ~1 nm using a scanning tunneling electron microscope (STEM) (Figure 2-2(a)).[12] More recently, nanopore devices with 3-nm thin SiN_x membrane were created by applying poly-Si/SiO_2 sacrificial layers to protect

the film during the etch process (Figure 2-2(b)).[13, 14]

In another sense, 2-dimensional (2D) materials were utilized as the membrane to fabricate thin nanopores (Figure 2-3). Namely, graphene (Figure 2-3(a)),[10, 15, 16] hexagonal boron nitride (*h*-BN) (Figure 2-3(b)),[5, 17, 18] and molybdenum disulfide (MoS_2) (Figure 2-3(c))[3, 19, 20] are representative 2D materials used in the solid-state nanopore fabrication. The listed materials have a sub-nanometer thickness, approaching to the distance between DNA nucleotides. As a result, the 2D membranes could produce DNA translocation signals with ~2 times the magnitude of those from the 20-nm thick SiN_x nanopores,[2, 10] and discriminate single nucleotides.[3] Furthermore, the effect of the nanopore diameter to ΔI was examined in the graphene nanopore to obtain even larger DNA translocation signals (Figure 2-3(a)).

In summary, the theoretic influence of experimental and geometrical parameters to ΔI was confirmed experimentally; high voltage, high electrolyte strength, small nanopore diameter, and short nanopore thickness were favorable for large ΔI. However, particularly, the thin membranes inherently possess the high electrical noise limitation as mentioned above. In addition, the previous works were based on a simple analysis without considering the complex nature of DNA translocation. Therefore, a more realistic approach is required to understand ΔI and to improve the nanopore signal magnitude of DNA translocation.

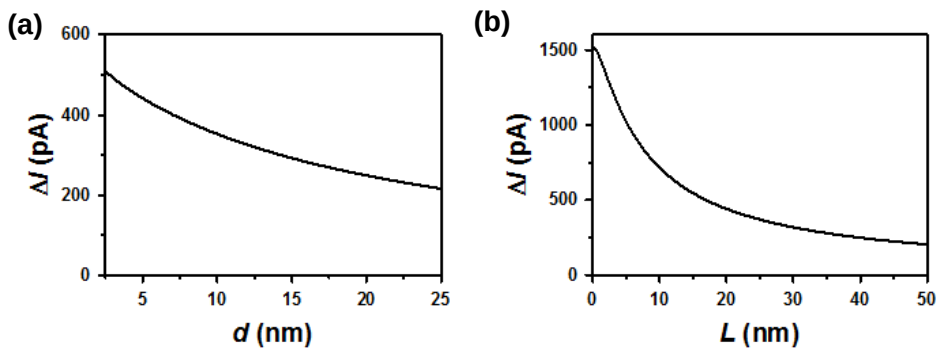

Figure 2-1 Relationship between ΔI and nanopore dimensions. Calculated ΔI using Equation 1-2, assuming σ=15.0 S/m (1 M KCl), V=200 mV, d_{mol}=2.2 nm (for dsDNA), with (a) varying d at L=20 nm and (b) varying L at d=5 nm.

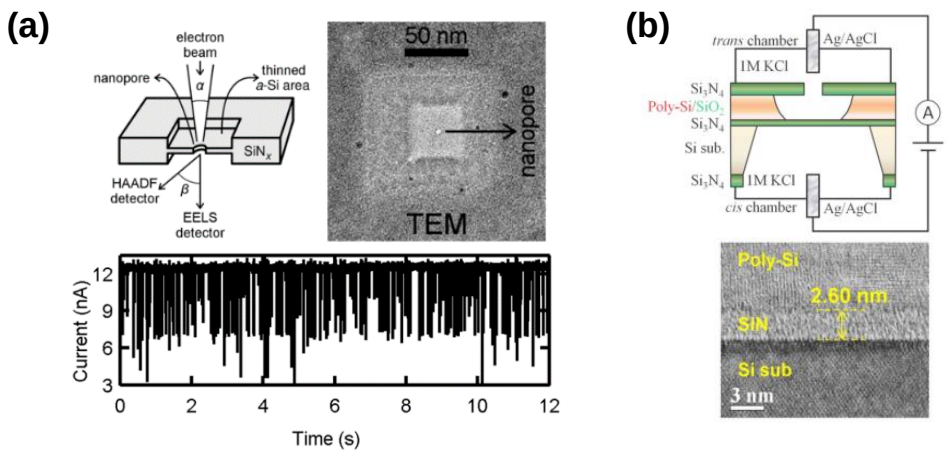

Figure 2-2 Thinning of SiN_x membrane to increase ΔI. (a) locally thinned SiN_x membrane by STEM thinning and the nanopore signals obtained from the ~1 nm-short nanopore. (b) ~3 nm-thick SiN_x membrane for nanopore using poly-Si/SiO_2 sacrificial layer. Figures were adapted with permission from (a) ref.[12]. Copyright 2015 American Chemical Society; (b) ref.[14] under the terms of the Creative Commons Attribution License (CC-BY). Copyright 2015 Springer Nature.

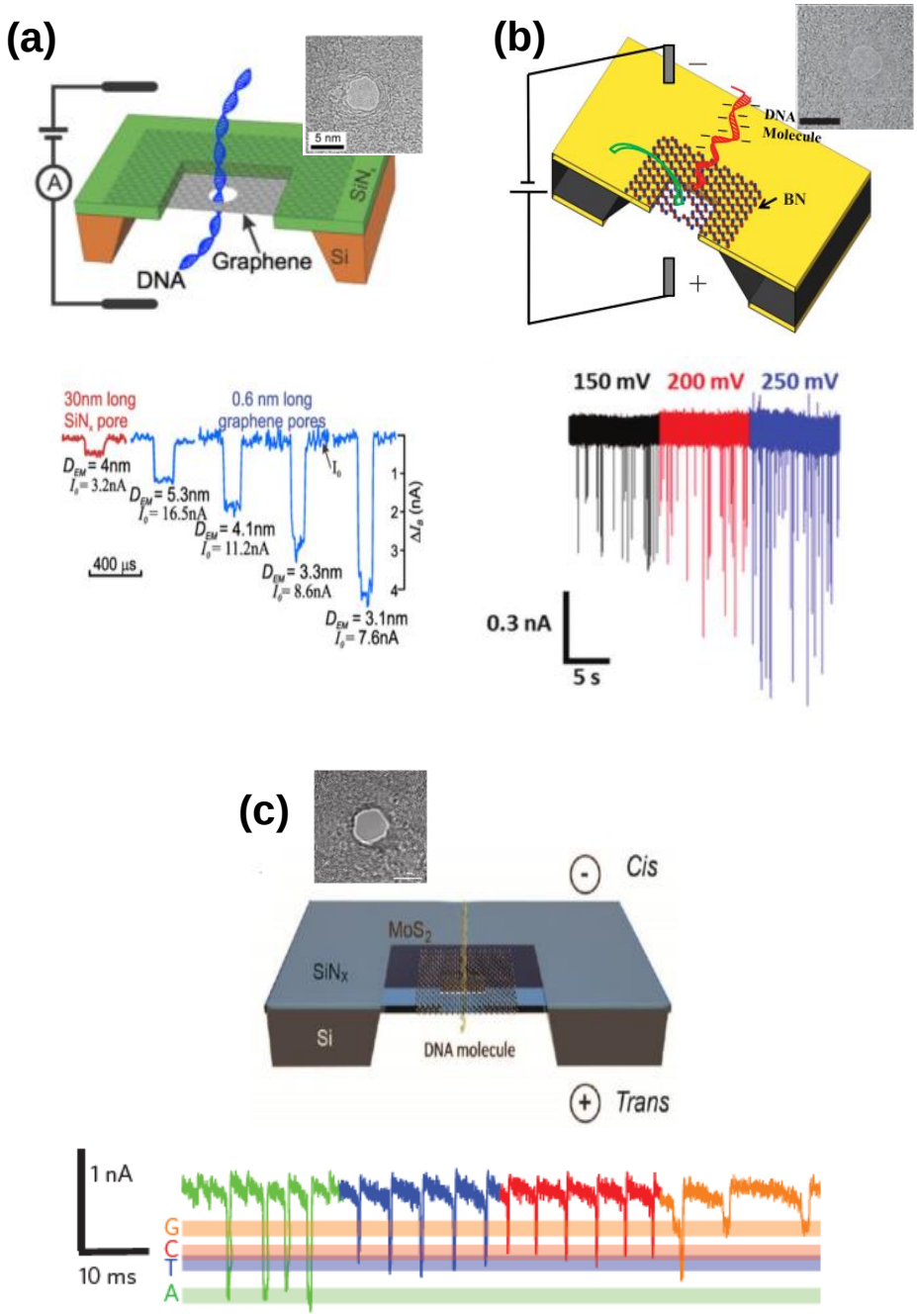
(a)
5 nm
A
SiN
Si
Graphene
DNA
30nm long
SiN, pore
0.6 nm long
graphene pores
D_{EM} = 4nm
I_0 = 3.2nA
D_{EM} = 5.3nm
I_0 = 16.5nA
D_{EM} = 4.1nm
I_0 = 11.2nA
D_{EM} = 3.3nm
I_0 = 8.6nA
D_{EM} = 3.1nm
I_0 = 7.6nA
I_0
ΔI_0 (nA)
400 µs
(b)
DNA
Molecule
BN
150 mV
200 mV
250 mV
0.3 nA
5 s
(c)
Cis
MoS_2
SiN_x
Si
DNA molecule
Trans
1 nA
10 ms
G
C
T
A

Figure 2-3 2D membrane solid-state nanopore. (a) graphene nanopore schematics and TEM image of a nanopore formed on graphene (top), DNA translocation signals and their magnitudes with the respective nanopore dimensions (bottom). (b) diagram of *h*-BN nanopore with a TEM image (top), concatenated DNA translocation signals obtained from *h*-BN nanopore (bottom). (c) MoS_2 nanopore schematics with a TEM image (top), translocation signals of poly adenine (A_{30}), thymine (T_{30}), cytosine (C_{30}) and guanine (G_{30}) detected by the MoS_2 nanopore (bottom). Figures were reproduced with permission from (a) ref.[10]. Copyright 2013 Garaj *et al.*; inset of (a) ref.[16]. Copyright 2010 American Chemical Society; (b) ref.[18]. Copyright 2013 WILEY-VCH Verlag GmbH & Co. KGaA, Weinheim and ref.[5]. Copyright 2016 Royal Society of Chemistry; (c) ref.[19]. Copyright 2014 American Chemical Society and ref.[3]. Copyright 2015 Springer Nature; inset of (c) ref.[3]. Copyright 2015 Springer Nature.

2.1.2. Previous Studies on Slowing Down DNA Translocations in the Solid-State Nanopore

Figure 2-4 summarizes the 3 main approaches to reduce the DNA translocation speed through the solid-state nanopore. Firstly, studies on DNA translocation speed have heavily relied on empirical relations of the experimental parameters and the translocation speed (Figure 2-4(a)) because the movement of the flexible and long polymer is a very complicated phenomenon to model. Therefore, earlier works on slowing down the DNA translocation speed first controlled the applied voltage and the electrolyte viscosity.[7, 9] Obviously, low applied voltage and high electrolyte viscosity induced slow DNA translocations through the nanopore. In addition, DNA translocations in lithium chloride (LiCl) electrolyte were slower than those in KCl. This effect was originated from more effective shielding of the DNA electrical charge by Li^+ ions than by K^+ ions, resulting in a lower effective charge of DNA in LiCl than in KCl.[21] To summarize, the experimental approaches were effective in slowing down DNA translocations and easy to apply. Nevertheless, the window of the parameter control was very narrow; for instance, the lowest voltage to promote DNA translocation was ~100 mV,[7] only about 2-fold lower than the general experimental conditions. Moreover, a reduction in SNR was an inevitable tradeoff in decreasing the applied voltage.

Secondly, extra external dragging forces other than the applied voltage was introduced to the translocating DNA (Figure 2-4(b)). Mechanical forces were exerted on the DNA via optical, magnetic, and molecular tweezers[22-24] to individually pull the DNA against the electrical translocation direction. This method directly slowed down the DNA movements, but dragging the DNA molecule one-by-one was inappropriate for practical uses. Another extra force applicable was the positive gate voltage, with the gate electrode embedded in the nanopore to electrically drag the negatively charged biomolecule from quickly passing through.[25] This was an effective and fundamental approach to slow down DNA translocations, but

fabricating the nanopore device with the gate electrode was difficult, showing a low yield.

The last track to achieve slow DNA translocation in the solid-state nanopore was inducing strong molecular interactions between the nanopore surface and DNA (Figure 2-3(c)). For instance, graphene and HfO_2 membranes strongly interacted with DNA molecules and produce long-lasting DNA translocation signals than the conventional SiN_x nanopores.[26, 27] In addition, other interactive materials such as agarose gel were coated on the SiN_x membrane to obstruct smooth DNA movements to and through the nanopore.[28, 29] Nevertheless, the interaction between the nanopore surface and DNA was difficult to control, so was the degree of retardation of DNA translocation through the modified nanopores.

To summarize, the previous works were successful in slowing down the DNA translocations in the solid-state nanopore, but they lacked systematic analysis on the translocation speed. Therefore, a physical analysis of DNA translocation speed is still required for its effective control. In the next section, velocities related to the electrokinetic environment near a translocating DNA molecule will be explained. Based on the physical factors, a new solid-state nanopore structure to effectively control the DNA translocation speed as well as to enhance the translocation signal magnitude will be suggested.

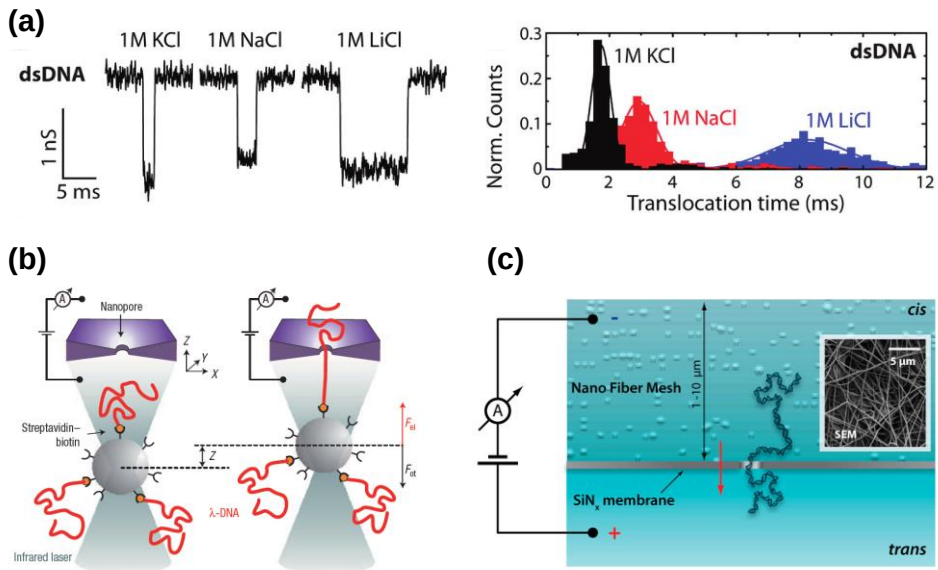

Figure 2-4 Slowing down DNA translocations in the solid-state nanopore. (a) DNA translocation signals (left) and time histograms (right) in different electrolytes: KCl (black), NaCl (red), and LiCl (blue). (b) illustration of optical tweezer pulling of DNA during nanopore translocation. (c) DNA dragging by interaction with nanofiber gel mesh. Figures were reproduced with permission from (a) ref.[21]. Copyright 2012 American Chemical Society; (b) ref.[30]. Copyright 2006 Springer Nature; (c) ref.[28]. Copyright 2013 American Chemical Society.

2.2 Design and Fabrication of the Guide-Inserted Nanopore Device

2.2.1 Physical Interpretation of DNA Translocation through the Nanopore

Under the electric field generated by the applied voltage, a translocating DNA molecule is affected by electrophoresis and electroosmosis as illustrated in Figure 2-5. The major driving force of DNA translocation is electrophoresis, where the electrophoretic velocity of DNA v_{EPH} is physically described with the electrophoretic mobility of DNA μ_{DNA} and the electric field E as Equation 2-1:

$$v_{EPH} = \mu_{DNA} E. \quad (2-1)$$

The electric field generates not only electrophoresis but also electroosmosis inside the nanopore. Electroosmosis is a fluid motion induced by the movement of counterions accumulated near the surface of a channel.[31] In a typical nanopore experimental condition of pH 7-8, the SiN_x surface has a negative surface charge.[32] Therefore, positive counterions are placed in the electrical double layer near the surface and are forced to move in the opposite direction to the DNA translocation by the same electric field inside the nanopore. Electroosmosis is an essential principle to consider especially in the nanopore experiments, where the narrow pore dimension becomes comparable to that of the electrical double layer.[33] The electroosmotic velocity v_{EOF} can also be physically interpreted, which is shown in Equation 2-2:

$$v_{EOF} = -\frac{\varepsilon \zeta}{\eta} E \quad (2-2)$$

where ε is the permittivity of the medium (water), ζ is the zeta potential of the channel surface, and η is the dynamic viscosity of the medium.[31] Therefore, a DNA molecule inside the nanopore is affected

by both v_{EPH} and v_{EOF}, and the net DNA velocity v_{DNA} at pH 8 can be described as Equation 2−3 and Equation 2−4, considering the directions of each velocity components:

$$v_{DNA} = v_{EPH} + v_{EOF} \quad (2-3)$$

and

$$|v_{DNA}| = |v_{EPH}| - |v_{EOF}|. \quad (2-4)$$

During translocation, the remaining segments of a translocating DNA molecule reside just outside the nanopore (in the *cis* chamber). The residual parts are under a relatively weak influence of electrophoresis and electroosmosis from the weak electric field in the exterior of the nanopore resistor compared to its interior. In addition, the exterior of a nanopore is free of surface that can generate electroosmotic flow. Therefore, these segments can be an additional target of drag to reduce the DNA translocation speed; if an additional channel is placed at the nanopore exterior, the extra electroosmotic flow could be built inside the new channel, acting as another drag for the translocating DNA. Other than the DNA translocation speed, the segments near the nanopore could provide an extra hindrance to the ionic flow through the nanopore when the parts were placed near the nanopore entrance.[34]

In the next section, a structural modification of the solid−state nanopore will be introduced to utilize the remaining segment of a translocating molecule in enhancing the sensitivity of the nanopore detection.

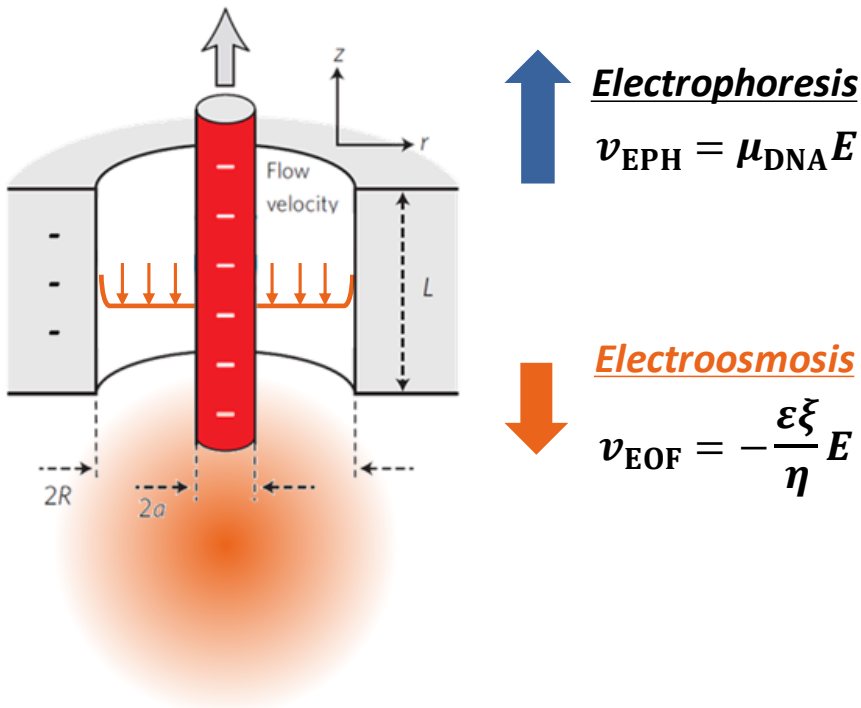

Figure 2-5 Electrophoretic (blue arrow) and electroosmotic (orange arrow) contributions to DNA translocation velocity (gray arrow). The orange area beneath the nanopore indicates the region for potential additional drag on the remaining segments of translocating DNA in the *cis* chamber. Figure was adapted with permission from ref.[23]. Copyright 2009 Springer Nature.

2.2.2 Design of the Guide-Inserted Nanopore Device

To induce the additional drag and the ionic current hindrance on the DNA segments in the *cis* chamber, an effective way would be placing an extra channel underneath the nanopore. A solid-state nanopore device with such a channel, named as 'guide structure' in this work, is schematically presented in Figure 2-6 with the structure of a conventional nanopore device. Both devices had the SiN_x sensing layer in 20-nm thickness, in which a nanopore was individually perforated in ~5-nm diameter. The guide structure was designed to be larger than the sensing nanopore because it should hold the translocating molecules and its electrical resistance should be negligible to that of the sensing nanopore. If the guide structure were formed in a similar dimension to that of the sensing nanopore, the effective voltage drop across the sensing nanopore would be reduced, and so would ΔI.

Specifically, the molecular dimension of DNA was considered in determining the dimensions of the guide structure. 1 kilobase pair (kbp) dsDNA was selected as the target biomolecule in this work, which is a type of biomolecule frequently used in the solid-state nanopore experiments. Since the chain length of 1 kbp dsDNA (340 nm) is larger than the persistence length of dsDNA (~50 nm),[35] the molecule is expected to be in a random conformation in the aqueous environment. Here, the radius of gyration (R_g) of a polymer is the estimated distance between the two ends of the polymer chain when it has a random conformation. Therefore, a free 1 kbp dsDNA molecule can be assumed as a sphere having a radius R_g, which is known to be ~70 nm.[36] In contrast, when it is fully stretched, its length would be 340 nm, same as the chain length L_{chain}.

The guide structure was designed in order that a 1 kbp dsDNA molecule could be fully inserted inside the new channel in any conformation. In conclusion, the length of the guide structure was set as 500 nm, and the width of the channel was targeted to be ~150 nm.

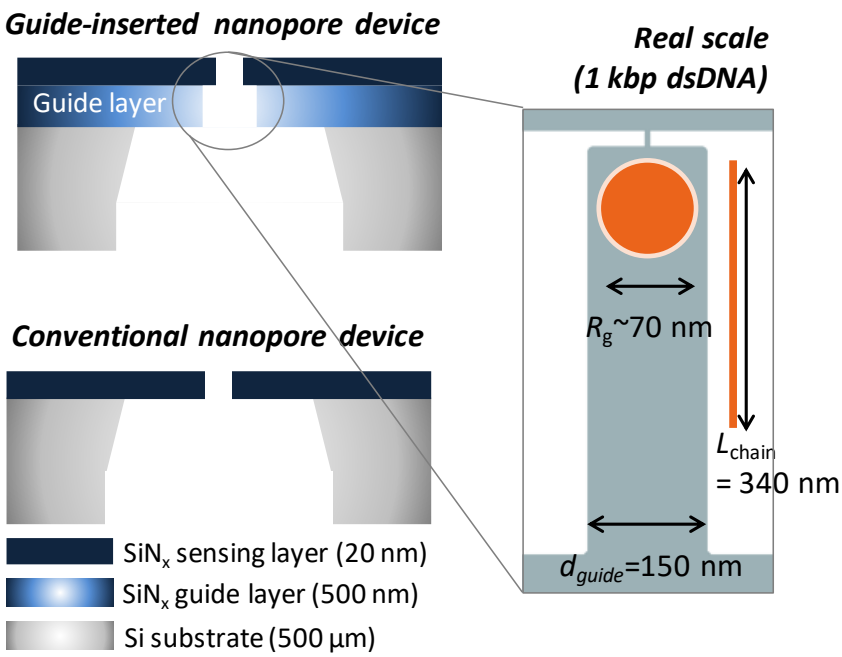

Figure 2-6 Design of guide-inserted nanopore device. The schematics of the guide-inserted and the conventional devices (left, not in scale) with the real scale image of the guide structure and 1 kbp dsDNA molecule (right). Figure was from ref.[1] - Adapted by permission of the Royal Society of Chemistry.

2.2.3 Fabrication Procedure of the Guide-Inserted Nanopore Device

The fabrication process of the guide-inserted nanopore device is illustrated in Figure 2-7. The protocol was set up basically following the standard process to create the conventional Si-substrate nanopore chip. Firstly, 500-nm thick low-stress SiN_x was deposited on the double-side polished 4-inch Si wafer. This film will serve as the guide layer in the completed device. Then, a nanopore chip with a 50 μm x 50 μm freestanding membrane was created using the same process described in section 1.3. The guide structure was formed using a focused ion beam (FIB). Although FIB is an expensive and heavy facility with low accessibility, it was an effective way to pattern a ~150-nm large and straight channel penetrating the 500-nm thick layer. Using gallium ion FIB, it required only ~10 s to form a guide structure per chip.

After forming the guide structure, the additional SiN_x sensing layer was prepared using a process called 'transfer'.[1, 4, 37] For the transfer method, 2 mm x 2 mm SiN_x membrane (100-nm thick) was prepared separately using the same protocol to pattern and expose the freestanding membrane.[4] Inside a bath of deionized water, a membrane chip was put over a target chip (device with the guide structure formed) so that the 100-nm thick membrane and the guide layer would touch each other. The membranes were strongly adhered after fully drying the moisture between the two membranes. As the last step, the Si substrate of the membrane chip could be removed by slightly twisting it from the nanopore chip. The thickness of the membrane chip, 100 nm, was selected to ensure the mechanical stability of the membrane during the transfer process. Therefore, a partial etch process to thin down the sensing layer to ~20 nm was required before perforating the sensing nanopore. In this step, the etch stop was easily controllable by using a mild condition for the dry etch of SiN_x (detailed process will be presented in section 2.3.1). Conventional nanopore devices were fabricated using the protocol explained in section 1.3, starting from the deposition of 20-nm thick low-stress SiN_x film.

Figure 2-8 displays the photograph of the fabricated guide-inserted nanopore device and the TEM images of the guide structure and the sensing nanopore. From the figure, it can be concluded that the guide structure of ~150 nm diameter and the nanopore of 5-7 nm diameter were successfully formed. Likewise, a nanopore of ~5 nm diameter was perforated in each conventional nanopore chip. The completed nanopore devices were examined for their electrical characteristics and DNA detection sensitivities in terms of the signal magnitude and duration in the following sections.

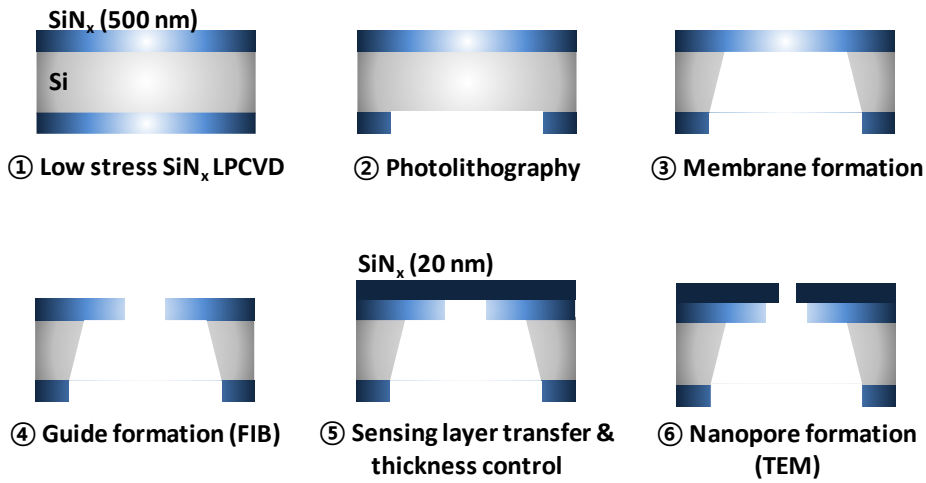

Figure 2-7 Guide-inserted nanopore fabrication process. The detailed process is explained in the text. Images are not in scale.

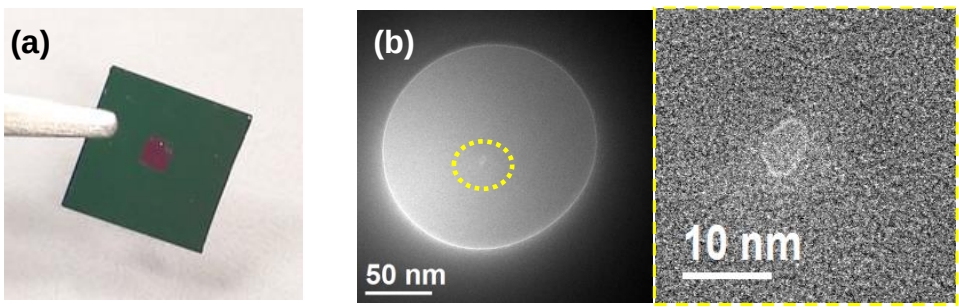

Figure 2-8 Fabricated guide-inserted nanopore device. (a) photograph of the device with the transferred sensing layer in the center of the chip. (b) TEM images of the guide structure with the sensing nanopore in the dashed circle (left) and a close-up TEM image of the sensing nanopore (right). (b) was from ref.[1] – Adapted by permission of the Royal Society of Chemistry.

2.3 Experimental Details

2.3.1 Experimental Details

In the fabrication of the guide-inserted nanopore device, the LPCVD of low-stress SiN_x (500 nm, 100 nm, 20 nm thickness) was conducted by National Nanofab Center (NNFC). Photolithography was performed in hard contact mode for 14 s exposure using MA6 mask aligner (Karl Suss, Garching, Germany) after spin coating hexamethyldisilazane (HMDS, 500 rpm, 10 s – 2000 rpm, 20 s) and AZ5214 photoresist (700 rpm, 10 s – 3800 rpm, 40 s). The pattern was developed using AZ300 developer for 50 s. After thorough rinsing in deionized water and drying, the membrane pattern was etched using Oxford 80Plus Reactive Ion Etcher (Oxford Instruments, Abingdon, UK) under 30 mTorr of tetrafluoromethane (CF_4) gas and 100 W (etch rate: 40-60 nm/min) to expose Si. The remaining photoresist was removed using acetone and the patterned wafer was immersed in 6 M potassium hydroxide (KOH) solution at 78°C temperature for 10 hours to create the freestanding SiN_x membrane.

The guide structure was perforated using Helios NanoLab 650 (FEI Company, Hillsboro, USA), with the target size set as 120 nm. In the FIB setup used in this work, slightly large patterns were created than the target pattern drawn in the program. The exact size of the guide structure was checked by TEM imaging before proceeding to the next fabrication step. The transfer process of the sensing layer was performed as explained in section 2.2.3. The transferred layer was partially etched to the final thickness of 20 nm, using dry etch condition with 30 mTorr CF_4 and a mild power of 40 W (etch rate: ~15 nm/min) for better thickness controllability. The sensing nanopore was fabricated using a JEOL 2010F transmission electron microscope (JEOL, Tokyo, Japan).

After fabrication, the nanopore devices were assembled with the custom-made Teflon® flow cells and connected to Axon Axopatch 200B Microelectrode Amplifier (Molecular Devices, San

Jose, USA) as described in section 1.2 and Figure 1-4. 1 M KCl (Bioneer, Daejeon, Korea) buffered using 1X Tris-HCl EDTA (TE, pH 8.0, Sigma Aldrich, St. Louis, USA) was inserted in the flow cell to form an ionic circuit through the nanopore. The sampling frequency of the current amplifier was 250 kHz and 10 kHz bandwidth lowpass Bessel filter was digitally applied to process the recorded signals. For the electrical noise characterization of the devices, 0 mV and 100 mV were applied to each device and the ionic current was recorded for 10 s in each run. To convert the ionic current trace to a PSD curve, FFT of the ionic current recording was performed using Clampfit® software provided by the manufacturer of the current amplifier. The applied voltage was swept from −100 mV to +100 mV to measure the ionic conductance of the devices.

For the DNA translocation experiment, 1 nM of 1 kbp DNA in the buffered 1 M KCl solution (pH 8.0) was injected in the *cis* chamber. 150, 250, 300, and 400 mV was applied in the direction that the DNA molecules would pass through the guide structure before entering the sensing nanopore. The DNA translocation signals were collected and analyzed using Clampfit®. The threshold ΔI for translocation was determined based on the geometrical analysis by Carlsen *et al.*[34] Here, the event peak magnitudes formed several Gaussian distributions, and only the Gaussians with the center magnitude larger than the threshold were approved as the real translocation events. This process was conducted to eliminate the signals from bouncing, which is a group of false events without relocation of DNA molecules to the *trans* chamber.[34]

2.3.2 Finite Element Method Simulation of the Electrokinetic Environment Surrounding the Nanopore

(simulations conducted by Professor Hyomin Lee and Professor Sung Jae Kim, Department of Electrical and Computer Engineering, SNU)

In order to analyze the electrokinetic environment near the nanopore, the guide structure, and the translocating DNA molecule, finite element method (FEM) simulations were conducted using COMSOL Multiphysics® 4.3 software. In a cylindrical coordinate system, the geometry was built as the same as the structures of the actual guide-inserted nanopore device and the conventional nanopore device, as depicted in Figure 2-9. Governing equations for the 3 physical models (electrostatics, transport of the diluted species, creeping flow) and the continuity equation are listed below:

$$-\varepsilon\nabla^2\psi = F(c_+ - c_-) \tag{2-5}$$

$$-\nabla\cdot\left(-D_\pm\nabla c_\pm \mp \frac{FD_\pm}{RT}c_\pm\nabla\psi + c_\pm\mathbf{u}\right) = 0 \tag{2-6}$$

$$-\nabla p + \eta\nabla^2\mathbf{u} - F(c_+ - c_-)\nabla\psi = 0 \tag{2-7}$$

and

$$\nabla\cdot\mathbf{u} = 0 \tag{2-8}$$

where ψ is the electric potential, F is the Faraday constant, c_+ and c_- are concentrations of the cation and the anion, $D_\pm$ is the diffusivity of each ionic species, R is the gas constant, T is the absolute temperature, $\mathbf{u}$ is the flow field, and p is the hydrodynamic gauge pressure. The equations are Poisson equation (2-5), Nernst-Planck equation (2-6), Stokes equation (2-7) and the continuity equation (2-8). The boundary conditions on the SiN_x nanopore surface were modeled as described in Equation 2-9, Equation 2-10, and Equation 2-11:

$$-\mathbf{n}\cdot\varepsilon\nabla\psi = q_s \tag{2-9}$$

$$\mathbf{n}\cdot\left(-D_{\pm}\nabla c_{\pm} \mp \frac{FD_{\pm}}{RT}c_{\pm}\nabla\psi + c_{\pm}\mathbf{u}\right) = 0 \tag{2-10}$$

and

$$\mathbf{n}\cdot\mathbf{u} = \mathbf{t}\cdot\mathbf{u} = 0 \tag{2-11}$$

where $\mathbf{n}$ is the outward normal vector on the surface, q_s is the surface charge density of the nanopore at pH 8 (−5 mC/m^2),[32] and $\mathbf{t}$ is the tangential vector on the surface. Each equation represents the surface charge density of the SiN_x surface (2−9), no penetration of ionic species (2−10) and no slip condition for fluid flow (2−11). The reservoir boundary conditions on each chamber are explained in Equation 2−12, Equation 2−13, and Equation 2−14:

$$\psi = V_{app} \tag{2-12}$$

$$c_{\pm} = c_0 \tag{2-13}$$

and

$$p = 0 \tag{2-14}$$

where V_{app} is the applied voltage and c_0 is the bulk ionic concentration.

The remaining segment of a translocating 1 kbp dsDNA molecule was modeled as a hard sphere of 70 nm radius inside the guide structure (guide−inserted device) or outside the sensing nanopore (conventional device). The geometry of the model including the DNA molecule is graphically presented in Figure 2−9(b) and Figure 2−9 (d).

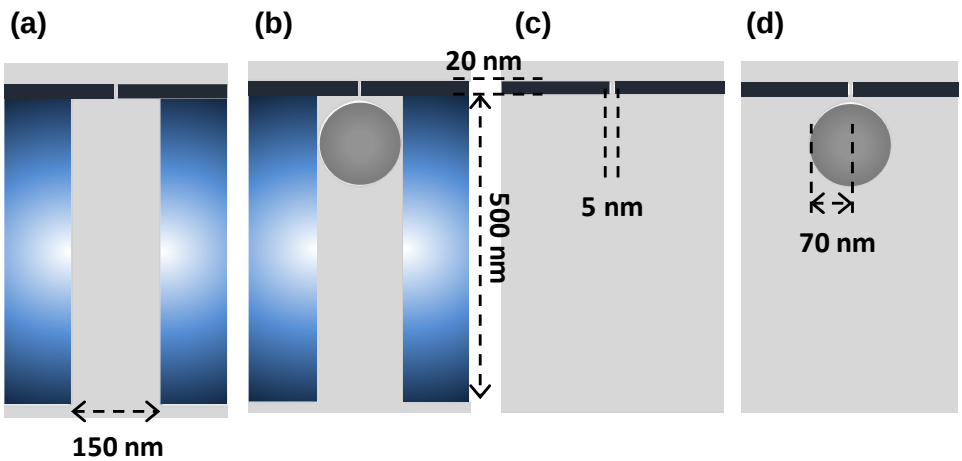

Figure 2-9 Geometrical setup of FEM simulation in the nanopore region. (a)-(b) cross-section images of the modeled guide-inserted nanopore device (a) without and (b) with a 1 kbp dsDNA molecule inserted (gray circle). The solid layers indicate the sensing membrane, where the layers with a color gradient denote the guide layer. (c)-(d) the cross-section images of the conventional nanopore device are shown (c) without and (d) with the DNA molecule. Figures were from ref.[1] - Adapted by permission of the Royal Society of Chemistry.

2.3.3 Physical Analysis of the DNA Translocation Time Data

To physically figure out the DNA translocation velocity from the t_d data, it should be fitted to a translocation probability function of time t. The derivation of this function starts from the assumption of 1 dimensional (1−D) biased diffusion, where the thermal diffusion and the external bias (applied voltage in nanopore experiments) simultaneously affect the movement of a particle.[9, 38] The partial differential equation explaining this condition is shown in Equation 2−15 (Fokker−Planck equation):

$$\frac{\partial P(x,t)}{\partial t} = D\frac{\partial^2 P(x,t)}{\partial x^2} - v\frac{\partial P(x,t)}{\partial x} \qquad (2-15)$$

where $P(x,t)$ is the probability of DNA at position x and time t, and D and v are the diffusion constant and the drift velocity of the DNA inside the pore, respectively.[38]

Figure 2−10 illustrates the 1−D DNA translocation situation in this model. DNA starts to translocate from the nanopore positioned at x=0, and a DNA translocation is complete when the DNA reaches x=L, where L is the chain length of the translocating DNA. Therefore, the boundary conditions of Equation 2−15 can be described as below:

$$P(x,0) = \delta(x) \qquad (2-16)$$

and

$$P(L,t) = 0. \qquad (2-17)$$

This form of Fokker−Planck equation was solved by Schrödinger, and the solution is presented in Equation 2−18:

$$P(x,t) = \frac{1}{\sqrt{4\pi Dt}}\left\{\exp\frac{-(x-vt)^2}{4Dt} - A\exp\frac{-(x-2L-vt)^2}{4Dt}\right\} \qquad (2-18)$$

where $A = \mathrm{e}^{\left(\frac{vL}{D}\right)}$.[38]

Meanwhile, $1-\int_{-\infty}^{L} P(x,t)\mathrm{d}x$ is the probability of DNA that would have finished translocation until time t. Therefore, $F(t)$, the translocation probability function at time t, can be explained as Equation 2−19:[38]

$$F(t) = -\frac{\mathrm{d}}{\mathrm{dt}}\int_{-\infty}^{L} P(x,t)\mathrm{d}x = \frac{L}{\sqrt{4\pi D t^3}}\exp\frac{-(L-vt)^2}{4Dt}. \qquad (2-19)$$

By fitting F(t) to the translocation time histogram with a known L, the unknown parameters v and D can be extracted. D is an indicator of the fluctuations in the velocity during translocations, but it is only occasionally studied in nanopore research. The key factor here is the translocation velocity v, which will be extracted from the experimental data and discussed in section 2.4.4.

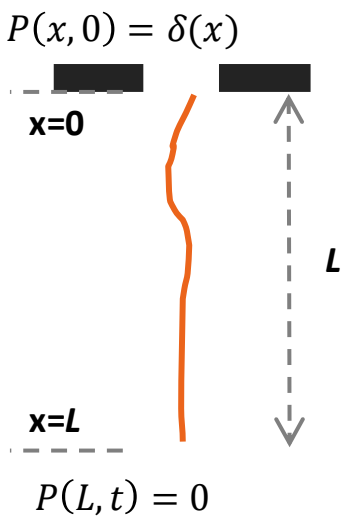

Figure 2-10 1-D biased diffusion model with the nanopore at x=0 and the absorbing boundary at x=L, where L is the DNA chain length. The boundary conditions at (x,t)=(x,0) and (L,t) are indicated.

2.4 Result and Discussion

2.4.1 Electrical Characteristics of the Guide-Inserted Nanopore Device

Before analyzing the effect of the guide structure to DNA translocation signals, the electrical characteristics of the guide-inserted nanopore device were examined. Figure 2-11 summarizes the $I-V$ relationship and the electrical noise PSD curve of the guide-inserted and the conventional nanopore devices. Both devices exhibited a linear $I-V$ curve following Ohm's law (Figure 2-11(a)). From Equation 1-1, the nanopore diameter could be calculated from the slope of the $I-V$ graph: 5.5 nm for the guide-inserted nanopore and 4.9 nm for the conventional nanopore. The calculated diameters corresponded to the physical diameters of 5 nm imaged using TEM right after perforation. In addition, the presence of the guide structure was ineffective in reducing the ionic conductance of the sensing nanopore, agreeing to the design factor discussed in section 2.2.2.

Figure 2-11(b) shows the electrical noise powers of the guide-inserted and the conventional nanopore devices as functions of frequency. The characteristics were similar to the typical electrical noise of the Si-substrate nanopore device. The measured I_{rms} of the devices in this work were 25-30 pA (guide-inserted) and 40-50 pA (conventional) with a 10 kHz lowpass filter applied. The reduction of I_{rms} in the guide-inserted device would have been originated from the enhanced mechanical stability of the thick membrane. Therefore, the presence of the guide structure in the nanopore device was beneficial for high SNR of DNA detection in terms of the noise.

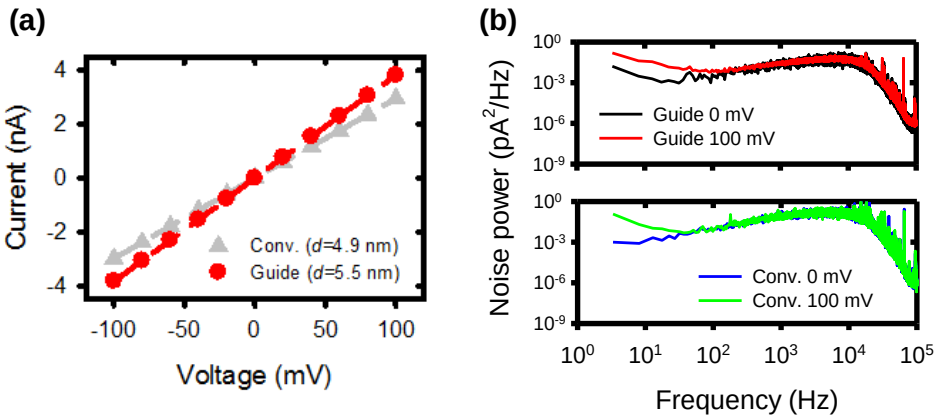

Figure 2-11 Electrical characteristics of the guide-inserted and the conventional nanopore devices. (a) *I*-*V* curve of the guide-inserted (red dots and line) and the conventional (gray triangles and line) nanopore. Nanopore diameters calculated with Equation 1-1 are marked in the legend. (b) noise PSD curves of the guide-inserted (black: 0 mV, red: 100 mV) and the conventional (blue: 0 mV, green: 100 mV) nanopore device. Figures were from ref.[1]- Reproduced by permission of the Royal Society of Chemistry.

2.4.2 DNA Translocation Results in the Guide-Inserted and the Conventional Solid-State Nanopore Devices

Figure 2-12 summarizes the 1 kbp dsDNA translocation results from the guide-inserted and the conventional nanopore devices. In the raw $I-t$ signals, the guide-inserted nanopore device showed a narrower baseline current band (low electrical noise, as discussed in section 2.4.1) and larger peak signal depth than the conventional device. The information of each peak, signal magnitude ΔG and duration t_d, were collected and analyzed to construct the scatter plots. Here, $\Delta G = \frac{\Delta I}{V}$ indicated signal magnitude normalized to the applied voltage. The numbers of DNA translocations detected in each condition were 660, 1309, 607, and 557 (150, 250, 300, and 400 mV) in the guide-inserted device and 587, 1117, 942, and 438 (150, 250, 300, and 400 mV) in the conventional device.

From the scatter plots in Figure 2-12(c), Figure 2-12(d), and Figure 2-12(e), larger ΔG and t_d in the guide-inserted device than in the conventional device were identifiable as expected. However, this difference was indistinguishable under 400 mV (Figure 2-12(f)). In the next sections, the improvements will be statistically and quantitatively discussed with the physical interpretations of the guide structure effect on the translocation signals.

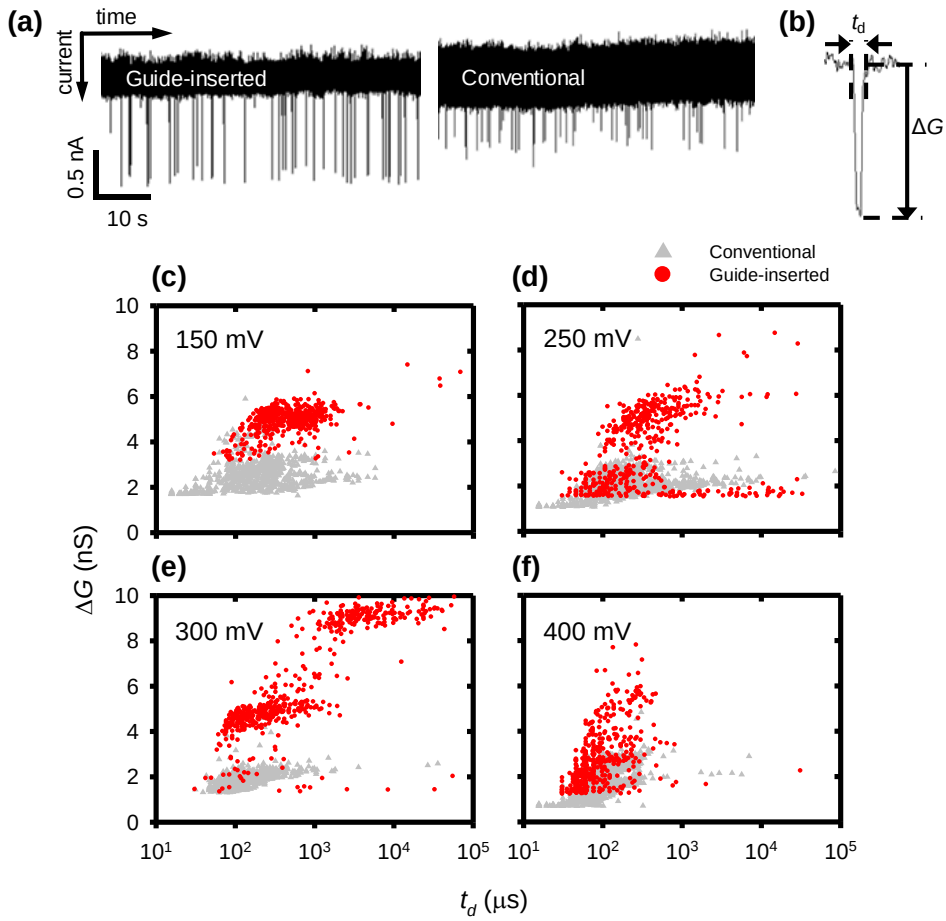

Figure 2-12 DNA translocation results in the guide-inserted and conventional nanopore. (a) raw ionic current traces of DNA translocations detected in the guide-inserted (left) and the conventional (right) devices. (b) a model DNA translocation signal with a signal magnitude ΔG and a duration t_d. (c)-(f) scatter plots of the translocation events through the guide-inserted (red dots) and the conventional (gray triangles) nanopores observed at (c) 150, (d) 250, (e) 300, and (f) 400 mV. Figures were from ref.[1] - Reproduced by permission of the Royal Society of Chemistry.

2.4.3 SNR Enhancement Effect in the Guide-Inserted Nanopore Device

To analyze the effect of the guide structure to SNR in detail, the ΔG information in Figure 2-12 was reconstructed in histograms as in Figure 2-13. Since the numbers of data points were different in all conditions, the histogram bar heights were normalized so that the maximum count would be 1. As briefly presented in the scatter plots in Figure 2-12, the guide-inserted device produced translocation signals with a larger ΔG than the conventional devices at 150-300 mV. The large signals formed extra distributions centered at 4-5 nS, positioned at 2-3 nS higher ΔG than that from the conventional device. Meanwhile, the expected ΔG calculated geometrically from the same assumption in section 1-2 was ~2.5 nS,[39] corresponding to the distributions from the conventional device centered at 2-2.5 nS at all voltages.

FEM simulation explained in section 2.3.2 was conducted to investigate the origin of the ΔG increase in the guide-inserted nanopore device. Figure 2-14 illustrates the electric field distributions near the nanopore with and without the guide structure (Figure 2-14(a)) and with a 1 kbp dsDNA molecule placed near the sensing nanopore of both devices (Figure 2-14(b)). This sphere represented the remaining segment of DNA in the *cis* chamber during translocation, assuming it had a random conformation inside the guide structure larger than its size (guide-inserted) and in free space (conventional). In the simulation results, the magnitude of the electric field was diminished as the distance from the nanopore resistor increased. Nevertheless, when the extra guide layer was present, the relatively strong electric field of 10^4-10^5 V/m was maintained inside the guide structure. Therefore, the translocating DNA molecule would be under a stronger electric field inside the guide structure than when it approaches the nanopore in the conventional device.

Based on this simulation, the distance of the DNA molecule to the sensing layer was changed from 100 nm to 0 nm, assuming the situation when a DNA molecule moved nearer to the sensing

nanopore for translocation. The calculated ΔG as a function of the distance in both device structures are presented in Figure 2-15(a). From the simulation, ΔG from the guide-inserted device was higher than that from the conventional device in all distances. Particularly, the guide structure produced excess ΔG of 1.3 nS even when a DNA molecule was placed at the 100 nm position from the sensing nanopore. This implied that the guide structure acted as geometrical confinement not only for DNA but also for ions when DNA approached to the sensing nanopore.

The geometrical hindrance effect of the guide structure also could be found in the DNA translocation experiment in the guide-inserted nanopore using 10 kbp dsDNA. 10 kbp dsDNA has an R_g of ~190 nm and a chain length of 3400 nm. Therefore, this molecule could enter to the guide structure only if it was partly or fully unthreaded. Comparing Figure 2-15(b) and Figure 2-13(c) obtained using the same guide-inserted device under 150 mV, the fraction of the large signals of 4-6 nS ΔG was smaller in 10 kbp dsDNA than in 1 kbp dsDNA. In other words, the geometrical confinement or hindrance effect was reduced in the larger, unthreaded molecule; thus, the guide structure was less effective in increasing the SNR in overall for the large target.

To summarize, ΔG was increased from the extra ionic current hindrance by the DNA segments inside the guide structure, where the width of the confinement was comparable to the size of the DNA random coil. However, this effect (~1.3 nS increase) partly explained the total ΔG increase (2-3 nS) in the guide-inserted nanopore. Additionally, the unraveling process of DNA in the nanopore entrance should be considered with the analysis of the remaining DNA segment to fully explain this phenomenon. In spite of the disagreement in the numbers, the electrokinetic analysis with the rigid sphere modeling of DNA was the key to understand the essential effect of the guide structure on the translocation signal magnitude.

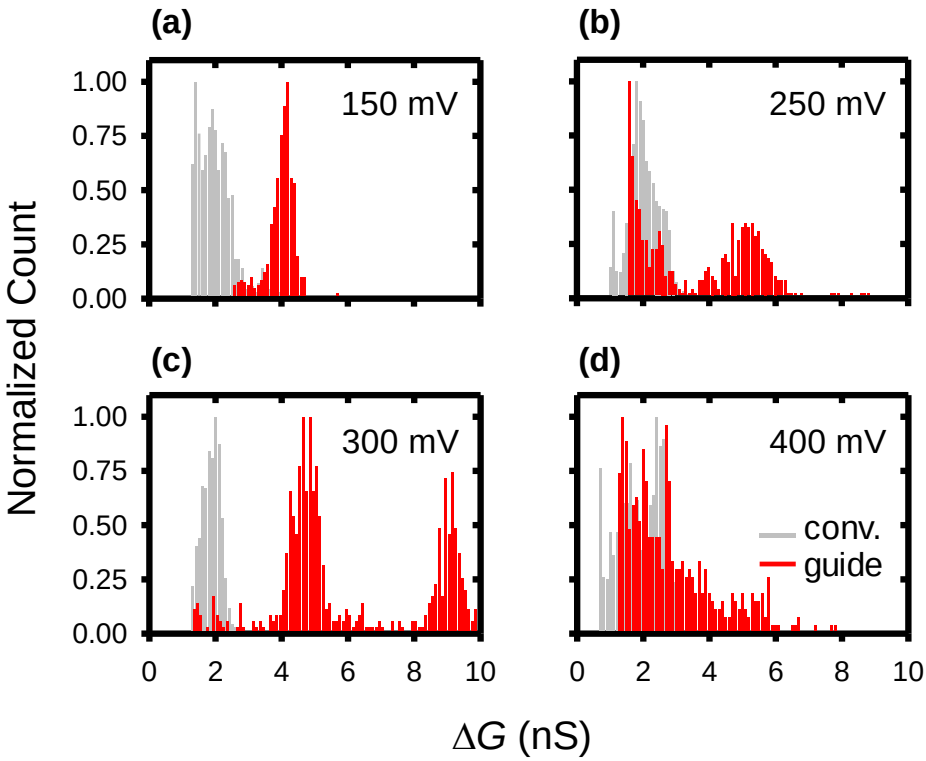

Figure 2-13 Translocation ΔG in the guide-inserted and the conventional nanopore device. ΔG histograms obtained at (a) 150 mV, (b) 250 mV, (c) 300 mV, and (d) 400 mV from the guide-inserted (red bars) and the conventional (gray bars) devices. Figures were from ref.[1] - Adapted by permission of the Royal Society of Chemistry.

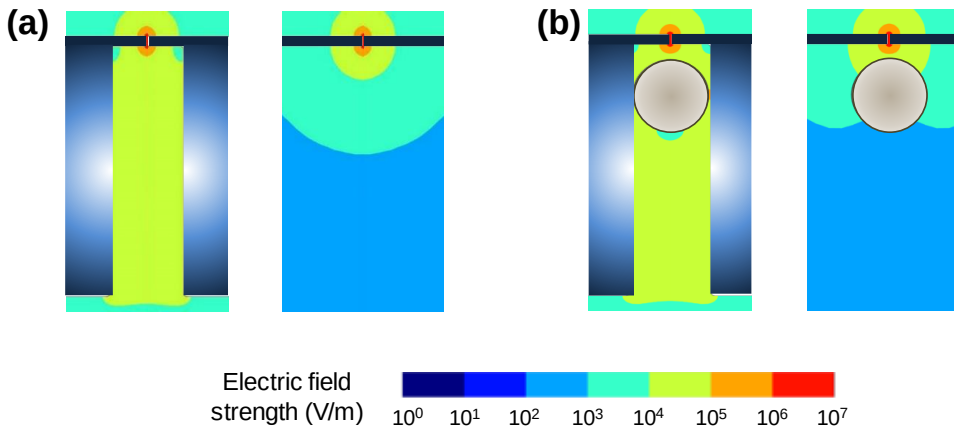

Figure 2-14 Electric field simulation results in the nanopore region using FEM. Electric field contour map (a) without and (b) with 1 kbp dsDNA molecule modeled as a hard sphere (gray circle) in the guide-inserted (left) and the conventional (right) nanopore devices. The electric field strength color scale is marked at the bottom. Figures were from ref.[1] - Reproduced by permission of the Royal Society of Chemistry.

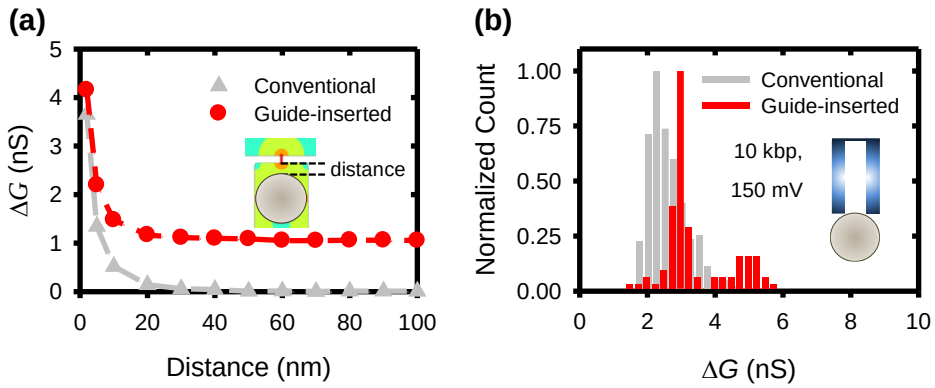

Figure 2-15 Effect of the guide structure to Δ*G*. (a) calculated Δ*G* as a function of the distance between the sensing nanopore and the 1 kbp dsDNA molecule in the guide-inserted (red dots and line) and the conventional (gray triangle and line) devices. (b) histogram of Δ*G* of 10 kbp dsDNA detected at 150 mV in the guide-inserted (red bars) and the conventional (gray bars) nanopore devices. Figures were from ref.[1] - Adapted by permission of the Royal Society of Chemistry.

2.4.4 DNA Retardation Effect in the Guide-Inserted Nanopore Device

The scatter plots in Figure 2-12 were rearranged to the translocation time histograms in Figure 2-16. Here, the histogram count normalization was conducted for the curve fitting explained in section 2.3.3, to make the total area of the histogram in each condition to be 1.

Like in the previous section, the flow fields near the nanopore were simulated in the guide-inserted device and the conventional device as in Figure 2-17. The flow field distribution was similar to the electric field distribution in Figure 2-14; the field magnitude diminished with the distance from the nanopore, and a moderate level of the field was maintained inside the guide structure. By principle, the trend of the electric field and the flow field distributions should be similar because the electroosmotic velocity is proportional to the electric field (Equation 2-2). It is clear from the flow field map that the guide structure was successful in generating the intrinsic electroosmotic flow near the sensing nanopore, which would act as an additional drag exerted to a translocating DNA molecule

Therefore, to quantitatively figure out the extra electroosmotic flow effect, the net translocation velocity ratio in the guide-inserted and the conventional devices was calculated. The velocity terms exerted on the remaining segment of a translocating DNA are graphically described in Figure 2-18. Here, electrophoresis ($v_{\mathrm{EPH,guide}}$) and electroosmosis ($v_{\mathrm{EOF,guide}}$) were taken into account in calculating the net DNA velocity in the guide structure, $v_{\mathrm{net,guide}}$, whereas only electrophoresis ($v_{\mathrm{EPH,conv}}$) was considered in the net translocation velocity in the conventional device, $v_{\mathrm{net,conv}}$:

$$\frac{v_{\mathrm{net,guide}}}{v_{\mathrm{net,conv}}} = \frac{v_{\mathrm{EPH,guide}} - v_{\mathrm{EOF,guide}}}{v_{\mathrm{EPH,conv}}}. \qquad (2-20)$$

Using Equation 2-1, Equation 2-2, and the electric field and the flow field from the FEM simulations, Equation 2-20 could be calculated. The calculated $\frac{v_{\mathrm{net,guide}}}{v_{\mathrm{net,conv}}}$ value was 0.79, which well corresponded to

the experimental value determined from the curve fitting of $F(t)$. Therefore, the retardation of DNA translocation in the guide-inserted device originated from the extra $v_{EOF,guide}$, which was exerted on the remaining DNA segment during translocation.

In conclusion, the strong intrinsic electroosmotic flow inside the guide structure could effectively reduce the DNA translocation speed by 21% compared to the conventional nanopore device. However, at 400 mV, the effect of the guide structure to increase ΔG and reduce v was unidentified in the experimental results. This observation would be due to the conformation change of the DNA molecule at high voltage; as the electric field gets stronger, the charged DNA molecules are more likely to be in its unthreaded shape than in a random conformation.[36] Therefore, the real situation at 400 mV would be out of the rigid sphere model of DNA taken in this analysis. Still, the model well explained the ion confinement and the electroosmosis effects in enhancing nanopore sensitivities under the normal voltage conditions of DNA analysis.

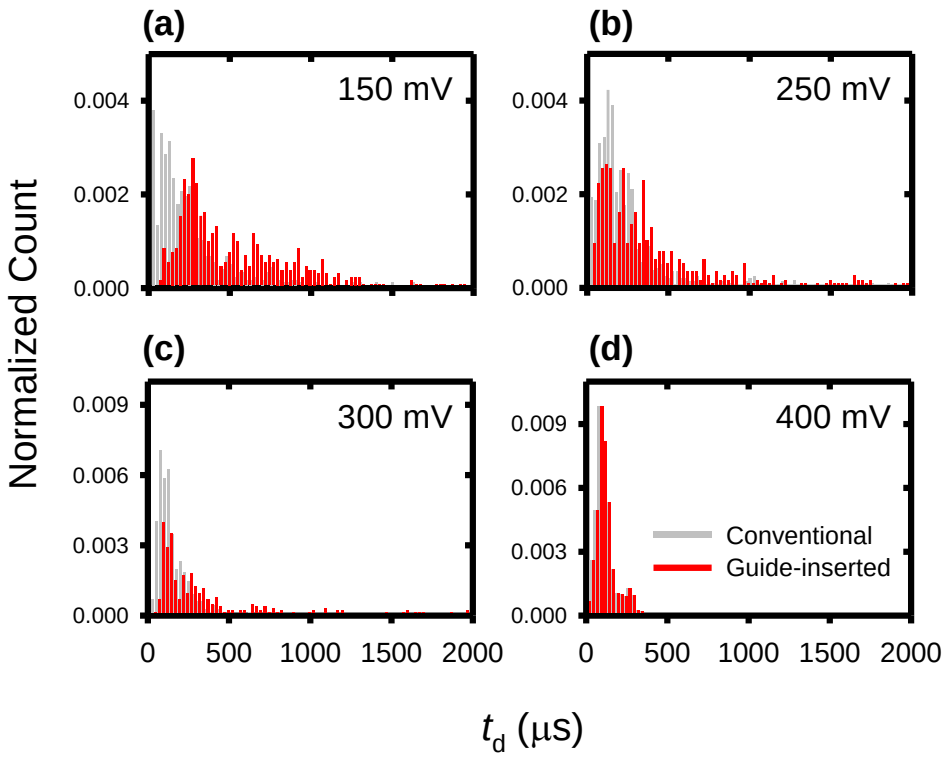

Figure 2-16 Translocation t_d in the guide-inserted and the conventional nanopore device. t_d histograms obtained at (a) 150 mV, (b) 250 mV, (c) 300 mV, and (d) 400 mV from the guide-inserted (red bars) and the conventional (gray bars) devices. Figures were from ref.[1] - Adapted by permission of the Royal Society of Chemistry.

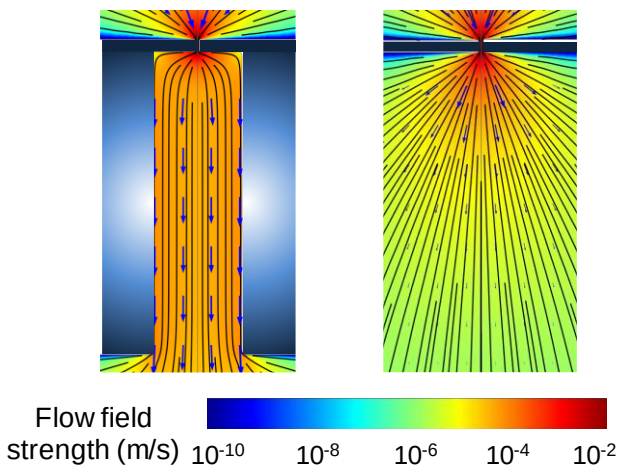

Figure 2-17 Flow field simulation results in the nanopore region using FEM. Flow field map in the guide-inserted (left) and the conventional (right) nanopore device with the blue arrows indicating the direction and the relative magnitudes of the flow. The flow field strength color scale is marked at the bottom. Figures were from ref.[1] - Reproduced by permission of the Royal Society of Chemistry.

Figure 2-18 Velocity contributions to a translocating DNA in the nanopores. The velocity terms explained in the text and their directions are marked on 1 kbp dsDNA molecules (gray circles) approaching the sensing layer in the guide-inserted (left) and the conventional (right) nanopore devices. The images are not in scale. Figures were from ref.[1] - Adapted by permission of the Royal Society of Chemistry.

2.5 Conclusion

In this chapter, a structural modification was introduced in the conventional Si-substrate nanopore to increase the DNA detection sensitivity in terms of the signal magnitude and the translocation velocity. A 500-nm thick and 150-nm wide guide structure was designed to generate extra confinement to the ions and an additional drag force to translocating DNA molecules. The objective was experimentally and numerically proved from the DNA translocation results and the FEM simulations. In summary, the guide structure induced ionic transport hindrance when a DNA molecule of comparable size to the guide structure translocated, and the electroosmotic flow built inside the guide structure acted as a drag to a translocating DNA molecule.

The major significance of this work corresponded to the major goal of this thesis; the detection sensitivity issue was examined in a view of the electrokinetics and the device structure. The design and the analysis of the guide structure effect were successfully conducted with the considerations on electrophoresis and electroosmosis principles. Furthermore, this work provided the first experimental evidence that the segments of a translocating DNA remaining in the *cis* chamber can be a target of the fluid drag to slow down the DNA translocations. The effect of the drag in the *cis* chamber had been indefinitely mentioned as a possible factor for controlling DNA translocation speed or numerically studied using Langevin dynamics.[40] The results in this chapter suggested that controlling the drag in *cis* chamber could be powerful in reducing the DNA translocation speed, and the speed could be further reduced using more delicate control on the fluid drag exerted on these segments.

References

1. Lee, K.; Lee, H.; Lee, S.-H.; Kim, H.-M.; Kim, K.-B.; Kim, S. J., Enhancing the sensitivity of DNA detection by structurally modified solid-state nanopore. *Nanoscale* 2017, *9* (45), 18012-18021.

2. Lee, K.; Park, K. B.; Kim, H. J.; Yu, J. S.; Chae, H.; Kim, H. M.; Kim, K. B., Recent Progress in Solid-State Nanopores. *Advanced Materials* 2018, *30* (42), 1704680.

3. Feng, J.; Liu, K.; Bulushev, R. D.; Khlybov, S.; Dumcenco, D.; Kis, A.; Radenovic, A., Identification of single nucleotides in MoS2 nanopores. *Nat. Nanotechnol.* 2015, *10* (12), 1070-6.

4. Yu, J.-S.; Hong, S. C.; Wu, S.; Kim, H.-M.; Lee, C.; Lee, J.-S.; Lee, J. E.; Kim, K.-B., Differentiation of selectively labeled peptides using solid-state nanopores. *Nanoscale* 2019, *11* (5), 2510-2520.

5. Park, K.-B.; Kim, H.-J.; Kim, H.-M.; Han, S. A.; Lee, K. H.; Kim, S.-W.; Kim, K.-B., Noise and sensitivity characteristics of solid-state nanopores with a boron nitride 2-D membrane on a pyrex substrate. *Nanoscale* 2016, *8* (10), 5755-5763.

6. Kumar, A.; Park, K.-B.; Kim, H.-M.; Kim, K.-B., Noise and its reduction in graphene based nanopore devices. *Nanotechnology* 2013, *24* (49), 495503.

7. Fologea, D.; Uplinger, J.; Thomas, B.; McNabb, D. S.; Li, J., Slowing DNA translocation in a solid-state nanopore. *Nano Letters* 2005, *5* (9), 1734-1737.

8. Carson, S.; Wilson, J.; Aksimentiev, A.; Wanunu, M., Smooth DNA Transport through a Narrowed Pore Geometry. *Biophysical journal* 2014, *107* (10), 2381-2393.

9. Jiali, L.; David, S. T., The distribution of DNA translocation times in solid-state nanopores. *Journal of Physics: Condensed Matter* 2010, *22* (45), 454129.

10. Garaj, S.; Liu, S.; Golovchenko, J. A.; Branton, D.,

Molecule-hugging graphene nanopores. *Proceedings of the National Academy of Sciences of the United States of America* 2013, *110* (30), 12192-12196.

11. Smeets, R. M.; Keyser, U. F.; Krapf, D.; Wu, M.-Y.; Nynke, H.; Dekker, C., Salt dependence of ion transport and DNA translocation through solid-state nanopores. *Nano Letters* 2006, *6* (1), 89-95.

12. Rodríguez-Manzo, J. A.; Puster, M.; Nicolaï, A.; Meunier, V.; Drndić, M., DNA Translocation in Nanometer Thick Silicon Nanopores. *ACS Nano* 2015, *9* (6), 6555-6564.

13. Yanagi, I.; Fujisaki, K.; Hamamura, H.; Takeda, K., Thickness-dependent dielectric breakdown and nanopore creation on sub-10-nm-thick SiN membranes in solution. *Journal of Applied Physics* 2017, *121* (4), 045301.

14. Yanagi, I.; Ishida, T.; Fujisaki, K.; Takeda, K.-i., Fabrication of 3-nm-thick Si3N4 membranes for solid-state nanopores using the poly-Si sacrificial layer process. *Scientific reports* 2015, *5* (1), 14656.

15. Garaj, S.; Hubbard, W.; Reina, A.; Kong, J.; Branton, D.; Golovchenko, J. A., Graphene as a subnanometre trans-electrode membrane. *Nature* 2010, *467* (7312), 190-193.

16. Schneider, G. F.; Kowalczyk, S. W.; Calado, V. E.; Pandraud, G.; Zandbergen, H. W.; Vandersypen, L. M. K.; Dekker, C., DNA Translocation through Graphene Nanopores. *Nano Letters* 2010, *10* (8), 3163-3167.

17. Zhou, Z.; Hu, Y.; Wang, H.; Xu, Z.; Wang, W.; Bai, X.; Shan, X.; Lu, X., DNA Translocation through Hydrophilic Nanopore in Hexagonal Boron Nitride. *Scientific reports* 2013, *3* (1), 3287.

18. Liu, S., *et al.*, Boron Nitride Nanopores: Highly Sensitive DNA Single-Molecule Detectors. *Advanced Materials* 2013, *25* (33), 4549-4554.

19. Liu, K.; Feng, J.; Kis, A.; Radenovic, A., Atomically Thin Molybdenum Disulfide Nanopores with High Sensitivity for DNA Translocation. *ACS Nano* 2014, *8* (3), 2504-2511.

20. Waduge, P., *et al.*, Direct and Scalable Deposition of

Atomically Thin Low-Noise MoS2 Membranes on Apertures. *ACS Nano* 2015, *9* (7), 7352-9.

21. Kowalczyk, S. W.; Wells, D. B.; Aksimentiev, A.; Dekker, C., Slowing down DNA Translocation through a Nanopore in Lithium Chloride. *Nano Letters* 2012, *12* (2), 1038-1044.

22. Keyser, U. F.; Does, J. v. d.; Dekker, C.; Dekker, N. H., Optical tweezers for force measurements on DNA in nanopores. *Review of Scientific Instruments* 2006, *77* (10), 105105.

23. van Dorp, S.; Keyser, U. F.; Dekker, N. H.; Dekker, C.; Lemay, S. G., Origin of the electrophoretic force on DNA in solid-state nanopores. *Nature Physics* 2009, *5* (5), 347-351.

24. Hyun, C.; Kaur, H.; Rollings, R.; Xiao, M.; Li, J., Threading Immobilized DNA Molecules through a Solid-State Nanopore at >100 μs per Base Rate. *ACS Nano* 2013, *7* (7), 5892-5900.

25. Liu, Y.; Yobas, L., Slowing DNA Translocation in a Nanofluidic Field-Effect Transistor. *ACS Nano* 2016, *10* (4), 3985-3994.

26. Banerjee, S.; Wilson, J.; Shim, J.; Shankla, M.; Corbin, E. A.; Aksimentiev, A.; Bashir, R., Slowing DNA Transport Using Graphene-DNA Interactions. *Advanced Functional Materials* 2015, *25* (6), 936-946.

27. Larkin, J.; Henley, R.; Bell, D. C.; Cohen-Karni, T.; Rosenstein, J. K.; Wanunu, M., Slow DNA transport through nanopores in hafnium oxide membranes. *ACS Nano* 2013, *7* (11), 10121-8.

28. Squires, A. H.; Hersey, J. S.; Grinstaff, M. W.; Meller, A., A nanopore-nanofiber mesh biosensor to control DNA translocation. *Journal of the American Chemical Society* 2013, *135* (44), 16304-7.

29. Tang, Z.; Liang, Z.; Lu, B.; Li, J.; Hu, R.; Zhao, Q.; Yu, D., Gel mesh as "brake" to slow down DNA translocation through solid-state nanopores. *Nanoscale* 2015, *7* (31), 13207-14.

30. Keyser, U. F.; Koeleman, B. N.; van Dorp, S.; Krapf, D.; Smeets, R. M. M.; Lemay, S. G.; Dekker, N. H.; Dekker, C., Direct force measurements on DNA in a solid-state nanopore. *Nature Physics* 2006, *2* (7), 473-477.

31. Firnkes, M.; Pedone, D.; Knezevic, J.; Döblinger, M.; Rant, U., Electrically Facilitated Translocations of Proteins through Silicon Nitride Nanopores: Conjoint and Competitive Action of Diffusion, Electrophoresis, and Electroosmosis. *Nano Letters* 2010, *10* (6), 2162-2167.

32. Sonnefeld, J., Determination of surface charge density parameters of silicon nitride. *Colloids and Surfaces A: Physicochemical and Engineering Aspects* 1996, *108* (1), 27-31.

33. Daiguji, H., Ion transport in nanofluidic channels. *Chemical Society reviews* 2010, *39* (3), 901-11.

34. Carlsen, A. T.; Zahid, O. K.; Ruzicka, J.; Taylor, E. W.; Hall, A. R., Interpreting the conductance blockades of DNA translocations through solid-state nanopores. *ACS Nano* 2014, *8* (5), 4754-60.

35. Stellwagen, E.; Stellwagen, N. C., Determining the electrophoretic mobility and translational diffusion coefficients of DNA molecules in free solution. *Electrophoresis* 2002, *23* (16), 2794-2803.

36. Chen, P.; Gu, J.; Brandin, E.; Kim, Y.-R.; Wang, Q.; Branton, D., Probing Single DNA Molecule Transport Using Fabricated Nanopores. *Nano Letters* 2004, *4* (11), 2293-2298.

37. 김기범, 유재석, 김형준 나노포어 구조체, 나노포어 구조를 이용한 이온소자 및 나노멤브레인 구조체 제조방법. KR1017590930000 07.01, 2015.

38. Ling, D. Y.; Ling, X. S., On the distribution of DNA translocation times in solid-state nanopores: an analysis using Schrodinger's first-passage-time theory. *Journal of Physics: Condensed Matter* 2013, *25* (37).

39. Kowalczyk, S. W.; Grosberg, A. Y.; Rabin, Y.; Dekker, C., Modeling the conductance and DNA blockade of solid-state nanopores. *Nanotechnology* 2011, *22* (31), 315101.

40. Lu, B.; Albertorio, F.; Hoogerheide, D. P.; Golovchenko, J. A., Origins and Consequences of Velocity Fluctuations during DNA Passage through a Nanopore. *Biophysical journal* 2011, *101* (1), 70-79.

Chapter 3

Surface Modification of Solid-State Nanopore by Plasma-Polymerized Chemical Vapor Deposition of Poly(ethylene glycol) for Stable Device Operation

- Based on the work by Lee, K. *et al.*, Surface Modification of Solid-State Nanopore by Plasma-Polymerized Chemical Vapor Deposition of Poly(ethylene glycol) for Stable Device Operation. *Nanotechnology*, 2020, accepted.[1]

3.1 Introduction

3.1.1 Non-specific DNA Adsorptions on the Nanopore Membrane during Solid-State Nanopore Experiments

As introduced in the previous chapters, the electrical noise and the detection sensitivity issues of the solid-state nanopore have been actively studied and well understood. However, among the issues in the solid-state nanopore, the device reliability still remains as the most critical problem that needs further intensive research.

Non-specific adsorption of biomolecules onto the nanopore membrane is the major factor that degrades the reliability and the performance of the solid-state nanopore device. Figure 3-1 illustrates the typical situations where the adsorptions adversely affect the detection during the nanopore experiments. Adsorption of DNA near the nanopore surface is reflected in the ionic current trace as a stepwise decrease in the baseline current level and increase in its noise (width of the baseline current band).[2-5] If adsorption is detected, the applied voltage is set to undergo a series of short zaps to a high voltage (~1000 mV) or is released to 0. The voltage manipulations are either to electrically tear off the adsorbed DNA from the surface or to let it naturally be free from the surface during the thermal fluctuation of the molecule.[4] The baseline current level and its noise return to the original level when the adsorbed molecule is cleared away. Nevertheless, the actions are sometimes ineffective; in this case, the nanopore is permanently damaged or clogged by the adsorbed DNA molecules, and the device eventually faces its failure.

In addition, DNA adsorptions on the nanopore surface can degrade the reliability of the nanopore detection as well as the reliability of the device itself. In the case in Figure 3-1(b), DNA translocations could be detected even after a clogging was observed.[5] This is a plausible situation when the adhered DNA molecule only partially block the nanopore so that a sufficient volume in the nanopore is allowed for other free DNA molecules to pass through.

Nevertheless, the attached DNA molecule may interact with the translocating DNA molecule, producing longer-lasting signals than in the free state. In other words, the information of the translocation peak signals can change in the presence of surface-adsorbed DNA, as if the nanopore device was changed.

Another signal change induced by adsorption is a motion of the adhered biomolecule inside the nanopore called vibration.[2] This mode is frequently identifiable especially in protein detections using nanopores. As one end of a biomolecule is anchored on the nanopore surface, another end can freely move and sometimes a molecular fluctuation inside the nanopore can occur (Figure 3-2). The molecular position in the nanopore moves back and forth, so two ionic current levels indicating the situations in Figure 3-2(a) and Figure 3-2(b) are recorded repeatedly. This sign of vibration can be misunderstood as real events especially when the current level difference between the two states is similar to the expected ΔI of the translocation.

In summary, DNA adsorptions on the nanopore surface are of negative influence to the lifetime of the device and the reliability in detection. Consequently, unwanted adherence has been targeted to prevent as much as possible during the biomolecule detections using solid-state nanopores.

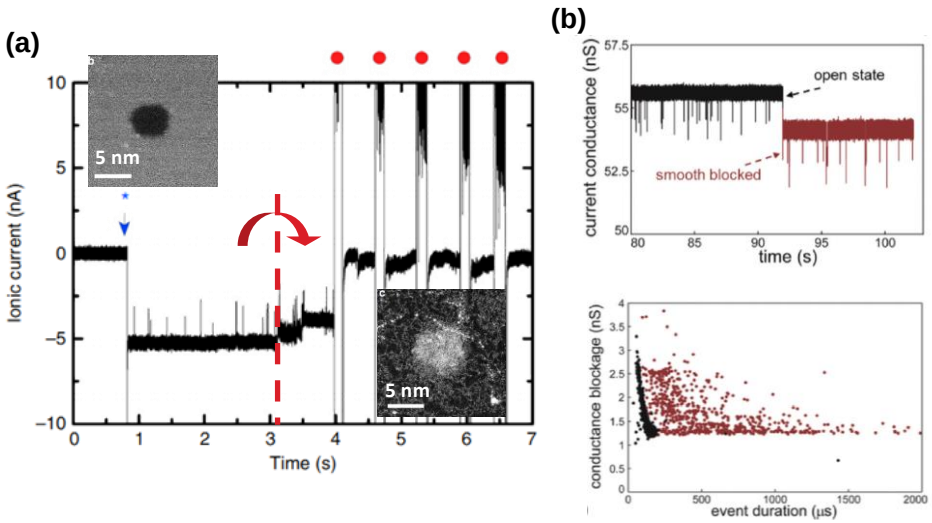

Figure 3−1 Signal changes caused by DNA adsorption during solid−state nanopore experiment. (a) DNA adsorption (red arrow) and voltage manipulations (red dots) to release the adhered molecule. The blue arrow points the time when the voltage (−200 mV) was applied initially. Insets are TEM images of the initial (left, top) and the clogged nanopore (right, bottom). (b) DNA translocation signal distortions in the partly blocked nanopore. Figures were adapted with permission from (a) ref.[4]. Copyright 2013 Springer Nature; (b) ref.[5]. Copyright 2015 Royal Society of Chemistry.

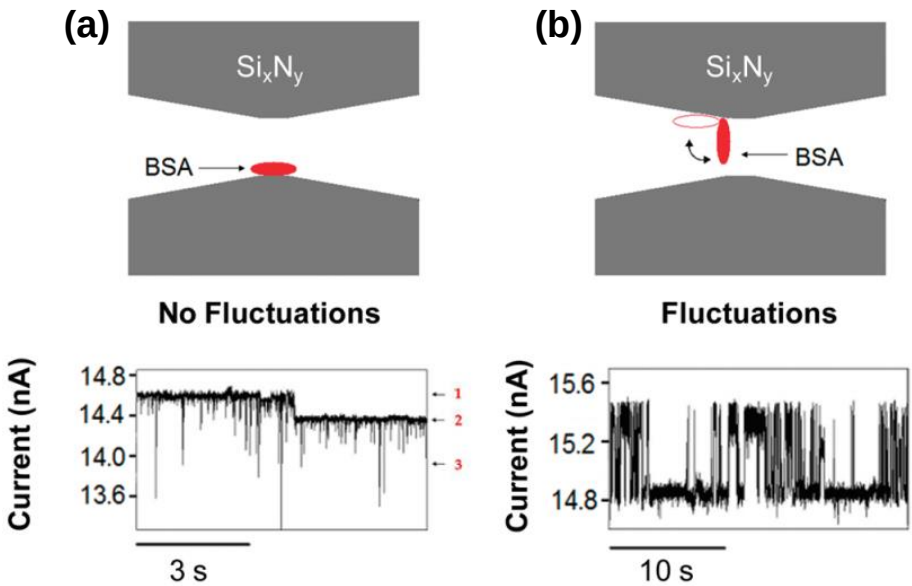

Figure 3-2 Ionic current signals reflecting the nanopore surface adsorptions of proteins. Schematic images (top) and ionic current traces (bottom) of (a) simple or quiet adsorption and (b) fluctuation or vibration of a protein (bovine serum albumin, BSA) molecule inside a nanopore. Figures were reproduced with permission from ref.[2]. Copyright 2010 American Chemical Society.

3.1.2 Previous Research on Preventing DNA Adsorptions on the Solid-State Nanopore Surfaces

The prevention of DNA adsorptions on the solid-state nanopore surfaces has been approached in a molecular and materials aspect. Namely, poly(ethylene glycol) (PEG), a class of molecule renowned for its anti-biofouling property, was coated on the nanopore surface to reduce the chances of DNA adsorption.[4, 6-8] 2 mechanisms have been proposed for the antifouling behavior of PEG: steric hindrance provided by the brushlike conformation of the polymer molecule and blocking of the surface by the hydration layer formed in the polymeric layer.[9] In both ways, biomolecules approaching the surface are physically blocked that they can barely interact with the surface to adhere. In contrast, hydrophobic interaction between the nanopore surface and the hydrophobic functional group in DNA or proteins is suggested as the mechanism of DNA adsorption in nanopore experiments.[2, 3, 10]

There have been several results where the device operation times were prolonged after PEG coating on the nanopore membrane. 2 representative results are summarized in Figure 3-3. Tang *et al.* coated PEG_{200} on a pre-pored nanopore device using the polymer self-assembly method (Figure 3-3(a)).[6] As a result, sticky ssDNA molecules could smoothly translocate through the functionalized nanopore for hours, whereas ssDNA adsorbed onto the uncoated surface only a few 10-seconds after the voltage was applied. Similarly, in Schneider *et al.*, pyrene ethylene glycol was self-assembled on graphene against severe DNA damage on the hydrophobic surface (Figure 3-3(b)).[4] Likewise, stable ssDNA detections were demonstrated using the polymer-coated graphene nanopore, and the cleanness of the functionalized surface after the experiment was imaged using atomic force microscopy (AFM). Following these reports, a few other articles using PEG or related material to promote stable detections and to enhance the device reliability were published.[8, 11]

The effective passivation of the SiN_x or the graphene surface

against biomolecule adsorption was provided by the self-assembly method. Self-assembly is a simple polymer preparation method performed in the liquid phase without heavy instruments required. However, the protocol has inherent limitations such as low scalability, controllability, reproducibility, and efficiency.[6] In addition, the published works mentioned the PEG coating effect on nanopore only by listing the maximum operation times of the polymer functionalized devices. The reports also lack physical or detailed explanations on the anti-biofouling function of the layer compared to the bare SiN_x or graphene surface.

Therefore, in this chapter, the gas-phase deposition of the PEG layer (plasma-polymerization of PEG[12-14]) will be applied instead of the self-assembly method in fabricating the polymer-coated solid-state nanopore device. The replacement was for the enhanced efficiency of fabrication in terms of the processing time and the number of devices that can be operated at once. The antifouling performance of the plasma-polymerized PEG (PP-PEG) compared to the SiN_x surface will be examined with the surface interaction effect on the DNA translocation, from a perspective of electrokinetics in DNA translocations.

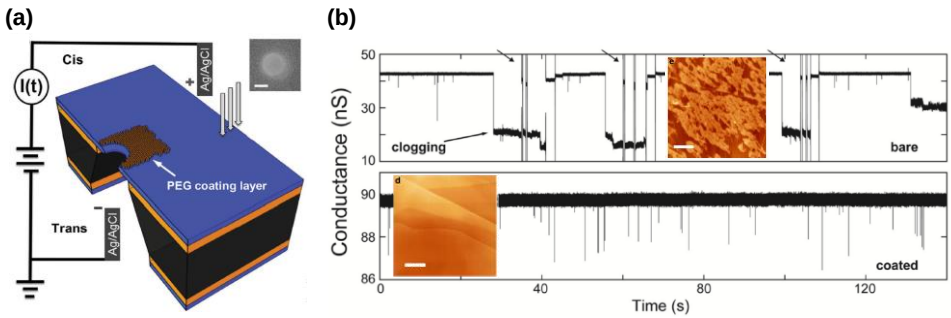

Figure 3-3 Reported PEG coating results on solid-state nanopore. (a) model diagram of PEG-coated solid-state nanopore using the self-assembly method. The nanopore diameter in the inset is 6 nm, and the scale bar denotes 10 nm. (b) ionic current trace during ssDNA detection using the uncoated (top) and the PEG-coated (bottom) nanopore devices. Inserted are the AFM images of the uncoated (top) and the coated (bottom) nanopore surface after ssDNA detection experiment, with the scale bars indicating 200 nm. Figures were reproduced with permission from (a), (b) ref.[6]. Copyright 2014 WILEY-VCH Verlag GmbH & Co. KGaA, Weinheim; inset of (b) ref.[4] Copyright 2013 Springer Nature.

3.2 Fabrication of the PP-PEG Deposited Solid-State Nanopore Device

(PP-PEG deposition conducted by Dr. Jisoo Park and Dr. Tae Geol Lee, Korea Research Institute of Standards and Science (KRISS))

Figure 3-4 illustrates the outline of the PP-PEG deposited nanopore fabrication. First, SiN_x/Si conventional nanopore devices were created using a similar method as in chapter 2. Here, the fabrication started from 100 nm-thick low-stress SiN_x LPCVD, so the SiN_x membrane should be etched down to ~20 nm before PEG deposition. The membrane was etched from the bottom side of the nanopore chip, using the same RIE protocol in section 2.3.1. This was to minimize the possible damage caused by the plasma on the membrane surface on which PP-PEG would be deposited.

PP-PEG deposition followed the reported protocol using the facilities setup at KRISS.[12-14] The deposition conditions were 100 mTorr Ar carrier gas pressure with vaporized $PEG_{200}(l)$ (canister temperature 105°C, line temperature 140°C), 2 W, 20 min. To facilitate the deposition, the top SiN_x surface of the SiN_x/Si device was hydrophilized under 30 mTorr of O_2, 30 W, and for 10 min before the main process. In this process, the plasma-polymerized film could be deposited on the nanopore surface under a weak power of 2 W.[12, 15] The weak plasma power was suitable for preparing a PP-PEG film with high chemical similarity to pure PEG_{1000} when examined using x-ray photoelectron spectroscopy (XPS). In addition, the anti-adhesiveness of the PP-PEG film has been confirmed in blood plasma and tissue compatibility tests.[12]

After the PP-PEG deposition, a nanopore was perforated using TEM, which penetrated the PP-PEG film and the SiN_x film simultaneously. The PP-PEG layer was unable to be used without the supporting layer because of its weak mechanical stability. Nevertheless, this bilayer nanopore structure was suitable for the direct comparison of the surface effect on DNA adsorptions, from that the surfaces shared the nanopore of the same dimension.

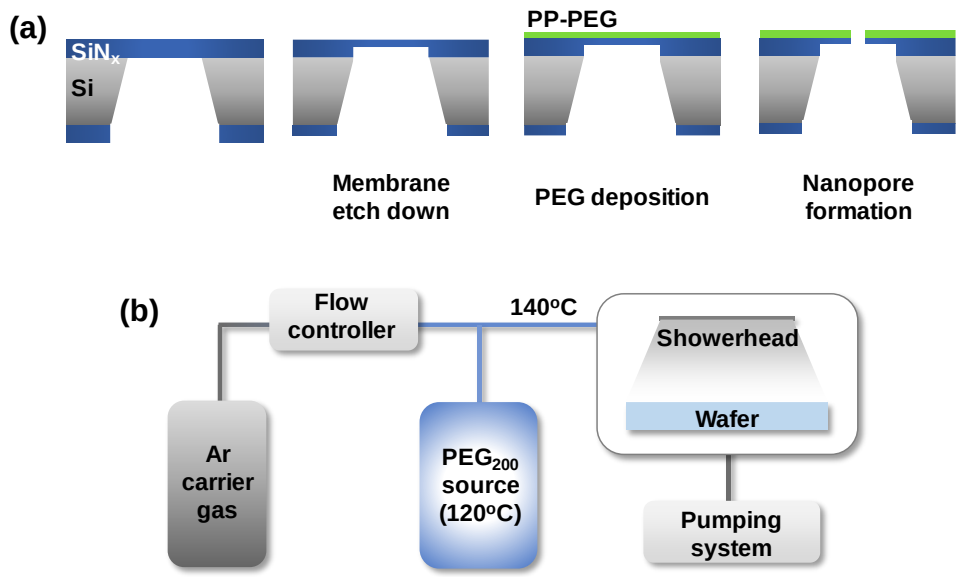

Figure 3-4 Fabrication of the PP-PEG deposited solid-state nanopore. (a) the fabrication process of the PP-PEG/SiN_x nanopore device. The image is not in scale. (b) PP-PEG deposition system schematics. (a) was reproduced with permission from ref.[1]. Copyright 2020 IOP Publishing.

3.3 Experimental Details

3.3.1 Experimental Details

The PP-PEG/SiN_x nanopore fabrication was conducted as explained in section 3.2 and 2.3. The low-stress SiN_x film deposition method and SiN_x partial etch condition to control the membrane thickness in chapter 2 were also used here. The PP-PEG deposition was performed in the custom-built plasma chemical vapor deposition facility setup and KRISS. The nanopores of 5-8.5 mn diameter were fabricated using JEOL-2010F TEM.

In the optical observation, Olympus® BX60M microscope and Nikon® Eclipse 90i fluorescence microscope were used. The fluorescence detection was performed to optically compare the antifouling property of the PP-PEG surface and the bare SiN_x surface. In this experiment, YOYO-dye tagged λ-DNA (20 μl, 500 ng/μl) was dropped on each surface and incubated for 10 min to allow enough time to adhere to the surface. After 10 min, a piece of cover glass was placed on the solution and the fluorescence signals were observed. The contact angle was measured using a custom contact angle imaging system.

The nanopore characterization and experiments with DNA were performed in the same setup as in section 2.3. First, to electrically characterize the nanopore devices, the PP-PEG/SiN_x nanopore and SiN_x nanopore were each assembled with the custom Teflon® flow cell and connected to the current amplifier. 1 M KCl solution buffered with TE buffer at pH 8.0 was filled in the flow cells to assess the electrical noise and the ionic conductance of each nanopore. For the DNA adsorption test and translocation experiment, 1 nM of 1 kbp dsDNA diluted in the buffered KCl solution was injected in both chambers. Here, 7 PP-PEG/SiN_x nanopores of 5-8.5 nm diameter were used. The detailed experimental sequence of the antifouling property evaluation during the nanopore experiment will be explained in the next section.

3.3.2 Experimental Sequence to Evaluate the Surface Reliabilities of the Nanopore Membrane Surfaces against DNA Adsorption

The model experimental sequence of DNA adsorption test is presented in Figure 3-5. The key feature is the control of the DNA translocation direction by switching the sign of the applied voltage without changing the setup or the nanopore device. For instance, in the inset of Figure 3-5, a DNA molecule would translocate the nanopore from the PP-PEG side under the positive voltage, when another molecule would start the translocation from the SiN_x side under the negative voltage.

In this sequence, DNA molecules in either chamber were driven to translocate the nanopore until adsorption occurred (labeled as '-500 mV' and '500 mV' in Figure 3-5). After a current drop lasting longer than one second (red asterisks in Figure 3-5), which was recognized as adsorption in this work, the applied voltage was set as 0 for ~20 s to release the adsorbed DNA to the free space (labeled as '0 mV' in Figure 3-5). Then, the voltage of the same magnitude but the opposite sign was applied to pull the DNA from the opposite side. This was repeated several times until the adsorption was too strong that setting the voltage at 0 was ineffective in clearing the molecule off the surface. The time criterion of adsorption, 1 s, was determined based on the translocation results of 1 kbp dsDNA obtained in chapter 2; all DNA translocation times were shorter than 1 s. Therefore, it is reasonable to regard a current drop lasting longer than 1 s would be less likely to be spontaneously recovered to the baseline current. Although only one cycle beginning from the SiN_x side was illustrated in the figure, the cycles also were performed the other way around, beginning from applying the positive voltage to draw DNA from the PP-PEG side first. ±150 mV, ±300 mV, and ±500 mV were applied to compare the antifouling properties of the PP-PEG and the SiN_x surface under different bias voltages.

There were 3 terms that could be analyzed from the experiment described above. First, times to adsorption on the PP-PEG surface (t_{PP-PEG}) or on the SiN_x surface (t_{SiN}) were the time

allowed in each surface for smooth DNA translocations before adsorption occurred (blue double-headed arrows in Figure 3-5). Therefore, the time to adsorption was an experimental meter of the nanopore surface stability against the unwanted DNA adsorptions: the longer the time to adsorption, the more stable and DNA-resistant the surface would be. As the surface adsorptions are based on the molecular interaction between the surface and DNA, the time to adsorption also would be a statistical term. Therefore, the statistical time to adsorption was a more suitable representation of the antifouling performance of a nanopore surface than simply presenting the longest operation time of the device without adsorption. Although it was a less representative term, the operation time before the failure of each surface was also presented in this chapter for practical comparison. This was a measure of the total time allowed until the surface was severely damaged by the biomolecule so that the reliability of the device itself or of the detected signal could no longer be guaranteed. Thirdly, DNA translocation signals during the adsorption test were collected to check if the different DNA-surface interactions induced any change in the signal (ΔG, t_d) and DNA translocation behaviors.

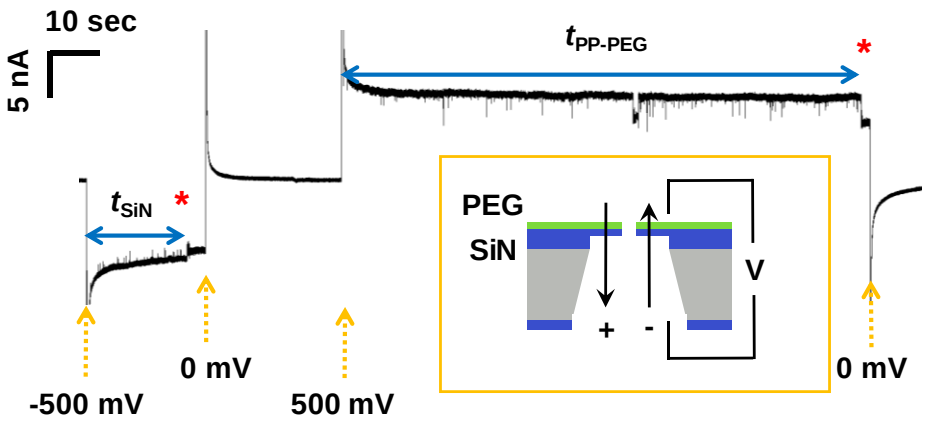

Figure 3-5 Model experimental sequence for evaluating the anti-adsorption property of the surfaces during the nanopore experiment. The inset informs the direction of DNA translocation by the sign of the applied voltage. The labels are explained in the text. Figure was adapted with permission from ref.[1]. Copyright 2020 IOP Publishing.

3.4 Result and Discussion

3.4.1 Optical Characteristics of the Deposited PP-PEG Surface

The optical observations of the PP-PEG surface deposited compared to the bare SiN_x surface are displayed in Figure 3-6. From the optical microscope imaging, the PP-PEG and the SiN_x surfaces were indistinguishable to each other due to the high transparency of PEG (Figure 3-6(a)).[16] Therefore, additional examinations, contact angle measurement and fluorescence imaging of the adsorbed DNA, were conducted.

From the hydrophilic nature of PP-PEG, the surface contact angle of a water droplet would decrease after the deposition. The experimental result corresponded to the expectation, where the average contact angles were 45° and 15° on the PP-PEG surface and on the SiN_x surface, respectively (Figure 3-6(b)). The purpose of the fluorescence imaging was to visually check if the nanopore membrane surface was successfully passivated by the antifouling material. As a result, the fluorescent signals from the adhered λ-DNA were barely noticeable on the PP-PEG surface, whereas the bright signals were detected all over the SiN_x surface indicating the severe DNA adsorptions on the uncoated surface.

In conclusion, from the contact angle measurement and the fluorescence microscope imaging, the successful deposition of a hydrophilic and antifouling layer was identified

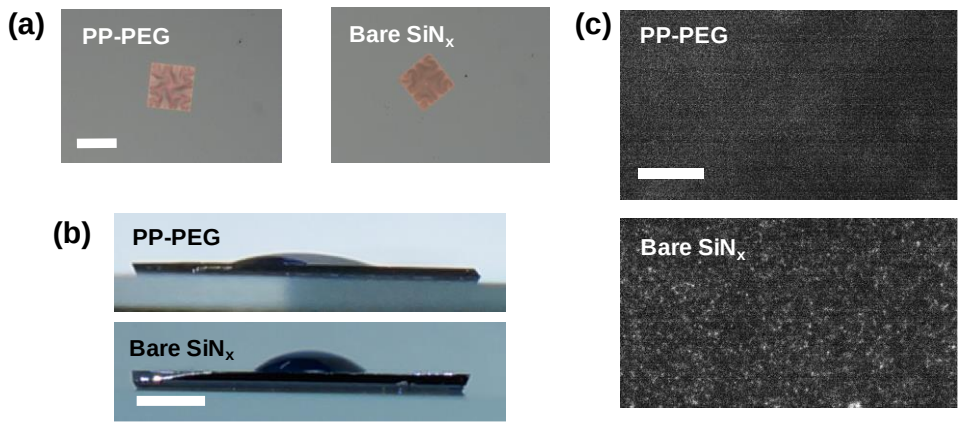

Figure 3-6 Optical characterization of the PP-PEG deposited nanopore surface. (a) optical micrograph of the PP-PEG deposited membrane (left) and the bare SiN_x (right), with the scale bar indicating 50 μm. (b) contact angle measurement of the PP-PEG deposited surface (top) and the bare SiNx surface (bottom). A 200 μm scale bar is marked in the figure. (c) fluorescence microscopy image after 10-min incubation of YOYO-dye labeled λ-DNA on the deposited PP-PEG (top) and the bare SiN_x (bottom) surface. The scale bar indicates 20 μm. Figures were adapted with permission from ref.[1]. Copyright 2020 IOP Publishing.

3.4.2 Electrical Characteristics of the PP-PEG/SiN_x Nanopore Device

Before moving to the main analysis in this chapter, the electrical characteristics of the PP-PEG/SiN_x nanopore were briefly investigated. The results are presented in Figure 3-7.

In the $I-V$ curve measured in 1 M KCl of pH 8.0, the PP-PEG/SiN_x nanopore exhibited a constant ionic conductance over the voltage, as in typical nanopores (Figure 3-7(a)). Using the measured conductance value and the known nanopore size from the TEM image, the thickness of the PP-PEG/SiN_x nanopore could be computed. From G=24.5 nS and d=8.5 nm, the length of the nanopore in Equation 1.1 was 27.9 nm. Therefore, the thickness of the PP-PEG layer on the 20 nm-thick SiN_x was 7.9 nm, which corresponded to the measured value using the cross-section SEM image.[12]

The electrical noise PSD curves of the PP-PEG/SiN_x nanopore at 0 mV and 100 mV were presented in Figure 3-7(b), with the curves measured using the conventional SiN_x nanopore device with a similar nanopore diameter (9 nm). The noise power levels and the outline of the curves were in correspondence with the general results in the Si-substrate nanopores.[17, 18] Namely, the flicker noise was distinguished below 100 Hz and the dielectric noise acted as the dominant noise source above 100 Hz.

A notable feature of the noise characteristic was the increased flicker noise in the PP-PEG deposited nanopore than in the conventional nanopore. For the PSD curves at 100 mV, ≤100 Hz frequency region is zoomed-in Figure 3-7(c) for a clearer comparison. To quantitatively figure out the degree of increase, the PSD curves in the low frequency range were fitted to the flicker noise power equation (Equation 1-4). As a result, A_{PP-PEG} was 6.3 times larger than A_{SiNx}. The increase in the material parameter implied that the polymeric layer deposition adversely affected the electrical noise property of the nanopore device.

The large flicker noise observed in the PP-PEG/SiN_x nanopore can be attributed to the brushlike molecular conformation of PEG. With one end of the polymer chain anchored to the PP-

PEG/SiN_x interface, another end would be continuously fluctuating in solution. Particularly, the molecules near the nanopore are possible sources of the inconsistency in the ionic current, which would be directly related to the flicker noise of the nanopore. The increase in the flicker noise was a frequently observed trend also in other polymer functionalized nanopores.[19-22] Nevertheless, the influence range of the flicker noise was only limited to frequencies below 100 Hz, which was only a small fraction of the total frequency domain of <10 kHz. Therefore, in spite of the raised flicker noise, the rms noise level of the PP-PEG/SiN_x nanopore was only slightly larger than that of the SiN_x nanopore, 58.6 pA and 54.2 pA, respectively.

In conclusion, the PP-PEG/SiN_x nanopore was successfully characterized as in the conventional SiN_x nanopore. Although the flicker noise was increased after the PP-PEG layer deposition due to the molecular nature of the polymer, the total rms noise was minimally affected. Accordingly, the antifouling properties of the PP-PEG surface could be further evaluated without a substantial reduction in the detection sensitivity.

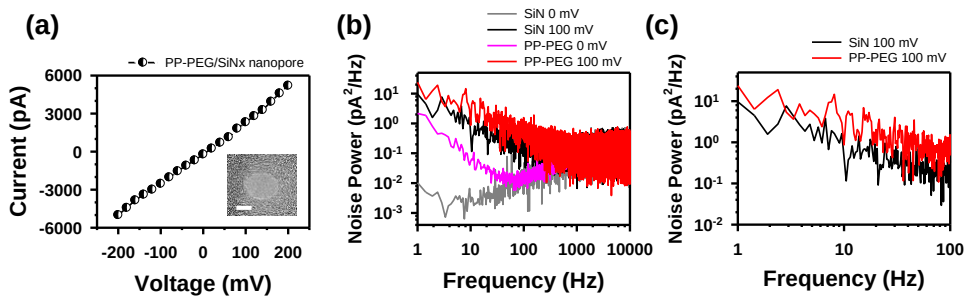

Figure 3-7 Electrical characterization of the PP-PEG deposited nanopore device. (a) *I*-*V* curve of the 8.5 nm-diameter PP-PEG/SiN_x nanopore in the inset (scale bar: 5 nm). (b) noise PSD curves of the PP-PEG/SiN_x nanopore (0 mV: pink, 100 mV: red) and the bare SiN_x nanopore (0 mV: gray, 100mV: black). (c) a close-up view of the 100 mV noise curves of the PP-PEG/SiN_x nanopore (red) and the bare SiN_x nanopore (black) in a 1-100 Hz frequency range. Figures (a)-(c) were reproduced with permission from ref.[1]. Copyright 2020 IOP Publishing.

3.4.3 Reliability against DNA Adsorptions on the PP-PEG and SiN_x Surfaces

Using the sequence explained in section 3.3.2 and Figure 3-5, the times to adsorption to the PP-PEG surface and the SiN_x surface were collected under 150, 300, and 500 mV. The result is summarized in Figure 3-8, where the numbers of data n = 8, 23, 32 (150, 300, 500 mV) for the PP-PEG and 8, 14, 17 (150, 300, 500 mV) for the SiN_x.

As expected from the good antifouling performance of PP-PEG (Figure 3-6(c)), the time to adsorption on the polymeric surface was longer than that on the bare SiN_x surface at all voltages. In detail, the mean time allowed for smooth translocations were extended by 56.9% (150 mV), 117% (300 mV), and 24.8% (500 mV) on the deposited film.

Apparently, the PP-PEG surface was unable to perfectly prevent DNA adsorptions during nanopore experiment. This was against the observation in Figure 3-6(c), where the fluorescence signal was absent on the PP-PEG surface indicating the surface was completely passivated from any DNA adsorptions. The disagreement would have been originated from the device structure and high sensitivity of the nanopore detection. The fabrication strategy in this work inevitably exposed the SiN_x surface in the pore interior, which can provide possible adsorption sites by attractively interacting with the translocating DNA molecules. In addition, the nanopore detection has single-molecular sensitivity, thus more DNA adsorptions could be recognized by the nanopore than by the optical microscope.

Additionally, in Figure 3-8, the relationship between the time to adsorption and the applied voltage was clear: shorter time is allowed for smooth DNA translocation under higher applied voltages. The applied voltage can affect the chance of DNA adsorption by electrical drawing of DNA near the nanopore region. The drawing situation can be understood physically, using the DNA capture theory in the solid-state nanopore. The DNA capture situation is graphically presented in Figure 3-9, with the electrical driving force and the surface interaction forces are marked as arrows. The specific

relationship between the capture rate and the applied voltage is shown in Equation 3−1:

$$R_c = c_{DNA} 2\pi D r^* = c_{DNA} \frac{\pi d^2 \mu_{DNA}}{4l} V \quad (3-1)$$

where R_c is the capture rate, c_{DNA} is the bulk DNA concentration, D is the diffusivity of DNA, r^* is the radius of the capture region, μ_{DNA} is the electrophoretic mobility of DNA, and V is the applied voltage.[23, 24] The derivation of R_c was based on an assumption that a DNA molecule cannot escape from the nanopore if it reaches the point where the electrical driving energy becomes equal to the thermal energy. The capture region is the hemisphere where the electrical energy is higher than the thermal energy of DNA to escape to the free space.[23, 24] Experimentally, the times to adsorption in both the PP−PEG and the SiN_x surface were proportional to $1/V$ (Figure 3−8), corresponding to the relationship in Equation 3−1. Therefore, the experimental result suggested that the voltage−driven capture directly influenced the DNA adsorptions.

Meanwhile, the DNA capture rate, or interaction frequency of DNA and surface, should be the identical at the same voltage regardless of the surface according to Equation 3−1. The experimental difference in the time to adsorption on the PP−PEG and the SiN_x surface should be attributed to the different surface interaction modes. The repulsive nature of the PP−PEG surface would have discouraged the DNA adsorptions, whereas the attractive SiN_x surface would have been favorable for such changes. Quantitatively, according to the coefficients of the $1/V$ fittings, the PP−PEG surface exhibited 63% enhanced antifouling property than the bare SiN_x surface.

In conclusion, the anti−adsorption performances of the PP−PEG deposited and the bare SiN_x surfaces were compared by the time to adsorption. As a result, the surface stability against the unwanted DNA adsorptions was enhanced on the modified surface than on the bare surface at all voltage conditions. The voltage dependence of the

time to adsorption was analogous to that of the DNA capture rate by nanopore, suggesting that the electrical drawing of DNA was mainly responsible for the adsorption probabilities. The DNA–surface interaction modes also contributed to the time to adsorptions, resulting in 63% improvement in antifouling property on the PP–PEG surface. Before closing this discussion, the device operation time until failure should be mentioned for each membrane surface. The PP–PEG surface could be used in the experiment for 48 min on average before severe damage to the surface was observed, with the maximum operation time of 110 min. On the other hand, the SiN_x surface suffered from severe adsorptions after 11 min on average, with the maximum survival time of 14 min.

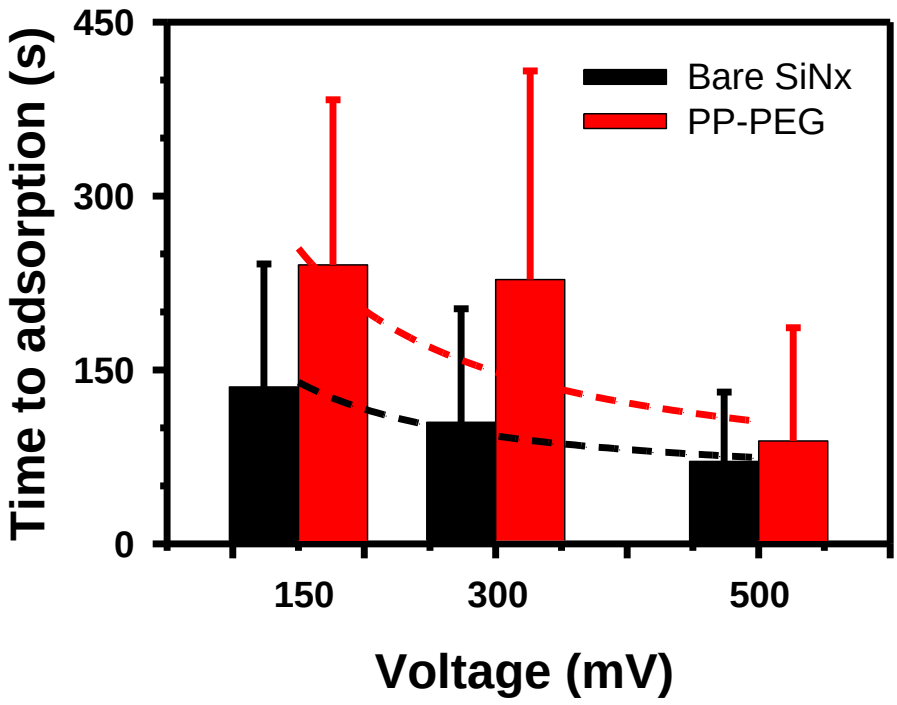

Figure 3-8 Anti-adsorption characterization of the surface during nanopore experiment. Time to adsorption plots as a function of applied voltage are exhibited for bare SiN_x (black bars) and the PP-PEG deposited (red bars) surfaces. Dashed lines are the fitted curves of the PP-PEG data (red line) and the SiN_x data (black line), each proportional to $1/V$. Figure was adapted with permission from ref.[1]. Copyright 2020 IOP Publishing.

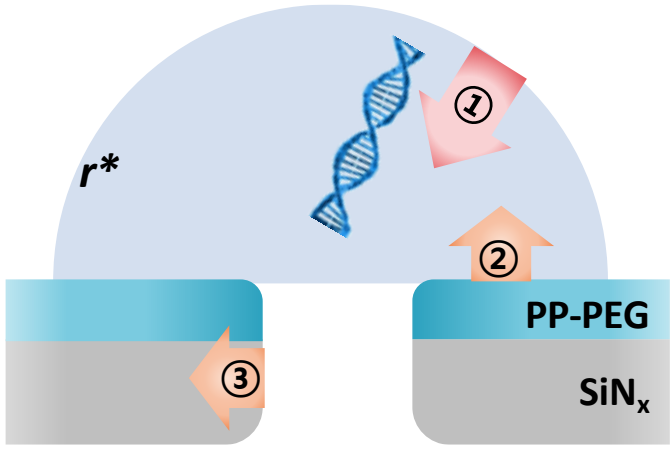

Figure 3-9 Microscopic view on the DNA adsorption and capture situations. The numbered arrows indicate ① electrophoretic force drawing DNA near the nanopore, ② repulsion force between PP-PEG and DNA, and ③ attraction force between PP-PEG and SiN_x. The blue-shaded region and r^* each represent the capture region and its radius.

3.4.4 Surface Interaction Effect on the DNA Translocation Behaviors

Extending the discussion on the DNA–surface interaction further, signals of DNA translocations initiated from the PP–PEG side or the SiN_x side were compared. The DNA translocation results obtained at 150, 300, and 500 mV from the two surfaces are displayed in Figure 3–10. The number of data points n=658 (150 mV, PP–PEG), 991 (150 mV, SiN_x), 1894 (300 mV, PP–PEG), 360 (300 mV, SiN_x), 2331 (500 mV, PP–PEG), and 969 (500 mV, SiN_x). In general, low ΔG and small t_d are visually noticed in the events initiated on the PP–PEG side than those from the bare SiN_x(Figure 3–10(a)). The detailed analysis of the ΔG and t_d differences is discussed below according to the translocation event information, focusing on the repulsive (PP–PEG) and the attractive (SiN_x) modes of the DNA–surface interaction.

As in the previous chapter, the ΔG data were reconstructed as the histograms in Figure 3–10(b). The most distinguishable feature in all cases was the main ΔG distribution centered at 2–3 nS, corresponding to the geometrically calculated ΔG of DNA ~2.5 nS.[25] In the translocations starting from the SiN_x side, events with ΔG at 4–6 nS were also found in a noticeable portion. Particularly at 300 mV, the large events even formed an additional Gaussian distribution. As the translocation signal magnitude reflects the occupied volume of the translocating molecule inside the nanopore, large signals represent the passage of DNA in its folded conformation.[26] Therefore, the high portion of deep signals suggested that DNA would have been more likely to pass through the nanopore in a folded form when it approached from the SiN_x side, whereas the PP–PEG side was more favorable for fully stretched translocations. This is a reasonable explanation considering the interaction modes of the PP–PEG and DNA as the repulsion would have made the DNA difficult to enter the nanopore in the folded conformations. However, at 500 mV, the 2 histograms were less distinguishable from each other because the strong driving force unthreaded the translocating DNA regardless of the surface interaction.

Figure 3-10(c) is the summary of the t_d of the translocations starting from the PP-PEG or the SiN_x surface. Similar to the discussion in chapter 2, it was difficult to compare t_d on the 2 surfaces directly from the histogram. The normalized histograms were fitted to Equation 2-19 to figure out the translocation velocity at each condition. v_{PEG}/v_{SiN} was calculated to evaluate the relative velocity of the DNA translocations, where v_{PEG} and v_{SiN} represent the fitted velocities measured at each surface. As a result, the ratio v_{PEG}/v_{SiN} at 150, 300, and 500 mV were 1.92, 3.39, and 3.89, respectively. The $v_{PEG}/v_{SiN} > 1$ suggested that the DNA translocations started from the PP-PEG surface were faster than those from the SiN_x surface under all conditions. This could be also understood considering the surface interaction with DNA, in that DNA-attractive nature of the surface has been reported to reduce the translocation time.[10, 27] Reversely, the repulsive PP-PEG surface would induce faster translocations as observed in the experiment.

In summary, the different surface interaction modes, repulsion on the PP-PEG and attraction on the SiN_x, were reflected in the DNA translocation behaviors as well as the adsorption resistance. The DNA-repulsive nature of the polymeric film induced smaller signal magnitude and faster DNA translocations than the bare SiN_x surface and the observed changes corresponded to the results from the previous works.

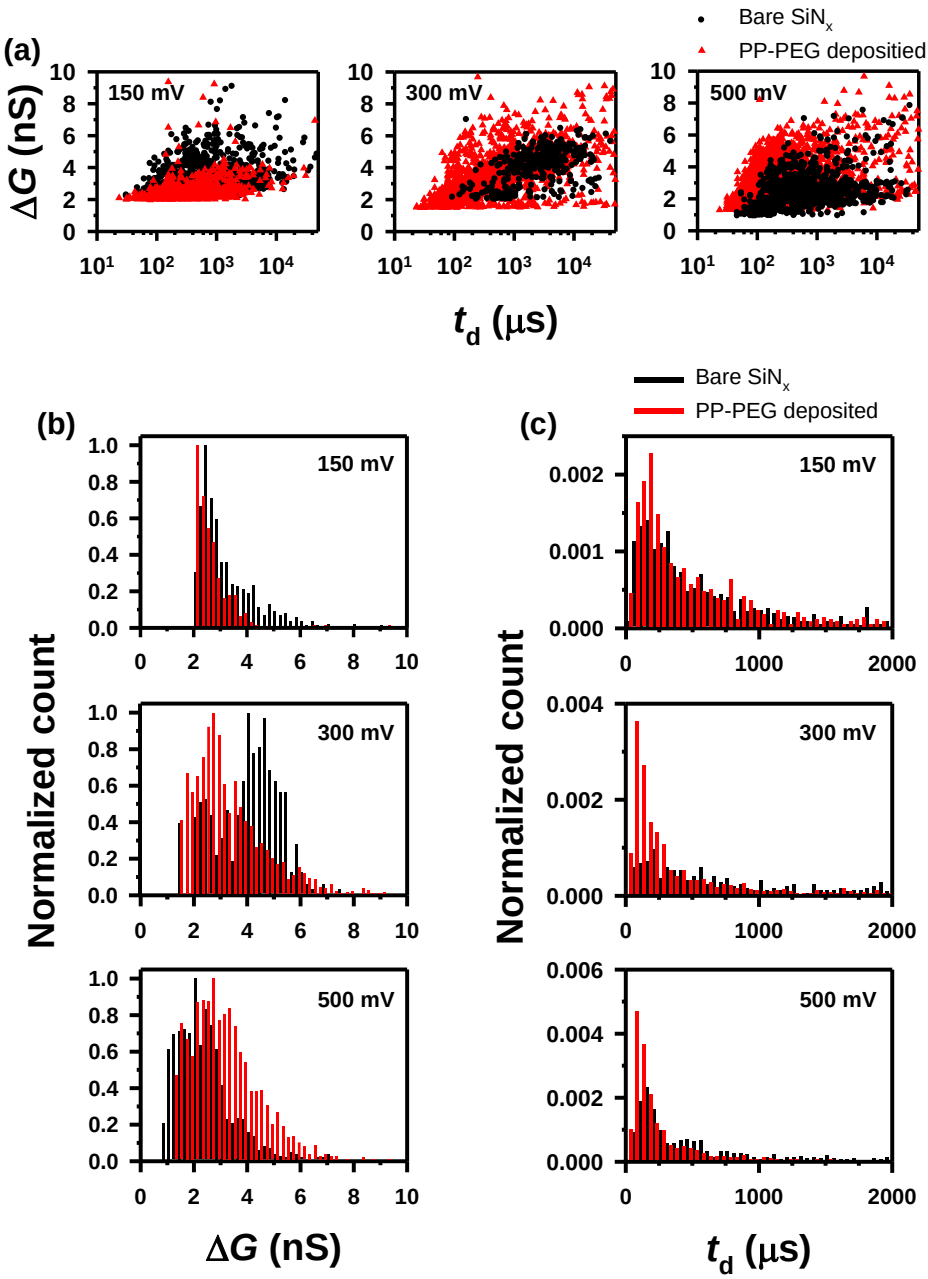
(a)
Bare SiNx
PP-PEG deposited
150 mV
300 mV
500 mV
ΔG (nS)
td (μs)
(b)
(c)
Normalized count
ΔG (nS)
td (μs)

Figure 3-10 DNA translocation data in the PP-PEG/SiN_x nanopore. (a) $\Delta G - t_d$ scatter plots of DNA translocation signals initiated from the bare SiN_x side (black dots) and the PP-PEG side (red triangles) detected at 150 mV (left), 300 mV (middle), and 500 mV (right). (b)-(c) (b) ΔG and (c) t_d histograms of the events in (a) under 150 mV (top), 300 mV (middle), and 500 mV (bottom). Black bars and red bars represent the translocation data from the SiN_x surface and the PP-PEG surface, respectively. Figures were adapted with permission from ref.[1]. Copyright 2020 IOP Publishing.

3.5 Conclusion

In this chapter, the plasma-polymerized poly(ethylene glycol) film was deposited on the solid-state nanopore to enhance the device reliability against DNA surface adsorptions. The polymeric material has been frequently used in previous efforts to prevent the surface adsorptions, but only by the liquid-phase self-assembly preparation method. Here, the polymer film was prepared using the gas-phase deposition technique, which was advantageous over the self-assembly method in terms of reproducibility, controllability, and process efficiency. The successful deposition of hydrophilic and antifouling layer on SiN_x/Si nanopore device was confirmed from the contact angle measurement and the fluorescence observation of the surface adhered DNA.

To assess the anti-adsorption property of the PP-PEG surface, time to adsorption concept was introduced, which explained the time allowed for smooth DNA translocations until mild adsorption occurred. The PP-PEG surface showed 1.25-2 times longer time to adsorption compared to SiN_x, proving its enhanced surface stability over the untreated surface. From the physical analysis of the nanopore capture theory and the force calculation, the voltage-driven DNA drawing dominantly affected to the surface adsorption probability, while the repulsive nature of PP-PEG still provided more chances of translocation without adhering to the surface. The DNA-surface interaction also affected to the DNA translocation behaviors, where the repulsive PP-PEG surface promoted more stretched and faster DNA translocations than the attractive SiN_x surface.

The significance of this work was that the realistic meter of surface adsorption property on the nanopore membrane (time to adsorption) was suggested with the new fabrication method of the polymer functionalized nanopores (plasma polymerization). On the other hand, the previous works only presented the maximum time until the first adsorption occurred as the antifouling performance of the functionalized membrane. In the fabrication aspect, the PP-PEG

deposition was particularly beneficial in enhancing the fabrication throughput. Since the feasibility of the PP-PEG film as an antifouling coating was confirmed in this work, the deposited film quality and property would be worth and necessary to be fine-tuned for better electrical noise and for even more enhanced anti-adsorption properties.

References

1. Lee, K.; Park, J.; Kang, J.; Lee, T. G.; Kim, H.-M.; Kim, K.-B., Surface Modification of Solid-State Nanopore by Plasma-Polymerized Chemical Vapor Deposition of Poly(ethylene glycol) for Stable Device Operation. *Nanotechnology* 2020, *Accepted*.

2. Niedzwiecki, D. J.; Grazul, J.; Movileanu, L., Single-Molecule Observation of Protein Adsorption onto an Inorganic Surface. *Journal of the American Chemical Society* 2010, *132* (31), 10816-10822.

3. Niedzwiecki, D. J.; Movileanu, L., Monitoring Protein Adsorption with Solid-state Nanopores. *Journal of Visualized Experiments* 2011, (58), e3560.

4. Schneider, G. g. F.; Xu, Q.; Hage, S.; Luik, S.; Spoor, J. N. H.; Malladi, S.; Zandbergen, H.; Dekker, C., Tailoring the hydrophobicity of graphene for its use as nanopores for DNA translocation. *Nature Communications* 2013, *4*, 2619.

5. Liang, Z.; Tang, Z.; Li, J.; Hu, R.; Yu, D.; Zhao, Q., Interaction prolongated DNA translocation through solid-state nanopores. *Nanoscale* 2015, *7* (24), 10752-10759.

6. Tang, Z.; Lu, B.; Zhao, Q.; Wang, J.; Luo, K.; Yu, D., Surface modification of solid-state nanopores for sticky-free translocation of single-stranded DNA. *Small* 2014, *10* (21), 4332-4339.

7. Giamblanco, N.; Coglitore, D.; Janot, J.-M.; Coulon, P. E.; Charlot, B.; Balme, S., Detection of protein aggregate morphology through single antifouling nanopore. *Sensors and Actuators B: Chemical* 2018, *260* (1), 736-745.

8. Roman, J.; Jarroux, N.; Patriarche, G.; Français, O.; Pelta, J.; Le Pioufle, B.; Bacri, L., Functionalized Solid-State Nanopore Integrated in a Reusable Microfluidic Device for a Better Stability and Nanoparticle Detection. *ACS Applied Materials & Interfaces* 2017, *9* (48), 41634-41640.

9. Zhang, H.; Chiao, M., Anti-fouling Coatings of Poly(dimethylsiloxane) Devices for Biological and Biomedical Applications. *Journal of Medical and Biological Engineering* 2015, *35*

(2), 143-155.

10. Banerjee, S.; Wilson, J.; Shim, J.; Shankla, M.; Corbin, E. A.; Aksimentiev, A.; Bashir, R., Slowing DNA Transport Using Graphene-DNA Interactions. *Advanced Functional Materials* 2015, *25* (6), 936-946.

11. Emilsson, G.; Sakiyama, Y.; Malekian, B.; Xiong, K.; Adali-Kaya, Z.; Lim, R. Y. H.; Dahlin, A. B., Gating Protein Transport in Solid State Nanopores by Single Molecule Recognition. *ACS Central Science* 2018, *4* (8), 1007-1014.

12. Choi, C., *et al.*, Fabrication and Characterization of Plasma-Polymerized Poly(ethylene glycol) Film with Superior Biocompatibility. *ACS Applied Materials & Interfaces* 2013, *5* (3), 697-702.

13. Choi, C.; Choi, K. O.; Jung, D.; Moon, D. W.; Lee, T. G., Surface characterization of plasma-polymerized polyethylene glycol thin film modified by plasma treatment. *Surface and Interface Analysis* 2013, *45* (1), 220-224.

14. Park, J.; Baik Kim, G.; Lippitz, A.; Kim, Y. M.; Jung, D.; Unger, W. E. S.; Kim, Y.-P.; Lee, T. G., Plasma-polymerized antifouling biochips for label-free measurement of protease activity in cell culture media. *Sensors and Actuators B: Chemical* 2019, *281* (1), 527-534.

15. Sakthi Kumar, D.; Fujioka, M.; Asano, K.; Shoji, A.; Jayakrishnan, A.; Yoshida, Y. J. J. o. M. S. M. i. M., Surface modification of poly(ethylene terephthalate) by plasma polymerization of poly(ethylene glycol). *Journal of Materials Science: Materials in Medicine* 2007, *18* (9), 1831-1835.

16. Gaharwar, A. K.; Rivera, C. P.; Wu, C.-J.; Schmidt, G., Transparent, elastomeric and tough hydrogels from poly(ethylene glycol) and silicate nanoparticles. *Acta Biomaterialia* 2011, *7* (12), 4139-4148.

17. Lee, K.; Park, K. B.; Kim, H. J.; Yu, J. S.; Chae, H.; Kim, H. M.; Kim, K. B., Recent Progress in Solid-State Nanopores. *Advanced Materials* 2018, *30* (42), 1704680.

18. Lee, K.; Lee, H.; Lee, S.-H.; Kim, H.-M.; Kim, K.-B.; Kim, S. J., Enhancing the sensitivity of DNA detection by structurally

modified solid-state nanopore. *Nanoscale* 2017, *9* (45), 18012-18021.

19. Anderson, B. N.; Muthukumar, M.; Meller, A., pH Tuning of DNA Translocation Time through Organically Functionalized Nanopores. *ACS Nano* 2013, *7* (2), 1408-1414.

20. Kowalczyk, S. W.; Kapinos, L.; Blosser, T. R.; Magalhaes, T.; van Nies, P.; LimRoderick, Y. H.; Dekker, C., Single-molecule transport across an individual biomimetic nuclear pore complex. *Nat. Nanotechnol.* 2011, *6* (7), 433-438.

21. Liebes-Peer, Y.; Rapaport, H.; Ashkenasy, N., Amplification of Single Molecule Translocation Signal Using β-Strand Peptide Functionalized Nanopores. *ACS Nano* 2014, *8* (7), 6822-6832.

22. Yusko, E. C.; Johnson, J. M.; Majd, S.; Prangkio, P.; Rollings, R. C.; Li, J.; Yang, J.; Mayer, M., Controlling protein translocation through nanopores with bio-inspired fluid walls. *Nat. Nanotechnol.* 2011, *6* (4), 253-260.

23. Wanunu, M.; Morrison, W.; Rabin, Y.; Grosberg, A. Y.; Meller, A., Electrostatic focusing of unlabelled DNA into nanoscale pores using a salt gradient. *Nat. Nanotechnol.* 2010, *5* (2), 160-165.

24. Grosberg, A. Y.; Rabin, Y., DNA capture into a nanopore: Interplay of diffusion and electrohydrodynamics. *J. Chem. Phys.* 2010, *133* (16), 165102.

25. Kowalczyk, S. W.; Grosberg, A. Y.; Rabin, Y.; Dekker, C., Modeling the conductance and DNA blockade of solid-state nanopores. *Nanotechnology* 2011, *22* (31), 315101.

26. Chen, P.; Gu, J.; Brandin, E.; Kim, Y.-R.; Wang, Q.; Branton, D., Probing Single DNA Molecule Transport Using Fabricated Nanopores. *Nano Letters* 2004, *4* (11), 2293-2298.

27. Larkin, J.; Henley, R.; Bell, D. C.; Cohen-Karni, T.; Rosenstein, J. K.; Wanunu, M., Slow DNA transport through nanopores in hafnium oxide membranes. *ACS Nano* 2013, *7* (11), 10121-8.

Chapter 4

Development and Clinical Application of Electrophoretic Nucleic Acid Preparation System using Nanofilter Membrane Device

– Based on the publication Lee, K. *et al.*, Direct Electrophoretic microRNA Preparation from Clinical Samples using Nanofilter Membrane. *Nano Convergence* 2020, accepted.[1]

4.1 Introduction

4.1.1 Multi-Nanopore Devices and Applications

As the improvements of the solid-state nanopore performances were achieved (*i.e.* low electrical noise, high sensitivity, and enhanced device reliability), the interest in the solid-state nanopore research greatly shifted to its applications. Detection of various biomolecules including proteins, short peptides, DNA-protein complexes, and protein-protein complexes using nanopore is a major part of the application.[2] With the wide variety of the target molecule, the solid-state nanopore has demonstrated its ability of protein sequencing,[3] single nucleotide polymorphism discrimination,[4] protein-protein interaction analysis, and drug screening.[5, 6]

In the device aspect, fabricating and utilizing multi-nanopore structure is still of a huge interest to increase the throughput and the accuracy of the biological sensing. To achieve the multi-nanopore structure, semiconductor fabrication technologies such as electron beam (e-beam) lithography and atomic layer deposition (ALD) were suitable for formation and opening size control of the nanopore array (Figure 4-1).[7-9] Nevertheless, there still remains a long way to reach to the DNA sequencing using the solid-state multi-nanopore device. The major hurdle is fabricating uniform nanopores in the size of a few nm; this is crucial in increasing the detection accuracy, but it is difficult to achieve with the current fabrication technology.

Still, the nanopore array is an appealing structure that the throughput of detection, analysis, or any operation in the nanopores can be greatly enhanced. Therefore, the solid-state nanopore society has begun to seek for applications other than the electrical detection of biomolecule using the nanopore array. For instance, Wanunu group designed nanopore zero-mode waveguide (ZMW) DNA sequencing device,[10-12] as illustrated in Figure 4-2. The original ZMW consists of multiple nanowells having ~100 nm width and length. Inside each well, biotin is anchored on the wall so that it

could immobilize a DNA-streptavidin complex. Fluorescent dyes are attached to the DNA sequence of interest so that the sequence information could be gathered by fluorescence detection.[11] In the nanopore ZMW, the DNA capture rate inside the waveguides was increased by integrating the nanopore to the ZMW structure (final structure similar to the guide-inserted device designed in chapter 2) and electrically dragging DNA to the nanopore. In contrast, DNA capture to the original ZMW relied only on diffusion, thus it had fundamental limitations on the detection efficiency.

As demonstrated in the above example, the recent strategy in the solid-state nanopore and related system is to propose a new application where controlling the nanopore size or fabricating small-sized nanopore is less important. In addition, the fabrication efficiency is becoming more significant as the degree of nanopore multiplexing increases. In that sense, nanopore ZMW still required individual nanoporing inside each ZMW well, which greatly reduced the fabrication throughput and practical applicability of such device.[11]

In this chapter, a new application of a multiple nanopore array, nucleic acid preparation by electrical particle transport, will be proposed. In the fabrication of the nanoporous structure, the nanoimprint technique was employed for the high-throughput process of creating an ordered array of uniform nanopores. The discussions on the application will cover from the operation principle in the next section to the practical demonstration using a clinical biosample.

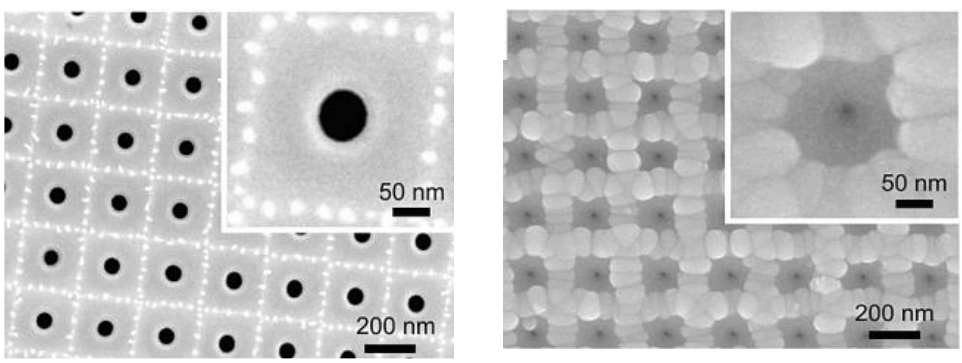

Figure 4-1 Multi-nanopore platform. TEM images of a multi solid-state nanopore array (left) and a diameter-controlled array using ALD (right). Figures were adapted with permission from ref.[9]. Copyright 2009 American Chemical Society.

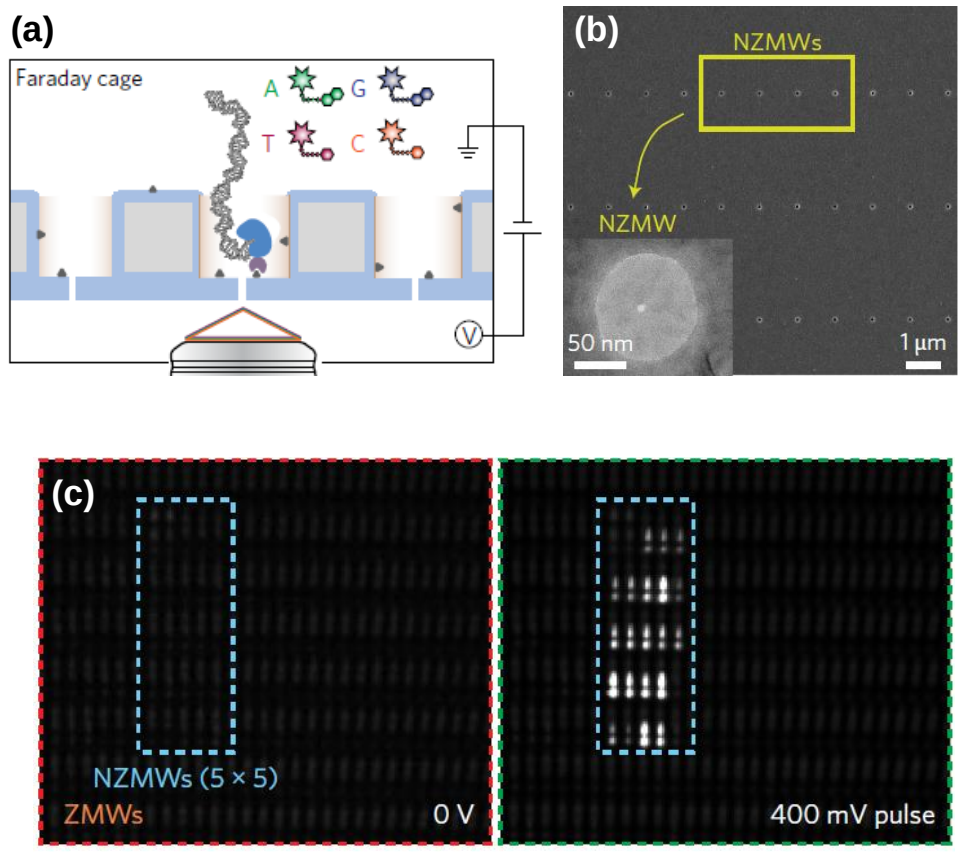

Figure 4-2 Application of multiplexed solid-state nanopore structure; nanopore zero-mode waveguide (NZMW). (a) conceptual image of NZMW DNA sequencing. (b) SEM micrograph of the fabricated NZMW array with a closed-up TEM image of single NZMW. (c) voltage-driven captures to the NZMW. Figures were adapted with permission from ref.[11]. Copyright 2017 Springer Nature.

4.1.2 Electrophoretic Biomolecule Transport Principle using Multi-Nanopore Device

Naturally, a nanoporous membrane is a good molecular sieve, as such structures have been actively utilized as molecular filters and separators.[13-15] Here, applying an electric field across the nanoporous membrane can add functionality in molecular separation. The most popular example of the electrical separation using a porous structure is gel electrophoresis, where biomolecules of different sizes and charges are discriminated inside a microporous gel mesh upon the electric field.

Similarly, the electric field across a nanoporous membrane can discriminate biomolecules by size and charge. In the schematic image of Figure 4-3, negatively charged molecules in the chamber on the left are driven to the opposite chamber by the positive voltage applied at the right end. In contrast, positively charged molecules and particles of a size larger than the pores would be unable to transport to the chamber at the right.

The size and electrical charge are the evident principles of the electrical separation of biomolecules. The third principle is based on the electrophoretic mobility of the biomolecules. As discussed in chapter 2, electrophoresis is the major driving force in the electrical transport of DNA. Electrophoretic velocity v_{EPH} here also can be explained by Equation 2-1, and the molecular flux induced by electrophoresis J can be described as Equation 4-1:

$$J = cv_{\mathrm{EPH}} = c\mu_{\mathrm{EPH}}E \qquad (4-1)$$

where c is the molecular concentration of transporting species, μ_{EPH} is the electrophoretic mobility of the molecule, and E is the electric field. Therefore, not only the transport velocity but also the amount transported during a given time is directly related to the electrophoretic mobility of the biomolecule.

Table 4-1 summarizes μ_{EPH} of biomolecules that are easily found in biosamples.[15-18] μ_{EPH} of DNA is constant regardless of the

chain length of the charged polymer.[16, 19] Albumin and hemoglobin are blood proteins, and lysozyme is contained in a large amount in egg white. At pH 8, DNA has 2−10 times larger μ_{EPH} than the selected proteins. Therefore, in the same condition and with the same initial concentration, DNA is expected to transport across the nanoporous membrane in a larger amount than the other biomolecules.

An application field where DNA transport and separation can be applied is nucleic acid preparation from biosamples.[20, 21] Nucleic acids in biosamples should be isolated from the other materials coexisting in the mixture such as proteins, cell debris, antigens, and wastes.[22] In the following sections, the designed setup and the feasibility of the electrophoretic nucleic acid preparation will be examined in detail. Before the confirmation, conventional nucleic acid preparation methods will be reviewed.

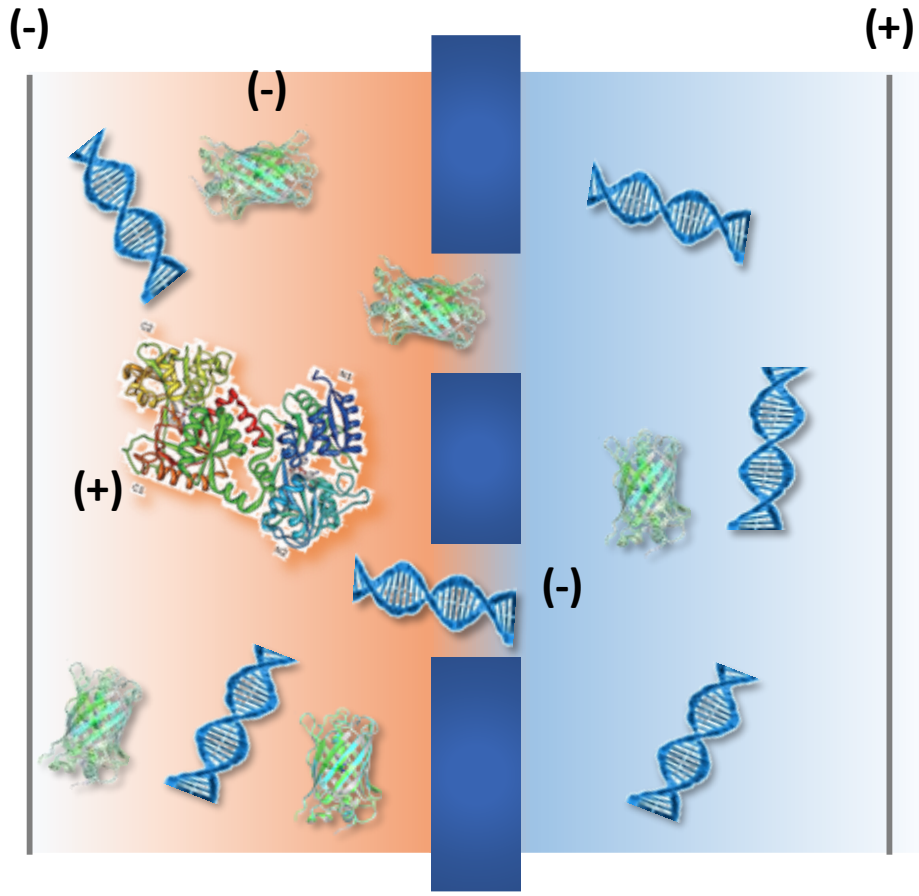

Figure 4−3 Electrophoretic biomolecule transport principle using a nanoporous structure. Signs of voltage applied on the electrode and net charges of the molecules are indicated. The images of the protein molecules were adapted with permission from ref.[23] under the terms of the Creative Commons Attribution License (CC−BY). Copyright 2012 Arpino *et al.*; ref.[24]. Copyright 2014 Springer Nature.

	DNA	Albumin	Hemoglobin	Lysozyme
$\lvert\mu_{EPH}\rvert$ (10^{-4} cm^2/Vs)	3.5−4	1.8	~0.7	~0.4

Table 4−1 Electrophoretic mobility magnitudes (at pH 8) of selected biomolecules commonly found in biosamples.[15−18]

4.2 Nucleic Acid Preparation Systems

4.2.1 Conventional Nucleic Acid Preparation Systems

Nucleic acid preparation is a biosample pre-treatment step performed before the actual genetic analysis. The quality of nucleic acid prepared affects the quality of the final result, so producing a clean and stable nucleic acid sample from the sample is important for its reliable analysis.[25]

A chemistry-based nucleic acid preparation protocol is well established in the laboratories and the market, and it is perceived as a conventional and standard pre-treatment method. Figure 4-4 graphically summarizes a phenol/chloroform extraction protocol, which can be divided into lysis, separation, binding and washing, and elution stages.[21, 25-27] Lysis is the first stage conducted to bring out the nucleic acid from cells, where the cell membrane is broken chemically, mechanically, or thermally.[25] The cell contents are of diverse molecules including DNA, RNA, miRNA, and proteins. Therefore, after lysis, a primary separation stage is incorporated which employs like-dissolves-like principle.[26, 28, 29] The aqueous sample with the lysed cell (lysate) is aggressively mixed with an organic solvent, phenol/chloroform in this case. When the mixture is centrifuged, the polar (water) and the nonpolar (phenol/chloroform) solvents are separated in the tube. By principle, polar molecules such as nucleic acid and hydrophilic proteins stay in the aqueous layer, whereas less polar substances like lipids and other less hydrophilic proteins are dissolved in the organic solvent. Consequently, only the aqueous phase is collected to move on to the next steps.

Next, the primarily separated nucleic acid is attached to the binding media, silica membrane or magnetic beads in general. The DNA binding to the silica surface is promoted by chaotropic salt, which acts as a positive ionic bridge between the negatively charged silica surface and nucleic acid.[21, 30] Nucleic acid has high linear negative charge density, so the molecules competitively bind to the

positively charged salt bridge. In contrast, other biomolecules lose in the competition to be chemically attached to the silica surface and are washed away from the binding media using alcohol-based washing buffers. After a few washing steps, the purified nucleic acids are detached from the binding media by switching the salt concentration or pH of the buffer. By changing the environment, the chaotropic cations are set free from the silica membrane, thus destroying the interaction between the surface and nucleic acid.[25] After this final elution stage, a clean nucleic acid solution is obtained and proceeded to further analysis.

Although it was briefly summarized above, the conventional, chemistry-based preparation protocol is complex, consists of more than 10 steps and takes more than an hour to complete. The process involves the use of heavy instruments such as heater and centrifuge and requires a skilled operator to prepare the nucleic acid in high purity and reproducibility. In addition, toxic chemicals such as phenol and chloroform are often used in preparing the nucleic acid.

Therefore, alternative nucleic acid protocols have been suggested to overcome the inconveniences of the conventional method. The biggest concerns in developing such alternative methods were user-friendliness and efficiency of the operation, as well as its applicability to on-site genetic analysis outside the laboratories. The new protocols include lab-on-a-chip based nucleic acid preparations, which will be discussed in the following section.

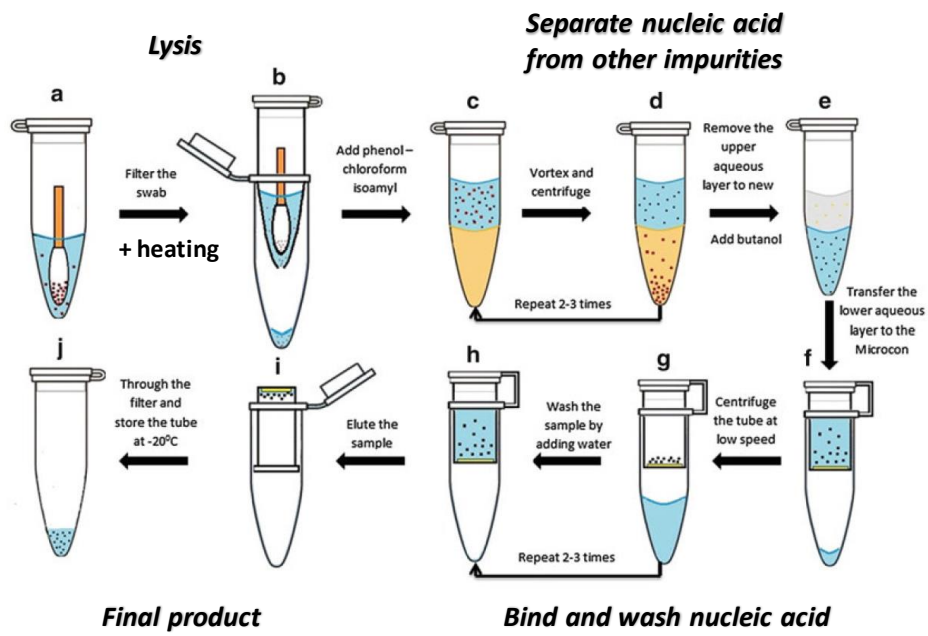

Figure 4−4 Conventional phenol/chloroform nucleic acid extraction method. The protocol is summarized with brief explanations of each stage. Figure was adapted with permission from ref.[27]. Copyright 2016 Springer Science Business Media New York.

4.2.2 Lab-on-a-Chip Based Nucleic Acid Preparation Systems

Preliminarily and fundamentally, the lab-on-a-chip nucleic acid preparation systems were designed to integrate the conventional system into a single chip. One of the earliest and the simplest form of such chips was a microfluidic channel with the binding media inserted in the middle of the channel (Figure 4-5(a)).[31, 32] Lysed sample, washing buffer, and elution buffer were sequentially injected in one end of the microchannel, and the waste was flown to another channel end. Nucleic acid was bound to the silica bead in this example, and the eluted DNA or RNA was collected in the channel outlet in the final step.

The simple channel form was developed into more delicate and effective systems, which shared the same principle and process sequence with the conventional protocol.[21, 33] Recently and notably, in 2018, an automatized nucleic acid preparation system was developed by Kim *et al.* (Figure 4-5(b)).[34] Here, the whole extraction buffers and chambers were packaged in a disc-shaped single-use utensil. The binding media in this work was silica-coated magnetic beads. The channel openings were controlled by a programmed magnetic pump switch integrated with a centrifuge. The centrifuge was used in gravitational separation of the matter and sample shaking by changing the rotation direction back and forth. All process was completed automatically in less than 30 minutes. Using this system, cell-free DNA was successfully extracted from human blood serum and studied to monitor the gene mutation levels during drug therapy of lung cancer patients.

As described above, the majority of the lab-on-a-chip nucleic acid preparation methods were based on the same chemical principle as the conventional protocol. Alternatively, physical separation of nucleic acids was demonstrated, motivated by dielectrophoresis under alternative current (AC) electric field (Figure 4-5(c)).[35, 36] The chip used in this method was a flat device with platinum (Pt) electrodes embedded in a repeating pattern, rather than being composed of microchannels. First, a biosample was

dropped onto the device, and a spatially nonuniform AC field was applied via the Pt electrodes. From the spatial electric field gradient and the differences in the electric polarizability between the media (blood) and the biomolecules, each particle experienced different dielectrophoretic field on the chip.[37] For instance, nucleic acids with high charge polarity were strongly attracted to the electrodes, whereas less polar molecules were pushed out to the area in between the electrodes.[36] Therefore, after washing the weakly bound molecules out, only the nucleic acid could be collected in time as short as 10 min for further genetic analysis. This physical principle proposed a simple process, where nucleic acids could be separated from the impurities by just applying the electric voltage to a fabricated chip.

To summarize, the lab-on-a-chip based nucleic acid preparation strategies all succeeded in developing simpler and faster protocols than the conventional method. In addition, by using a small chip and microchannels, the volumes of the sample and the buffer used in the processes were significantly reduced, increasing the economic efficiency of the extractions. However, despite the simplicity and efficiency were enhanced, the alternative systems still required heavy apparatus, namely liquid injector, centrifuge, or AC power supply, to complete the process. Hence, there still have been needs for a new nucleic acid preparation method with a more compact setup and high operation throughput.

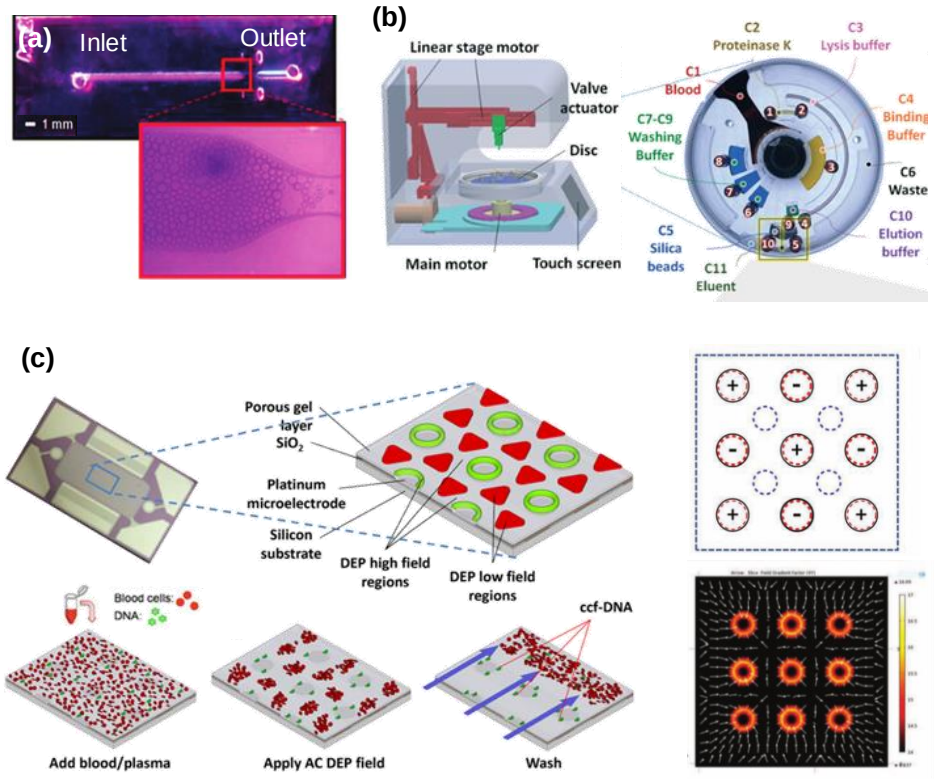

Figure 4-5 Lab-on-a-chip nucleic acid preparation methods. (a) microfluidic channel-based preparation chip with the image of silica beads (~30 μm diameter) in the inset. (b) automated cell-free DNA preparation system with a centrifuge (left) and a disc utensil (right). (c) dielectrophoretic direct separation of cell-free DNA protocol (left), mapping of the voltage signs applied (right, top) and the simulated dielectrophoretic force field on the separation chip (right, bottom). Figures were adapted with permission from (a) ref.[31]. Copyright 2008 American Chemical Society; (b) ref.[34]. Copyright 2018 Royal Society of Chemistry; (c) ref.[36]. Copyright 2014 WILEY-VCH Verlag GmbH & Co. KGaA, Weinheim (left); ref.[37]. Copyright 2013 WILEY-VCH Verlag GmbH & Co. KGaA, Weinheim (right).

4.3 Design and Setup of the Electrophoretic Nucleic Acid Preparation System

4.3.1 Design of the Electrophoretic Nucleic Acid Preparation System

The electrophoretic nucleic acid preparation system was developed with a focus on the simplicity and ease in the construction and operation of the system as well as the system stability. In establishing the new preparation system, 3 factors were mainly considered. The first design component was the chambers. In the chambers, especially in the reservoir chamber, the electric field should be generated evenly throughout the whole area so that the negatively charged nucleic acids could be smoothly driven to the separation layer. The electrical consideration was useful in determining the shape of the chambers, in that the electric field distribution could be predicted using the FEM simulation. Here, only the electrostatics physics was employed to map the electric field magnitude inside the chambers for simplicity. In a set of square-shaped chambers, there were blind areas of the electric field at the chamber edges (Figure 4-6). In contrast, the electric field built in trapezoidal-shaped chambers was relatively uniform, which would be more favorable for the smooth and even transport of the charged molecules. The dimensions of the chambers were decided based on the sample volumes used in the conventional protocol, ~100 μl of the biosample and 10-50 μl of the elution buffer.[28]

The second factor to consider was the electrode. In this system, Pt electrodes were used to eliminate electrochemical reactions that can occur on the electrodes and ensure the chemical stability of the collected nucleic acid as much as possible. Pt is well known as an electrochemically inert electrode, only acting as a catalyst in water electrolysis reaction above 1.23 V in the standard state (1 M, 25°C, 1 atm).[38] In addition, the Pt electrode is a familiar tool in the biological process, from that the electrode is used in gel electrophoresis experiments. On the other hand, electrochemical

reactions occurring at Ag/AgCl electrodes produce AgCl salt precipitate at the anode,[38] as experimentally observed at 0.5−2 V (Figure 4−6(b)). After electrophoretic collection of nucleic acid using Ag/AgCl electrodes, the genetic analysis of the prepared sample was impossible. This was possibly because the enzymes or nucleic acids in the sample aggregated to the AgCl seed instead of participating in gene amplifications.

The third and the most important feature in the electrophoretic preparation system was the separating porous layer, which will be described in detail in the following section.

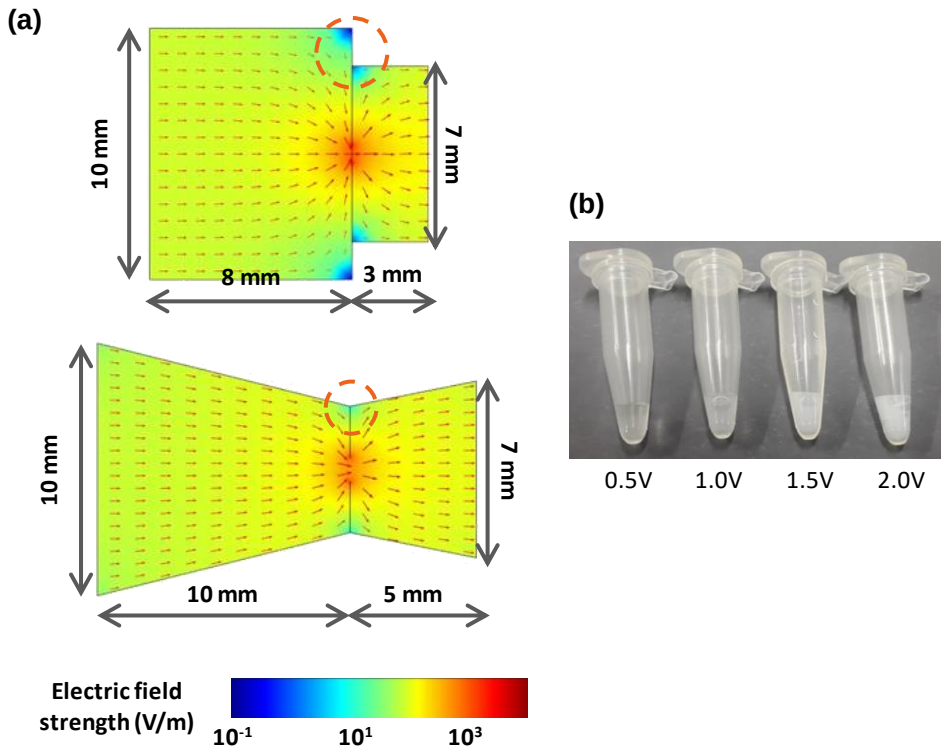

Figure 4-6 Chamber structure and electrode material design of the electrophoretic nucleic acid preparation system. (a) dimensions and electric field mapping of the rectangular-shaped chamber (top) and the trapezoidal-shaped chamber (bottom). Dashed circles indicate the blind area of the electric field at the chamber edges. The electric field strength color scale is presented below. (b) AgCl precipitates formed after applying 0.5-2.0 V to the electrophoretic system for ~10 minutes. (b) is in courtesy of Jaehyun Kang, SNU.

4.3.2 Fabrication of the Nanofilter Membrane Device

(nanoimprint lithography conducted by Dr. Junhyoung Ahn and Dr. JaeJong Lee, Korea Institute of Machinery & Materials (KIMM))

In designing the nanoporous separation layer, 3 factors were taken into account: high molecular transport rate, capability to exclude large debris or cells, and reliability in fabrication. The layer should be able to prevent the mixing of the buffers in the two chambers and act as an effective path of mass transport at the same time. In this aspect, commercially available molecular filter membranes were inappropriate for the electrophoretic preparation in this work due to their μm-10 μm order thickness.[13]

Therefore, creating a thin, robust, and porous membrane was crucial in establishing the electrophoretic nucleic acid preparation system. SiN_x was the excellent choice for the membrane material, given that it has been a standard membrane material for the solid-state nanopore with its high robustness and processability. In addition, the semiconductor fabrication technique including lithography and etch is effective in forming a multi-nanopore structure with a highly aligned network of uniform pores.

Figure 4-7 presents the fabrication procedure of the nanoporous SiN_x membrane based on nanoimprint lithography technique.[39-41] In this work, the chip containing the membrane was named 'nanofilter membrane device'. Among the semiconductor fabrication technique, nanoimprint lithography had superior simplicity and efficiency of the process, where a reusable nanoimprint mold was simply stamped onto the resist to create the desired pattern. Similar to the solid-state nanopore fabrication, the process started from low-stress SiN_x LPCVD to 500 nm thickness on a double-side polished Si wafer. On one side of the SiN_x/Si/SiN_x wafer, poly(urethane acrylate (PUA) nanoimprint resist was spin-coated to 250 nm thickness. The resist was cured using an ultraviolet (UV) ramp to create the nanoporous pattern (Figure 4-7(b)).[40] After the nanoimprint process, the patterned SiN_x was trenched by inductively coupled plasma (ICP) etching (Figure 4-7(c)). Since the SiN_x film

should also act as the mask for Si wet etch, the porous structure should be partially etched. From the low etch selectivity of SiN_x to PUA, the resist layer was completely removed during the partial etch process. Next, the free-standing membrane was created using the same method as in solid-state nanopore fabrications (section 1.3). The trenched pattern was further etched from the backside of the membrane to form the fully perforated nanopore paths.

The photograph and the SEM micrograph of the completed nanofilter membrane device are shown in Figure 4-8(a), with those of the commercially available membrane filter for comparison (Figure 4-8(b)). In Figure 4-8(a), the nanofilter membrane of a 1 mm width was formed at the center of a 1 cm-wide Si chip. The width of the membrane was decided upon the mechanical stability of the porous membrane; larger membrane would be favorable for high molecular transport rate but would be more physically vulnerable during handling and the operation. The thickness of the membrane was determined by the same reasoning; thinner membrane would allow faster transport but would be difficult to handle.

The most important design factor for the nanofilter membrane device was the size of the nanopores. In this work, the nanopore diameter was set as 200 nm based on the reliability in fabrication and ability to exclude large impurities in the biosamples during nucleic acid preparation. The minimum feature size that could be reliably patterned using nanoimprint was >100 nm, following that of e-beam lithography used in creating the PDMS mold. Considering the typical sizes of biological cells, ~μm, the 200 nm-sized nanopores would be effective in eliminating the transport of large particles across the nanofilter membrane. In the completed device, the pore density of the nanofilter membrane was 7.22×10^8 cm^{-2} (Figure 4-8(a), bottom).

As presented in Figure 4-8 and Table 4-2, the properties of the fabricated nanofilter membrane were clearly distinguished from those of the commercially available membrane filter. The most critical feature was the membrane thickness, where the nanofilter membrane was thinner than the membrane filters by at least an order of magnitude. The nanopores fabricated in this work were evenly

distributed throughout the whole membrane, straightly perforated, and arranged as a high porosity network. In contrast, the membrane filter had a nonuniform and relatively sparse arrangement of skewed channels. Furthermore, the SiN_x nanofilter membrane showed excellent chemical stability compared to the polymer-based membrane filters.

In summary, the nanofilter membrane device was designed to facilitate a high rate of molecular transport across the nanopores and ensure the mechanical stability of the membrane during the nucleic acid preparation. As a result, the device was successfully fabricated by incorporating the nanoimprint fabrication technique. The nanofilter membrane of sub-micron thickness and an ordered network of uniform 200 nm-sized nanopores effectively allowed the molecular transport as compared to the thick membrane filter, where the molecular transport was hardly detected through the thick membrane.

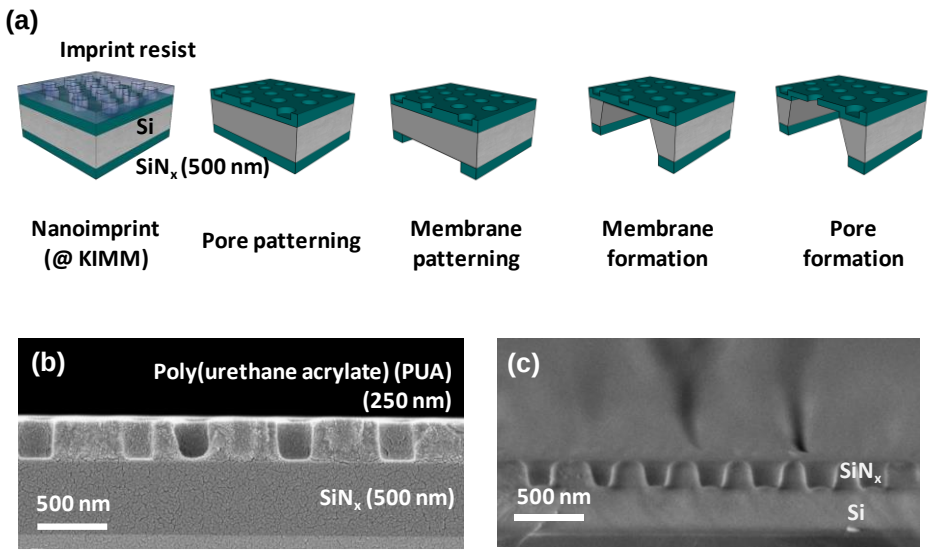

Figure 4-7 Fabrication of the nanofilter membrane device. (a) the fabrication process of the nanofilter membrane device. The image is not in scale. (b)-(c) cross-section SEM micrograph after (b) nanoimprint step and (c) pore patterning step in (a). Each part is labeled in the figure with 500 nm scale bars. (a) was adapted with permission from ref.[1] under the terms of the Creative Commons Attribution License (CC-BY). Copyright 2020 Lee *et al.* (b) and (c) are in courtesy of Jaehyun Kang, SNU.

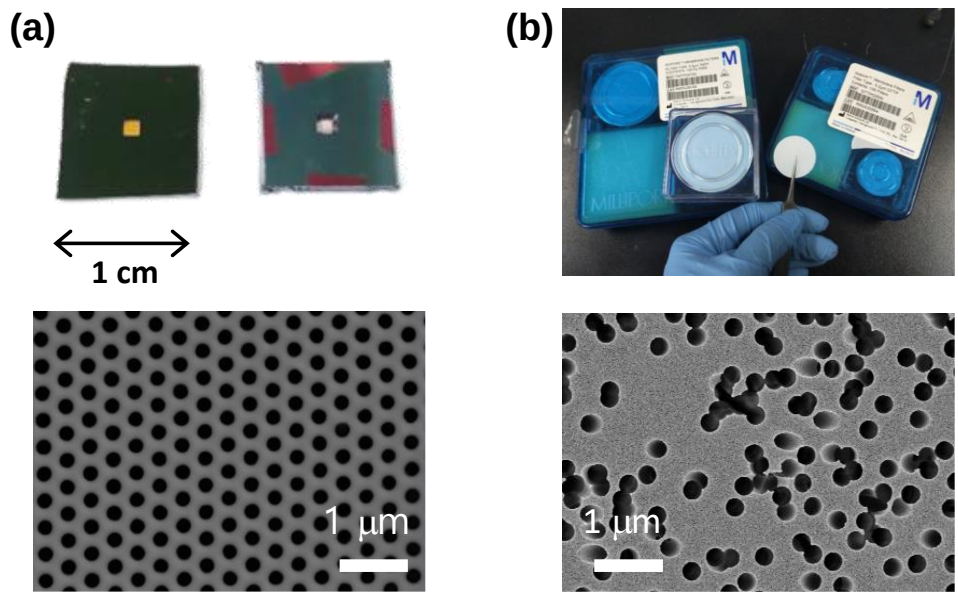

Figure 4-8 Fabricated nanofilter membrane device and commercial membrane filter. Device or filter images (top) and SEM micrograph of the porous structure (bottom) of the (a) nanofilter membrane and (b) commercial membrane filter (Isopore®). Figures were reproduced with permission from (a) ref.[1] under the terms of the Creative Commons Attribution License (CC-BY). Copyright 2020 Lee *et al.*.

	Nanofilter membrane	Commercial membrane filter
Thickness	100 nm	> μm
Pore size	200 nm	100 nm−10 μm
Pore distribution	Uniform	Random
Pore alignment	Straight	Skewed
Porosity	High	Moderate
Membrane width	1 mm	1−10 cm
Material	SiN_x/Si	Polymer (polycarbonate, nitrocellulose)
Chemical stability	Excellent	Moderate−Low
Molecular transport	Detectable	Below detection limit

Table 4−2 Comparison of the nanofilter membrane fabricated in this work and the commercially available membrane filters.

4.3.3 Electrophoretic Nucleic Acid Preparation Setup

The finalized electrophoretic nucleic acid preparation setup is shown in Figure 4-9. The system was basically an assembly of a pair of chamber cells, a nanofilter membrane device, 2 PDMS blocks to prevent the sample leakage, and a pair of electrodes. The components were put together simply by tightening the screws through the holes in the chamber cells. In the system, the chamber where the biosample was injected was named a reservoir chamber, and the compartment where the nucleic acid was collected by the electric field was named a collection chamber. The positive direct current (DC) voltage was applied to the collection chamber via the electrodes, each immersed in the biosample and the collection buffer.

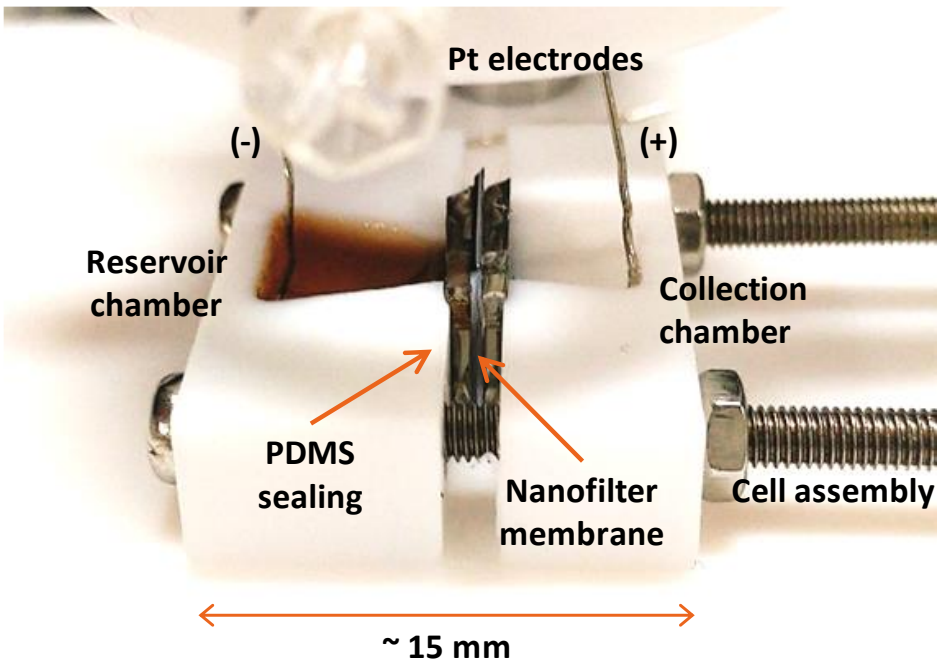

Figure 4−9 Electrophoretic nucleic acid preparation setup. Each part is explained throughout section 4.3.

4.4 Experimental Details

4.4.1 Experimental Details

The detailed fabrication method of the nanofilter membrane device generally followed that of solid-state nanopore fabrication in sections 1.3, 2.3.1, and 3.3.1. Nanoimprint lithography was conducted as previously reported and explained in the above section.[39-41] The electrophoretic nucleic acid system was assembled as presented in section 4.3.3. The cell compartments were formed using Teflon® for repeated use after hot piranha solution cleaning. The PDMS blocks were formed in 1 cm width, and a 3 mm-diameter center hole was punched on each block. A pair of Pt electrodes (ALS, Tokyo, Japan) was bent in L-shape to cover the chamber width and immersed in the chambers, as displayed in Figure 4-9.

The target nucleic acid molecule of transport was microRNA (miRNA), specifically human miRNA hsa-mir-93-5p (miR93-5p). miRNAs are ~20 nucleotides (nt)-long single-strand noncoding RNAs participating in the post-transcriptional regulation of the gene expression.[42, 43] Some miRNAs including miR93 are closely related to tumor growth and cell survival, and the abnormal proliferation or depletion of the genes in the body can be cancer biomarkers.[44-46] Meanwhile, miRNAs of 20-22 nucleotides are very short molecules in a biofluid, having ~6 nm chain length. The small molecules thus are difficult to isolate from the biofluids even using the conventional pre-treatment protocol.[26] Therefore, if the electrophoretic miRNA preparation was successful from biofluids such as blood, it could be of a high impact on easy and simple cancer diagnosis.

In the proof-of-concept experiment, the electrophoretic transport principle was confirmed using miR93-5p. Here, the reservoir and the collection chambers were each filled with 150 μl of 100 pg/μl miR93-5p mimic in 1X TE buffer and 75 μl of pure 1X TE buffer, respectively. miR93-5p mimic was synthesized by and purchased from Genolution (Seoul, Korea). 1X TE buffer (pH 8.0,

RNase- and DNase-free) was purchased from Sigma-Aldrich (St. Louis, USA). The concentration of miR93-5p mimic was decided based on the typical cell-free nucleic acid concentrations in the blood of cancer patients.[47, 48] The reservoir volume was determined from the starting biosample volume of the conventional preparation method, but the collection buffer volume was larger than the suggested elution volume of the chemical protocol (10-20 μl).[28] In the electrophoretic method, ~20 μl collection buffer significantly dried during the experiment. Therefore, for the stability of the buffer, the sufficient collection buffer volume of 75 μl was selected. 1-10 V was applied to the collection chamber for 30 minutes using Keithley® 237 instrument (Keithley Instrument, Washington D.C., USA), where the time was also set based on the conventional method, to be less than a half of the operation time of the chemical pre-treatment kit (1-1.5 hr).[26, 28] 7 runs for each voltage condition (1, 2, 5, 10 V) were performed electrophoretically, and 3 runs at 0 V were also conducted to check the diffusive contribution to the molecular transport across the nanofilter membrane.

In the experiment with the clinical biosample, human blood serum samples donated by hepatocellular carcinoma (HCC) patients and healthy individuals were used. miRNA preparation from the serum samples was performed upon approval by the institutional review board (IRB) of Seoul National University (SNU), IRB No. E1804/003-004, 2018-04-16. The serum samples were provided by the Biobank of Chungnam National University Hospital (healthy group) and the Biobank of Keimyung University Dongsan Hospital (cancer patients), members of the National Biobank of Korea. miRNA was electrophoretically transported from 150 μl of blood serum (reservoir chamber) to 75 μl of pure 1X TE buffer (collection chamber), under 2 V for 30 min. The reasoning for setting 2 V as the operating voltage will be explained in sections 4.5.1 and 4.5.2. To assess the effectivity and the efficiency of the electrophoretic protocol, the same serum samples of the same volume (150 μl each) were chemically processed using miRNeasy® serum/plasma kit (Qiagen, Hilden, Germany). To reduce the variance which could be

caused by the difference in the elution volume, miRNA bound to the silica membrane was collected using 75 μl elution buffer instead of ~14 μl suggested by the kit manufacturer. Other than the final elution volume, the chemical process was completed following the manufacturer's protocol. The electrophoretic experiment was conducted 3 times, while the conventional extraction was only performed once for each serum sample. The small numbers of repetitions were due to the limited amount of serum provided (600–700 μl for each donor).

After each 30–min electrophoretic run and also after the conventional extractions, the collected miRNA was processed via reverse transcription (RT) reaction, followed by quantitative polymerase chain reaction (qPCR). To confirm the molecular stability and integrity of the amplified product, melting curve analysis or gel electrophoresis was conducted after qPCR. In section 4.5.4, the electrophoretically and the chemically prepared miRNA from the human blood serum were analyzed using ultraviolet–visible (UV–Vis) spectrophotometry to identify the chemical species in each extract. The detailed experimental procedures of the biological and biochemical analysis will be explained in the following section.

4.4.2 Analytical Methods and Protocols

4.4.2.1 Reverse Transcription-Quantification Polymerase Chain Reaction (RT-qPCR)

(biological process setup supported by Mr. Wan-Jin Jeon and Dr. Jae-Hoon Lee, Heimbiotek Inc.)

RT-qPCR of the collected miRNA was performed in two steps, RT and qPCR. The RT reaction was performed no later than a day after the preparation of each miRNA sample. In the RT step, miScript II RT Kit (Qiagen) and 2720 Thermal Cycler (Applied Biosystems, Waltham, USA) were used. The recipe and the protocol are presented in Table 4-3. After the reaction was complete, the synthesized complementary DNA (cDNA) was stored at -20°C before proceeding to qPCR.

To ensure the reliability in data, triplicates of each cDNA were processed in the qPCR stage. In addition, a reference cDNA synthesized using the miRNA mimic of a known concentration (1 ng/μl) was amplified in every qPCR amplification run as a standard sample. Table 4-4 shows the recipe and the thermal protocol followed for qPCR amplification. miScript SYBR Green PCR Kit and miScript Primer Assay (hsa-miR-93-5p primers), both purchased from Qiagen, and CFX384 Touch™ Real-Time PCR Detection System (Bio-Rad, Hercules, USA) were used in the qPCR process. The qPCR machine detected the fluorescence signal of SYBR Green dye, which acted as a quantitative indicator of the amplified DNA by emitting fluorescence when adhered to dsDNA.

Figure 4-10 describes data processing after the qPCR amplification. Raw qPCR results were obtained as the fluorescence intensities of individual wells after each thermal cycle. The amplification curve in Figure 4-10(a) was the primary result of qPCR. Here, the threshold cycle (C_t) value of each well was the intersection of the amplification curve and threshold fluorescence level. After C_t, the signal intensity was beyond the background noise of the detector,

indicating the presence of the amplicons. The curves were processed using CFX Manager^{TM} software to figure out the C_t of each sample.

A derivative investigation using the fluorescence amplification signal is melting curve analysis, in which the temperature is gradually increased to measure the dissociation of the DNA strands. The fluorescence intensity (F) decreases as dsDNA dissociates into ssDNA at higher temperatures (T), and the differential decrease with the temperature (−dF/dT) can be plotted as a melting curve (Figure 4−10(b)). The temperature at the maximum −dF/dT is the characteristic temperature for the certain amplified gene, which is conventionally called a melting temperature. In this work, the melting curve analysis was used to check the specificity of amplification by comparing the melting property of the unknown sample to that of the reference sample (pure target gene of a known concentration). If the same melting results were obtained in the reference and the unknown samples, the gene amplification result of the unknown sample would be confirmed as specific and valid.

For quantification of the target gene in unknown samples, a standard amplification curve as a function of the miRNA concentration was constructed as Figure 4−11. miR93−5p mimic solutions of known concentrations (1 ng/μl to 0.1 pg/μl, 10−fold dilution) in 1X TE buffer were processed through the RT−qPCR protocol. The standard curve was plotted based on the C_t values with the initial miRNA concentrations of the corresponding samples. As a result, the empirical relationship between the miRNA concentration and the C_t was formulated as Equation 4−2:[49]

$$C_t = C_0 - s \log x \qquad (4-2)$$

where C_0 (=32.1) is the C_t value detected in 1 pg/μl miRNA solution, s (=3.19) is the slope of the standard curve, and x is the miRNA concentration in pg/μl. Using the above equation and the detected C_t values, the miRNA concentrations in the extracted samples were computed.

Component	Volume per reaction
5X buffer	2 μl
10X nucleics mix	1 μl
RNase-free water	5 μl
Reverse transcriptase mix	1 μl
Template miRNA	1 μl
Total volume	10 μl

Step	Temperature	Time
Reverse transcription	37°C	60 min
Enzyme inactivation	95°C	5 min

Table 4-3 RT reaction components and recipe (top) and thermal protocol (bottom), following the instruction provided by the kit manufacturer.

Component	Volume per reaction
2X PCR mastermix	5 μl
10X universal primer	1 μl
10X specific primer	1 μl
RNase-free water	2 μl
Template cDNA	1 μl
Total volume	10 μl

Step		Temperature	Time
Initial activation		95°C	15 min
3-step cycling	Denaturation	94°C	15 s
	Annealing	55°C	30 s
	Extension	70°C	30 s
Melting analysis			

Table 4-4 qPCR reaction components and recipe (top) and thermal cycling protocol (bottom), following the instruction provided by the kit manufacturer.

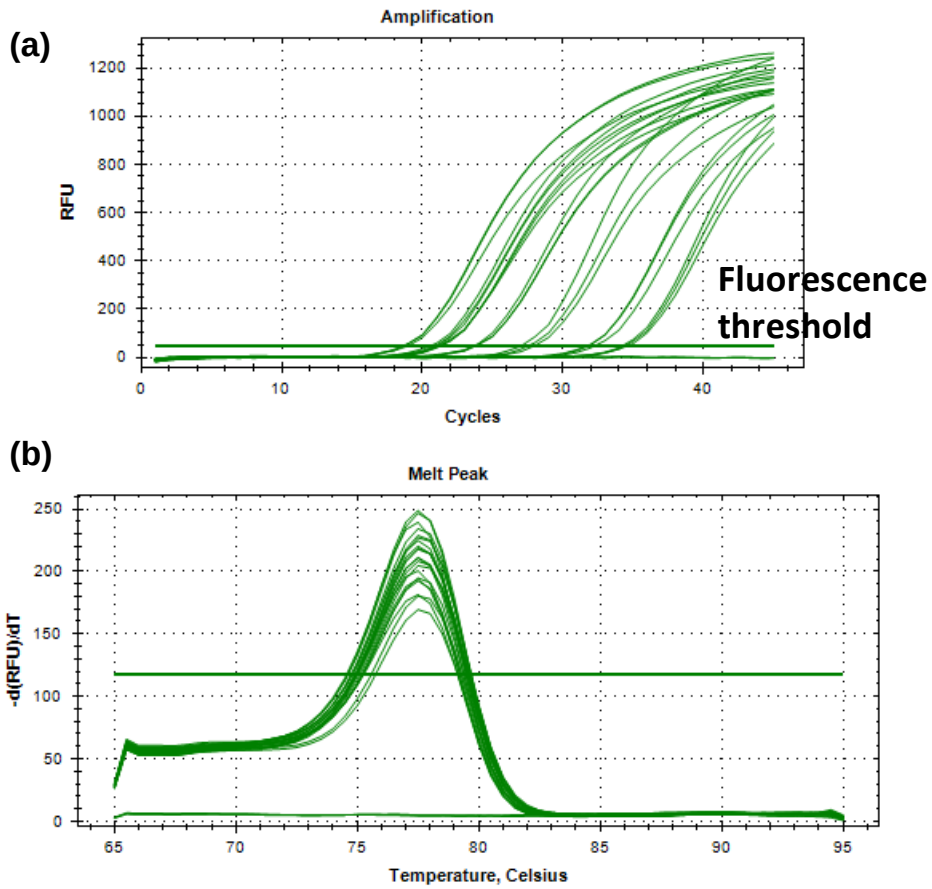

Figure 4-10 Data processing after qPCR. (a) amplification curves obtained from multiple wells in a single run. The threshold fluorescence level is marked as a horizontal line. (b) melt curve analysis from the amplified products in (a). The horizontal line is a threshold -d(RFU)/dT for melt peak recognition. -d(RFU)/dT in the figure is the same term as -dF/dT in the text.

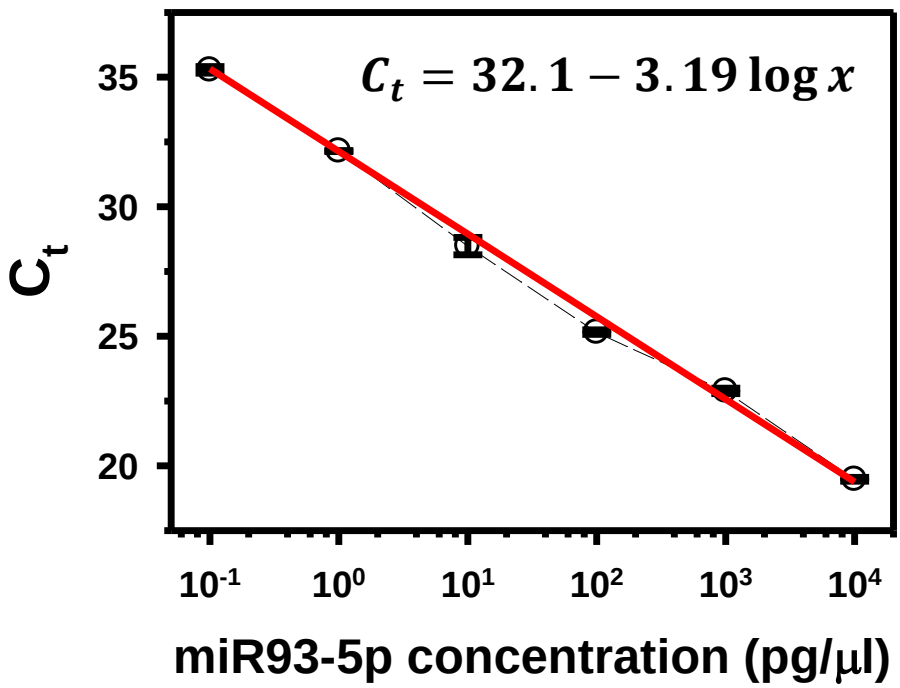

Figure 4−11 miR93−5p RT−qPCR standard curve in this work. The error bars were calculated from the results of triplicates for each miRNA concentration. The fitted curve equation in the figure is Equation 4−2, where x is miR93−5p concentration in pg/μl.

4.4.2.2 Gel Electrophoresis

Gel electrophoresis was performed after RT-qPCR to confirm the stability of the prepared miRNA. The specificity of the amplification can be validated in the melting curve analysis, but the gel test is a more certain method to prove the specificity with the stability and integrity of the amplified genes. Agarose gel was prepared by melting agarose powder in 1X tris acetate-EDTA (TAE) buffer to 2% agarose concentration, adding SYBR Safe DNA Gel Stain (Invitrogen, Waltham, USA) in 1 ml gel-to-1 μl stain ratio, and pouring the mixture in the gel template. After ~25 min, the hardened gel was immersed in 1X TAE buffer in Mupid® 2-Plus Electrophoresis System (Advance, Tokyo, Japan). Amplified products were mixed with 6X loading buffer (Bionics, Seoul, Korea), and was loaded into each comb in the agarose gel. 2 μl of 25/100 bp mixed DNA ladder was inserted in an empty comb as a reference. The electrophoresis was run for 30 min, and the gel was imaged using Gel Doc™ XR+ system (Bio-Rad, Hercules, USA). Figure 4-12 is a demonstration of the gel electrophoresis experiment and gel imaging. Unless indicated, the chemicals were purchased from Bioneer (Daejeon, Korea).

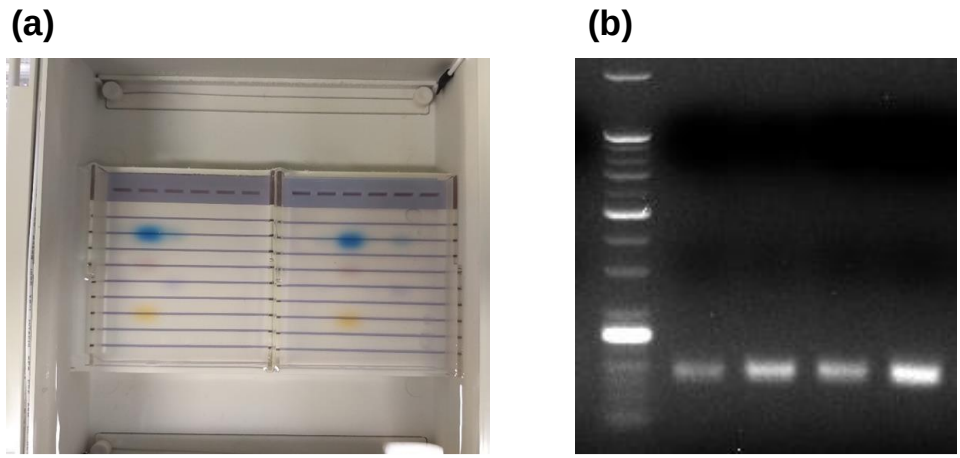

Figure 4-12 Gel electrophoresis experiments. (a) a picture of the actual gel electrophoresis setup and the processed gels. (b) an example DNA band image after a gel electrophoresis experiment.

4.4.2.3 Ultraviolet−Visible (UV−Vis) Spectrophotometry

To identify the chemical species in the electrophoretically and conventionally prepared miRNA samples from the blood serum, UV−Vis spectrophotometry analysis was performed. Here, Nanodrop® 2000 (Thermo Fisher Scientific, Waltham, USA) instrument was used, which was capable of detecting the absorbances of samples as few as ~1 μl.

Using UV−Vis spectrophotometry, the presence of chemicals and their concentrations can be analyzed. Each chemical species has a characteristic absorbance plot as a function of the wavelength, as shown in Figure 4−13(a). For instance, nucleic acids and proteins have distinct absorbance profiles, exhibiting a peak at 260 nm and 280 nm wavelength, respectively.[50] The absorbance curve of the mixture of nucleic acid and protein would result from a summation of the absorbances from each contributor. Consequently, the relative purity of nucleic acid to protein in a given sample is expressed as the ratio of absorbances at 260 nm and 280 nm, A260/280. A260/280 values of pure nucleic acid samples are 1.8 (DNA) and 2.1 (miRNA), while pure protein samples have A260/280 of ~0.6.[50, 51] Therefore, the relative DNA or RNA purity to protein in a sample increases as its A260/280 approaches to 1.8 or 2.1.

In addition to the identification, the concentrations of the species can be measured in UV−Vis spectrophotometry. The background theory for the quantification is Beer−Lambert law presented in Equation 4−3:[38]

$$A = \varepsilon bc \qquad (4-3)$$

where A is the absorbance of the sample at a given wavelength, ε is the molar extinction coefficient ($M^{-1}cm^{-1}$) at the wavelength, b is the optical pathlength, and c is the concentration of the analyte in the sample.

The optical quantification is an important and widely used feature of the analytical method. However, spectrophotometric quantification

was out of the scope of this work; miRNA quantification was performed using RT−qPCR, and only the chemical identification in the prepared samples using UV−Vis spectrophotometry was discussed in the following sections.

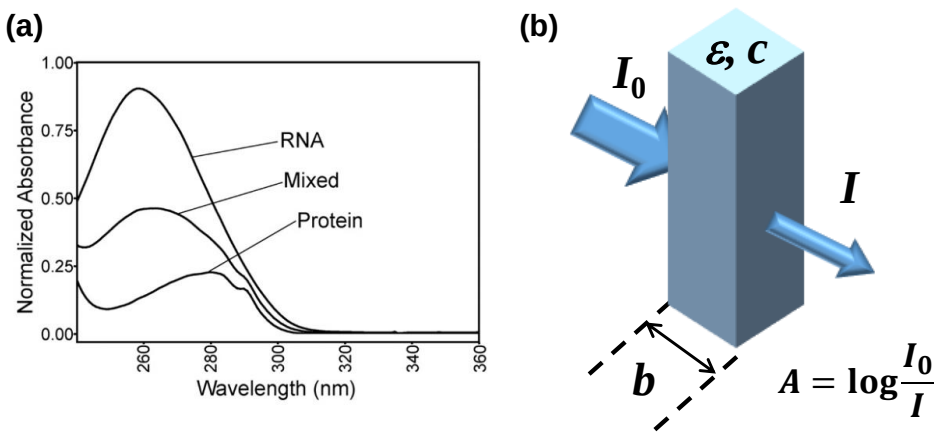

Figure 4-13 UV-Vis spectrophotometry of a biosample. (a) a model absorbance plot of pure RNA, pure protein, and a mixture of RNA and protein. (b) a conceptual image of the absorbance measurement in UV-Vis spectrophotometry. (a) was reproduced with permission from ref.[50]. Copyright 2010 Elsevier Inc. All rights reserved.

4.5 Result and Discussion

4.5.1 Proof-of-Concept of Electrophoretic Nucleic Acid Preparation

In the proof-of-concept experiment, it was tested if the miRNA molecules transported across the nanofilter membrane by the applied electric field and if the collected miRNA was compatible with the downstream RT-qPCR process. The miRNA in the reservoir chamber was forced by 1, 2, 5, and 10 V to move to the opposite chamber for 30 min. Figure 4-14 is the transported amount percentage after 7 trials under respective conditions, calculated using the quantification method explained in section 4.4.2.1 and Equation 4-4:

$$\text{Transport } \% = \frac{\text{Collected quantity}}{\text{Input quantity}} \times 100. \qquad (4-4)$$

Under all voltages, miR93-5p mimic was detected at the collection chamber, implying that the molecules transported across the membrane during all 30-min runs. Moreover, when 0 V was applied to the same setup, less than 5% of the electrophoretically transported miRNA quantity was detected in the collection chamber after diffusion. Therefore, as expected, the electrophoretic driving force induced transport of the charged nucleic acid molecules across the nanofilter membrane, though the transported quantity was as low as ~5% of the input quantity. The low number of transport % will be further discussed in section 4.5.4.

After experimentally confirming the electrophoretic transport principle, the stability and reproducibility of the transport were checked. In the gel electrophoresis result (inset of Figure 4-14), the gel band positions from the 1-10 V samples corresponded to that of the reference band. The reproducibility of transport data was maximized at 2 V, compared to the data points under 1, 5, and 10 V.

In conclusion, the electrophoretic nucleic acid preparation principle was proven valid in the model experiments using the miRNA

mimic solution. The validity and stability of the collected miRNA molecules were confirmed in gel electrophoresis, proving the compatibility of the electrophoretic preparation with the conventional downstream applications such as qPCR. In addition, 2 V was selected as the best voltage condition in terms of the reproducibility of data.

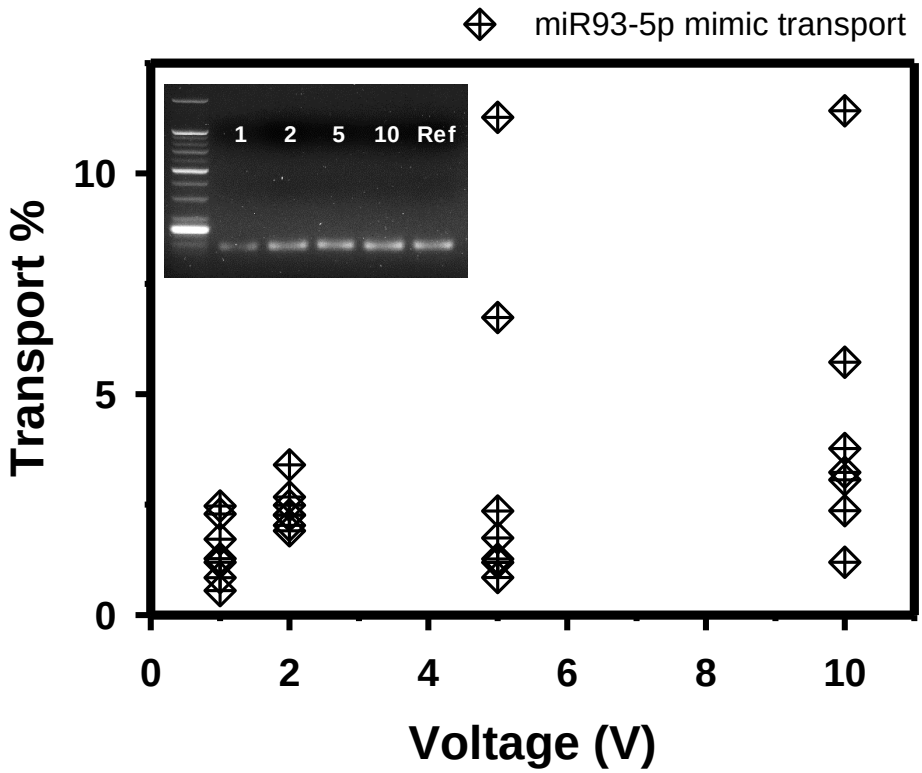

Figure 4-14 Electrophoretic transport proof-of-concept. Transport % detected as a function of applied voltage in all electrophoretic transport experiments under 1-10 V. Inset is a gel band image of the transported miRNA, where the numbers represent the applied voltage to collect the miRNA and 'Ref' indicates the pure gene for reference. Figure was reproduced with permission from ref.[1] under the terms of the Creative Commons Attribution License (CC-BY). Copyright 2020 Lee *et al.*.

4.5.2 Stability of the Electrophoretic Nucleic Acid Preparation System

Along with the collected miRNA stability and the data reproducibility, the stability of the system during and after the electrophoretic preparation was evaluated. Here, the system stability included ionic current stability and electrochemical stability of the buffers. The results are summarized in Figure 4-15.

At 1-2 V, the ionic current steadily decreased to a saturated current after several minutes. In contrast, the current continuously or abruptly dropped under 5-10 V, reflecting the electrical instability of the system in these conditions.

Similarly, the electrophoretic preparation system was also unstable at 5-10 V in the electrochemical aspect. The system, particularly the collection buffer, suffered from severe drying and fluid migration during the experiment under these conditions. Although hardly noticeable in the figure, 20-30% of the collection buffer migrated to the reservoir chamber at 5 V for 30 minutes. Under 10 V, a significant amount of the collection buffer migrated to the opposite chamber, as visible in Figure 4-15. The direction of fluid transport, from the collection chamber to the reservoir chamber, corresponded to the direction of osmosis and electroosmosis that could exist in the given system. The osmotic flow could be generated in the direction towards a highly concentrated solution, which was the reservoir sample with miRNA in this case. Following the same principle as chapter 2, electroosmotic flow generated by the electric field and the negatively charged SiN_x surface would be in the opposite direction to the miRNA transport. On the contrary, at 1 and 2 V, the volumes of each buffer stayed the same as the input after the experiments.

In addition to the instability in buffer volumes, the pH of the buffers was subject to change during the electrophoretic preparations at high voltages. The standard potential (at 1 M, 25°C, 1 atm) of water electrolysis reaction on Pt electrodes is 1.23 V, so above this voltage, the electrochemical reaction shown below can take place:

(cathode) $4H_2O + 4e^- \rightarrow 2H_2 + 4OH^-$ (pH increase)

(anode) $4OH- \rightarrow O_2 + H_2O + 4e^-$ (pH decrease)

where the pH changes following the half-reactions are marked respectively.[38] Although the electrolysis could occur at 2 V, the pH differences before and after the experiment were minimal. However, at 5 V and 10 V, the products of severe electrochemical reactions were beyond the buffering capability, as in Figure 4-15(c). With the pH changes, air bubbles were generated in both chambers under these conditions as a byproduct of the electrochemical reactions. It should be noted that the buffer migration, air bubble generation, and pH changes in the buffers were always observed in the electrophoretic experiments at 5 and 10 V. These unwanted events all would have adversely affected to the stability of the electrophoretic preparation system, thus would have been resulted as the low reproducibility of the transport % (Figure 4-14).

To conclude, considering the electrical and electrochemical stabilities during the electrophoretic preparation as well as the data reproducibility in the previous section, 2 V was selected as the optimum voltage to collect miRNA. Hereafter, all electrophoretic miRNA collections were conducted at 2 V for 30 min.

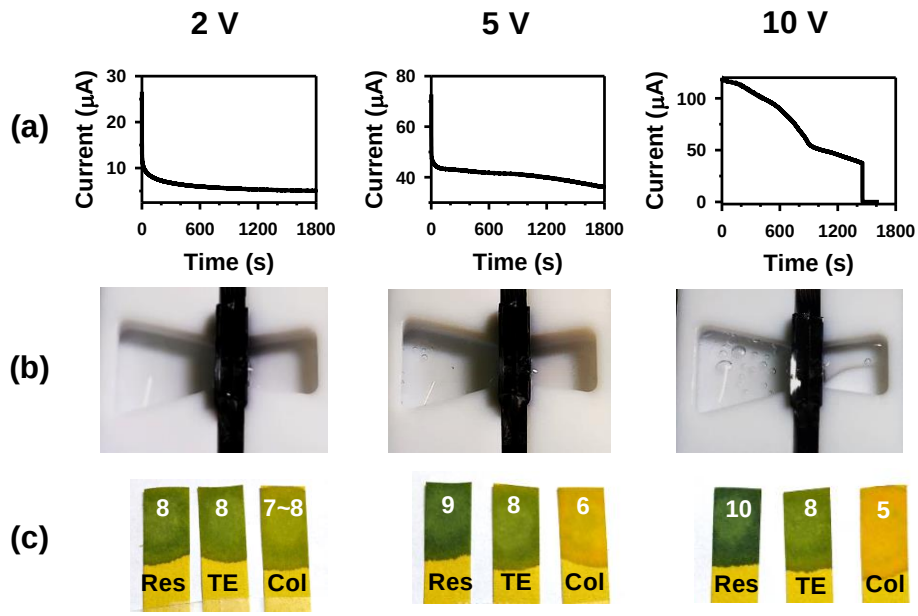

Figure 4-15 Electrical and electrochemical stabilities during the electrophoretic miRNA preparation. (a) ionic current during 30 minutes, (b) buffers in the chambers and (c) their pH changes after the 30-min runs at 2 V (left), 5 V (middle), and 10 V (right). Figures were reproduced with permission from ref.[1] under the terms of the Creative Commons Attribution License (CC-BY). Copyright 2020 Lee *et al.*.

4.5.3 Demonstration of Liquid Biopsy using the Electrophoretic Nucleic Acid Preparation System

After the electrophoretic preparation principle and the stability of the system were confirmed, the same setup was applied to clinical samples. Here, human blood serum was selected as the clinical sample to demonstrate liquid biopsy process.

Before moving on to the experimental demonstrations, liquid biopsy process and its significance should be discussed. Current biopsy method is mainly performed by taking off a part of the target tissue of analysis[52] using a large needle and optically analyzing the cells for cancerous evidence.[53] Even though the method is widely practiced, it is highly invasive, painful, difficult, expensive, and takes at least a few days to get the result. To overcome these disadvantages of the current biopsy process, liquid biopsy performed only with a small amount of blood was designed. As a cell faces apoptosis or necrosis, a part of the cell contents flows into the blood vessel. The cell contents include a small amount of nucleic acid, which exist in the blood as cell-free nucleic acid (cfNA) and migrate the whole body before it degrades.[53] If a certain cfNA was originated from a cancer cell, the nucleic acid would carry the genetic information related to the tumor. Furthermore, cell growth and death are abnormally active in cancer tissues, so that the level of cfNA could be aberrated in the blood of cancer patients than that sampled from healthy individuals.[52] Therefore, by detecting the content and the level of cfNA in blood, information about the disease – presence, type, stage, recurrence, *et cetera* – can be diagnosed or monitored.[34, 46, 52, 53]

In practice, liquid biopsy is performed mainly in 3 steps: sample collection, nucleic acid preparation, and genetic analysis.[26] The sample used in liquid biopsy is typically blood plasma or blood serum to eliminate possible interference and contamination from the blood cell DNA. This work used stored human blood serum samples provided by the National Biobank of Korea, which have been collected from anonymous HCC patients and healthy people. The sequence of

liquid biopsy demonstration in this work is displayed in Figure 4-16. Nucleic acid from the serum samples was collected using the electrophoretic system and the commercial kit to assess the efficiency of the electrophoretic protocol relative to the conventional method. The target gene was miR93-5p as in the previous section. miR93-5p was amplified using RT-qPCR of the collected samples, and the C_t values were compared. In published reports, this gene was found to be upregulated in the blood of cancer patients, including HCC patients, compared to the samples from the control group.[44, 46, 54-56]

The quantification results are summarized in Figure 4-17. The cell-free miRNA levels in blood serum could be different by the individual, so the C_t should be compared in the same sample. In each sample ID, the C_ts from the chemically prepared sample and from the electrophoretically collected miRNA were at comparable levels, suggesting that the electrophoretic miRNA preparation was as effective as the conventional extraction method. Statistically, the average C_ts detected from serum samples of the patients were 32.38 (chemical extraction) and 32.69 (electrophoretic preparation), when the values from the control samples were 33.83 (chemical) and 34.06 (electrophoretic). The C_t numbers from the cancer patients and the healthy group were similar, with only a slight decrease identified with the presence of HCC. One possible origin of the similarity would be the small number of samples tested, with n=5 for the patient group and the control group respectively.

The effectiveness of the new method should gain more significance as the protocol required the time that was only half of that needed to complete the commercial kit protocol. Further, the validities of the 2 miRNA collection methods were confirmed in gel electrophoresis and melting curve analysis (Figure 4-17(b) and Figure 4-17(c)). The gel band positions and the melting curves of the amplified miRNAs matched to each other and those from the pure miRNA.

In conclusion, liquid biopsy from the human blood serum using the electrophoretic nucleic acid preparation system was successfully demonstrated. The RT-qPCR results of the electrically prepared

sample were comparable to the values from the chemically extracted miRNA. Considering the short process time and enhanced simplicity of the electrophoretic method, the newly developed process has verified its high efficiency as compared to the conventional protocol.

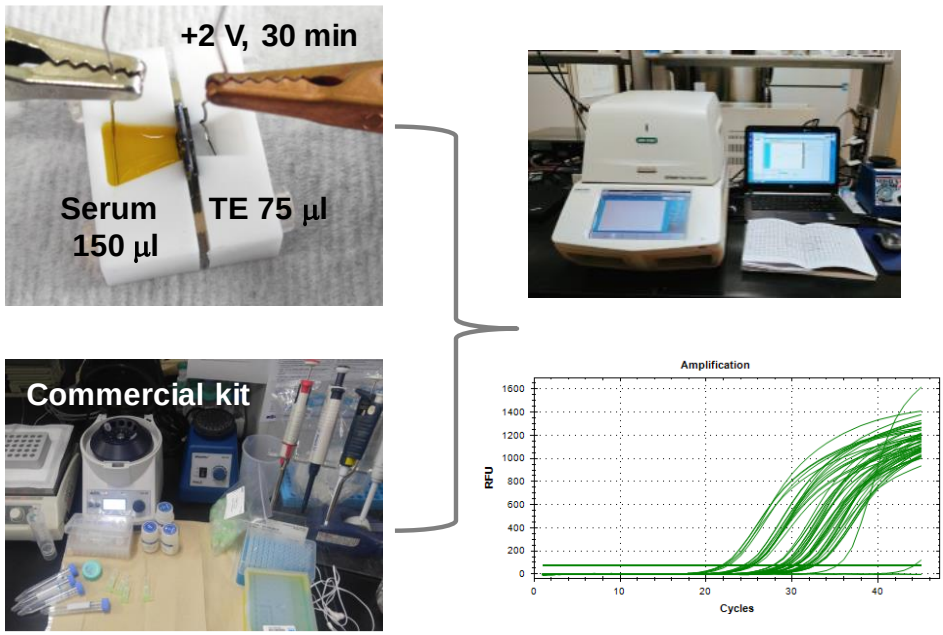

Figure 4-16 Experimental scheme of liquid biopsy demonstration in this work. After electrophoretic preparation (left, top) and commercial kit preparation (left, bottom), RT-qPCR was performed to compare the performances of the 2 methods.

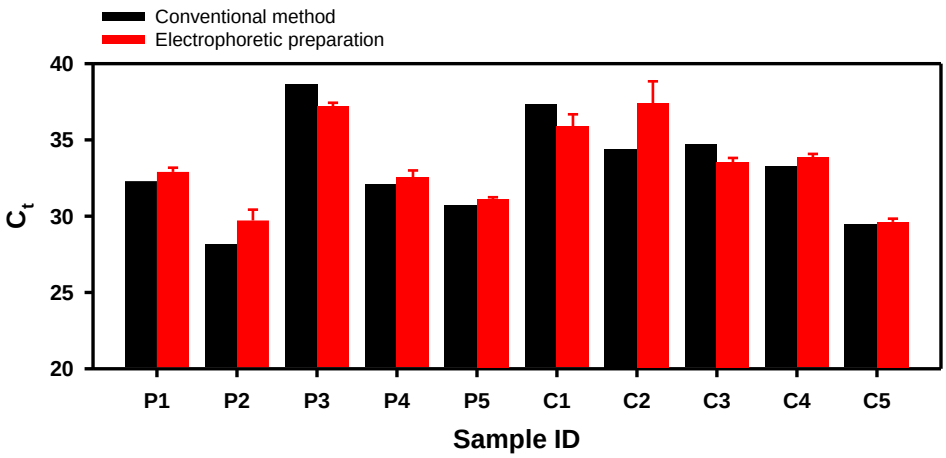

Figure 4-17 RT-qPCR results of the prepared miRNA from clinical serum samples. In sample ID, P denotes the HCC patient samples and C represents the samples from healthy controls. Kit extraction could be performed once for each sample and the error bars in the electrophoretic preparation data were calculated from three repeated experiments for the same sample. Figure was reproduced with permission from ref.[1] under the terms of the Creative Commons Attribution License (CC-BY). Copyright 2020 Lee *et al.*.

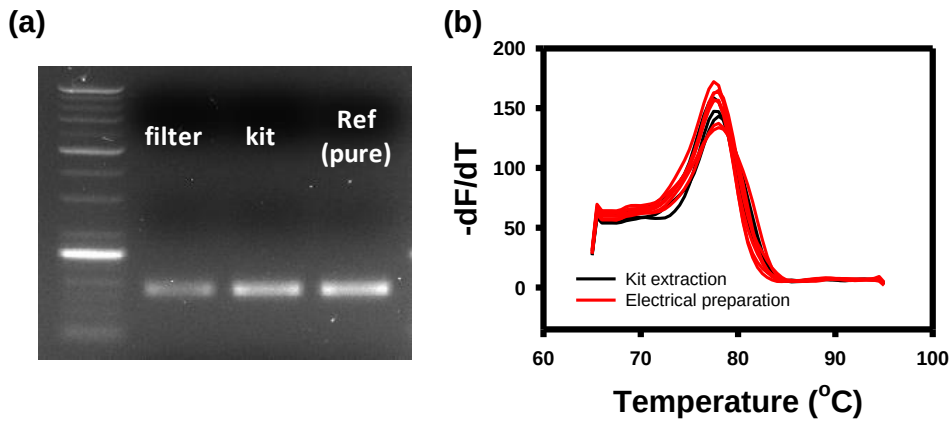

Figure 4-18 Validity check of the collected miRNA following RT-qPCR. (a) gel electrophoresis and (b) melting curve analysis of the miRNA collected using electrical preparation ('filter' in (a)) and kit extraction. Gel band of the pure miRNA amplicons is labeled 'Ref' in (a). (a) was adapted with permission from ref.[1] under the terms of the Creative Commons Attribution License (CC-BY). Copyright 2020 Lee *et al.*.

4.5.4 Yield and Purity Issues in the Electrophoretically Prepared miRNA from the Clinical Sample

4.5.4.1 Origin of the Low Electrophoretic Nucleic Acid Transport Yield

As the final discussion on the electrophoretic nucleic acid preparation method using the nanofilter membrane, the issues in yield and purity of the prepared miRNA should be examined. The yield and purity are current limitations of the electrophoretic preparation protocol, which should be studied and are being studied to improve the quality of the nucleic acid preparation.

In Figure 4−14, the transported amount of miRNA in 30 minutes was only ~5% of the input quantity. To find the origin of this low yield, the electrophoretic system was reconstructed as a circuit in Figure 4−19. Here, R_{res}, R_{col}, and R_{pore} indicate the resistances of the reservoir chamber, the collection chamber, and the nanofilter membrane, respectively. The electrode, specifically the electrical double layer (EDL) on the electrode surface, was modeled as a parallel alignment of a resistive term (R_{EDL}) and a capacitive component (C_{EDL}). The magnitudes of each electrical component could be calculated with the known dimensions and electrolyte conditions (R_{res}, R_{col}, and R_{pore}) or measuring the saturated ionic current. The time−dependent ionic current $I(t)$ and the saturated current $I(\infty)$ are expressed as Equation 4−5 and Equation 4−6:[57]

$$I(t) = \{I(0) - I(\infty)\} \exp\left\{-\left(\frac{1}{R_{EDL}C_{EDL}} + \frac{1}{(R_{res} + R_{col} + R_{pore})C_{EDL}}\right)t\right\} + I(\infty) \quad (4-5)$$

$$I(\infty) = V/(R_{EDL} + R_{res} + R_{col} + R_{pore}). \quad (4-6)$$

From resistance calculations and fitting the above equations to the ionic current measured at 2 V, R_{EDL}=1.13x10^5 Ω, $R_{res}+R_{col}$=1.23x10^4 Ω, and R_{pore}=39.8 Ω.

Therefore, at 2 V, R_{EDL} was the most dominant resistance in the total system, responsible for 90.2% of the total resistance. Accordingly, 90.2% of the electric voltage drop across the electrodes occurred at the EDL region, significantly reducing the effective driving force in the chambers and the nanofilter membrane. The electric field strength in the chambers and the nanofilter membrane was estimated by dividing the voltage drop at the resistance (V) to the length of the resistor (l): $E=V/l$. As a result, the electric field magnitude inside the nanoporous structure was 6.35x10^3 V/m, which was in a comparable electric field strength level to that of a conventional gel electrophoresis system (~100 V/10 cm). However, E inside the chambers was in a noticeably weak level, ~10 V/m, thus this weak E would have been the bottleneck for the miRNA transport to the collection chamber. The distance of electrophoretic travel during 30 min ($l_{EPH,30min}$) can be estimated as in Equation 4−7:

$$l_{\mathrm{EPH,30min}} = v_{\mathrm{EPH}}t = \mu_{\mathrm{DNA}}E(1800\ \mathrm{s}) \qquad (4-7)$$

where t is the time of travel (30 min=1800 s). According to the calculation and the chamber geometry (Figure 4−6(a)), the % of miRNA in the reservoir chamber that can reach the nanofilter membrane during 30 min was 6.2% at 2 V, close to the experimentally collected miRNA quantities in Figure 4−14.

From the simple electric circuit analysis, the source of the low transport yield in the electrophoretic system was identified as the large parasitic R_{EDL}. Pt electrode was favorable in the electrochemical aspect with its inertness, but at the same time, it was disadvantageous in promoting the miRNA transport to the collection chamber. Conversely, Ag/AgCl electrode is well known for its low parasitic resistance at EDL, but it reacts in the solution actively so that AgCl precipitates are formed during the experiment (section 4.3.1).

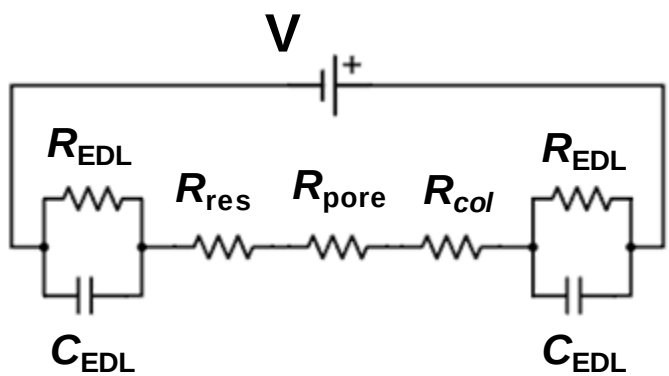

Figure 4-19 Electrical circuit model of the electrophoretic nucleic acid preparation system. Each electrical component is explained in the text. Figure was reproduced with permission from ref.[1] under the terms of the Creative Commons Attribution License (CC-BY). Copyright 2020 Lee *et al.*.

4.5.4.2 Low Optical Purity of the Electrophoretically Prepared Nucleic Acid from Protein Co-Migration

In UV-Vis spectrophotometry analysis, the absorbance plots of the electrophoretically and chemically prepared miRNA samples from the blood serum were obtained (Figure 4-20). The electrically collected solution exhibited an absorbance peak at 280 nm, representing the presence of protein in the buffer. In contrast, there was a peak at 270 nm in the absorbance profile of the conventionally prepared miRNA, indicating that phenol inserted in the serum during the conventional extraction process was incompletely washed out. [58] Phenol is a well-known PCR inhibitor,[59] so the residual phenol could have adversely affected RT-qPCR of the conventionally prepared miRNA in the previous section. Nevertheless, a peak at 260 nm indicating the nucleic acids was absent in both profiles presumably because the initial nucleic acid level in the serum was below the detection limit. A260/280 values, expressing relative nucleic acid purity to protein were 0.594 (electrophoretic preparation) and 1.72 (kit extraction).

From the absorbance analysis, it was experimentally proved that the electrophoretic nucleic acid preparation system was imperfect in eliminating proteins from the collected miRNA. Since the electrophoretic transport mechanism was universally applied to all charged particles in the sample, negatively charged proteins in blood serum were also driven across the nanofilter membrane in the same direction with miRNA. To completely separate the proteins with miRNA, reducing the size of the nanopores would be physically effective. In the array of small-sized nanopores, only nucleic acid molecules are allowed through the membrane by unthreading while the proteins would remain in the reservoir chamber. However, this is unpractical from the small difference in molecular dimensions of proteins and DNA or RNA strands; most proteins in blood serum are <10 nm in the diameter and the cross-section diameters of DNA or RNA strands are 1-2 nm.[60, 61] If the nanopores were to geometrically block the protein transport across the membrane, the pore size should be ~5 nm. Returning to the start point of this chapter,

fabricating a multiple nanopore array with a uniform size of ~5 nm is extremely difficult in the current technology. Therefore, the geometrical idea to prevent the protein co-migration with miRNA is invalid.

To summarize, the electrophoretic nucleic acid preparation technique currently has limitations of the low transport yield and the low purity of the collected nucleic acid in its current form. Nevertheless, in spite of the drawbacks, the effectivity of the electrophoretic preparation was still valid, as confirmed in the RT-qPCR and gel electrophoresis analysis from the previous sections.

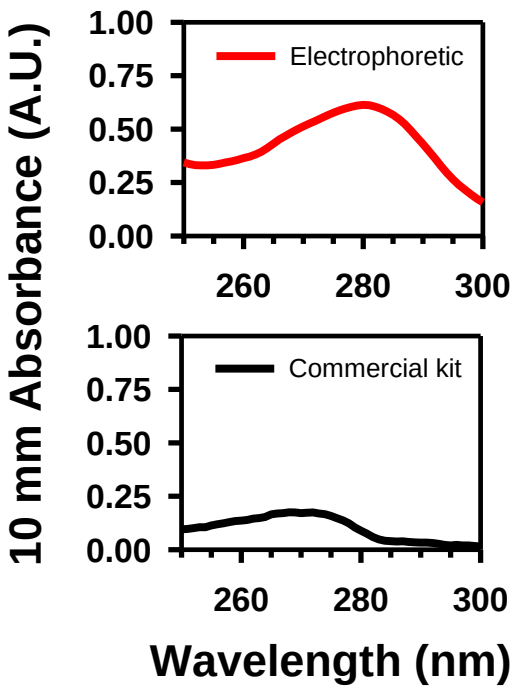

Figure 4-20 UV-Vis absorbance spectra of the electrophoretically prepared miRNA (top, red line) and the conventionally prepared miRNA (bottom, black line) from the blood serum. Figure was reproduced with permission from ref.[1] under the terms of the Creative Commons Attribution License (CC-BY). Copyright 2020 Lee *et al.*.

4.6 Conclusion

As an extension of the application of the fabricated nanoporous structure, the electrophoretic nucleic acid preparation system was designed and its operation was demonstrated using the clinical human blood serum. In the electrophoretic transport principle, the negatively charged nucleic acids were driven across the nanoporous structure, which served as a sieving media and paths of molecular transport. The principle was realized as a system incorporating chamber compartments, platinum electrodes, a DC electrical power supply, and the nanofilter membrane device. The device was fabricated based on the conventional solid-state nanopore fabrication technique and nanoimprint lithography technology to create a highly ordered network of uniform nanopores with ~100 nm membrane thickness.

The feasibility of the electrophoretic collection was studied in the proof-of-concept experiment, where miRNA mimic was successfully driven across the nanofilter membrane by the applied voltage. From data reproducibility and system stabilities, 2 V was selected as the optimized voltage condition for the electrical preparation. The same system was also successful and efficient in preparing miRNA from the human blood serum, demonstrating itself as a simple and effective sample pre-treatment process.

The significance of the electrophoretic nucleic acid preparation system can be found in its superior efficiency and simplicity in operation to the conventional, column-based method. The comparison of the electrophoretic method and the conventional protocol is summarized in Table 4-5. By simply plugging in electrical voltage to the chambers, the biosample pre-treatment can be completed in only half an hour with minimal operations. In addition, the new method can be further simplified by replacing the DC power supply with household batteries. Therefore, the physics-based protocol has potential as easy access, on-site nucleic acid preparation protocol, bringing out the laboratory procedure to the real world.

Commercial kit		Electrophoretic preparation
10+	Steps	3 (setup−run−collect)
1−1.5 hr	Operation time	0.5 hr
Centrifuge, column, phenol, chloroform, washing buffers	Device, reagent	DC power supply, device, flow cell, electrode
Comparable	Performance	Comparable
Phenol	Major contaminant	Protein
Well−established method	Advantage	Simple step and setup
Complex, chemically hazardous	Disadvantage	Low yield and purity

Table 4−5 Comparison of the conventional nucleic acid extraction method using commercial kits and the electrophoretic preparation method.

References

1. Lee, K.; Kang, J.; Kim, H.-M.; Ahn, J.; Lim, H.; Lee, J.; Jeon, W.-J.; Lee, J.-H.; Kim, K.-B., Direct Electrophoretic microRNA Preparation from Clinical Samples using Nanofilter Membrane. *Nano Convergence* 2020, *accepted*.

2. Lee, K.; Park, K. B.; Kim, H. J.; Yu, J. S.; Chae, H.; Kim, H. M.; Kim, K. B., Recent Progress in Solid-State Nanopores. *Advanced Materials* 2018, *30* (42), 1704680.

3. Yu, J.-S.; Hong, S. C.; Wu, S.; Kim, H.-M.; Lee, C.; Lee, J.-S.; Lee, J. E.; Kim, K.-B., Differentiation of selectively labeled peptides using solid-state nanopores. *Nanoscale* 2019, *11* (5), 2510-2520.

4. Yu, J.-S.; Lim, M.-C.; Huynh, D. T. N.; Kim, H.-J.; Kim, H.-M.; Kim, Y.-R.; Kim, K.-B., Identifying the Location of a Single Protein along the DNA Strand Using Solid-State Nanopores. *ACS Nano* 2015, *9* (5), 5289-5298.

5. Kwak, D. K.; Chae, H.; Lee, M. K.; Ha, J. H.; Goyal, G.; Kim, M. J.; Kim, K. B.; Chi, S. W., Probing the Small-Molecule Inhibition of an Anticancer Therapeutic Protein-Protein Interaction Using a Solid-State Nanopore. *Angewandte Chemie International Edition in English* 2016, *55* (19), 5713-7.

6. Chae, H.; Kwak, D.-K.; Lee, M.-K.; Chi, S.-W.; Kim, K.-B., Solid-state nanopore analysis on conformation change of p53TAD–MDM2 fusion protein induced by protein–protein interaction. *Nanoscale* 2018, *10* (36), 17227-17235.

7. Chen, P.; Mitsui, T.; Farmer, D. B.; Golovchenko, J.; Gordon, R. G.; Branton, D., Atomic layer deposition to fine-tune the surface properties and diameters of fabricated nanopores. *Nano Letters* 2004, *4* (7), 1333-1337.

8. Torsten, S.; Miao, Z.; Ilya, S.; Niclas, R.; Jan, L., Nanopore arrays in a silicon membrane for parallel single-molecule detection: fabrication. *Nanotechnology* 2015, *26* (31), 314001.

9. Nam, S.-W.; Rooks, M. J.; Kim, K.-B.; Rossnagel, S. M., Ionic Field Effect Transistors with Sub-10 nm Multiple Nanopores. *Nano Letters* 2009, *9* (5), 2044-2048.

10. Larkin, J.; Foquet, M.; Turner, S. W.; Korlach, J.; Wanunu, M., Reversible Positioning of Single Molecules inside Zero-Mode Waveguides. *Nano Letters* 2014, *14* (10), 6023-6029.

11. Larkin, J.; Henley, R. Y.; Jadhav, V.; Korlach, J.; Wanunu, M., Length-independent DNA packing into nanopore zero-mode waveguides for low-input DNA sequencing. *Nat. Nanotechnol.* 2017, *12* (12), 1169.

12. Jadhav, V.; Hoogerheide, D. P.; Korlach, J.; Wanunu, M., Porous Zero-Mode Waveguides for Picogram-Level DNA Capture. *Nano Letters* 2019, *19* (2), 921-929.

13. Yang, Q.; Lin, X.; Su, B., Molecular Filtration by Ultrathin and Highly Porous Silica Nanochannel Membranes: Permeability and Selectivity. *Analytical Chemistry* 2016, *88* (20), 10252-10258.

14. Chun, K.-Y.; Mafé, S.; Ramírez, P.; Stroeve, P., Protein transport through gold-coated, charged nanopores: Effects of applied voltage. *Chemical Physics Letters* 2006, *418* (4), 561-564.

15. O'Connor, A. J.; Pratt, H. R. C.; Stevens, G. W., Electrophoretic mobilities of proteins and protein mixtures in porous membranes. *Chemical Engineering Science* 1996, *51* (13), 3459-3477.

16. Stellwagen, N. C.; Gelfi, C.; Righetti, P. G., The free solution mobility of DNA. *Biopolymers* 1997, *42* (6), 687-703.

17. Ware, B. R.; Flygare, W. H., The simultaneous measurement of the electrophoretic mobility and diffusion coefficient in bovine serum albumin solutions by light scattering. *Chemical Physics Letters* 1971, *12* (1), 81-85.

18. Allison, S. A.; Potter, M.; McCammon, J. A., Modeling the electrophoresis of lysozyme. II. Inclusion of ion relaxation. *Biophysical journal* 1997, *73* (1), 133-140.

19. Stellwagen, E.; Stellwagen, N. C., Determining the electrophoretic mobility and translational diffusion coefficients of DNA molecules in free solution. *Electrophoresis* 2002, *23* (16), 2794-2803.

20. Manz, A.; Graber, N.; Widmer, H. M., Miniaturized total chemical analysis systems: A novel concept for chemical sensing.

Sensors and Actuators B: Chemical 1990, *1* (1), 244-248.

21. Price, C. W.; Leslie, D. C.; Landers, J. P., Nucleic acid extraction techniques and application to the microchip. *Lab on a Chip* 2009, *9* (17), 2484-2494.

22. McCormick, R. M., A solid-phase extraction procedure for DNA purification. *Analytical Biochemistry* 1989, *181* (1), 66-74.

23. Arpino, J. A. J.; Rizkallah, P. J.; Jones, D. D., Crystal Structure of Enhanced Green Fluorescent Protein to 1.35 Å Resolution Reveals Alternative Conformations for Glu222. *PLOS ONE* 2012, *7* (10), e47132.

24. Siqueiros-Cendón, T.; Arévalo-Gallegos, S.; Iglesias-Figueroa, B. F.; García-Montoya, I. A.; Salazar-Martínez, J.; Rascón-Cruz, Q., Immunomodulatory effects of lactoferrin. *Acta Pharmacologica Sinica* 2014, *35* (5), 557-566.

25. Rudi, K.; Jakobsen, K. S., Overview of DNA Purification for Nucleic Acid-Based Diagnostics From Environmental and Clinical Samples. In *Diagnostic Bacteriology Protocols*, O'Connor, L., Ed. Humana Press: Totowa, NJ, 2006; pp 23-35.

26. Moldovan, L.; Batte, K. E.; Trgovcich, J.; Wisler, J.; Marsh, C. B.; Piper, M., Methodological challenges in utilizing miRNAs as circulating biomarkers. *Journal of Cellular and Molecular Medicine* 2014, *18* (3), 371-390.

27. Altayari, W., DNA Extraction: Organic and Solid-Phase. In *Forensic DNA Typing Protocols*, Goodwin, W., Ed. Springer New York: New York, NY, 2016; pp 55-68.

28. miRNeasy Serum/Plasma Handbook. Qiagen: 2012.

29. Tan, S. C.; Yiap, B. C., DNA, RNA, and protein extraction: the past and the present. *BioMed Research International* 2009, *2009*, 574398.

30. Christel, L. A.; Petersen, K.; McMillan, W.; Northrup, M. A., Rapid, Automated Nucleic Acid Probe Assays Using Silicon Microstructures for Nucleic Acid Concentration. *Journal of Biomechanical Engineering* 1999, *121* (1), 22-27.

31. Hagan, K. A.; Bienvenue, J. M.; Moskaluk, C. A.; Landers,

J. P., Microchip-Based Solid-Phase Purification of RNA from Biological Samples. *Analytical Chemistry* 2008, *80* (22), 8453-8460.

32. Breadmore, M. C., *et al.*, Microchip-Based Purification of DNA from Biological Samples. *Analytical Chemistry* 2003, *75* (8), 1880-1886.

33. Kim, J.; Johnson, M.; Hill, P.; Gale, B. K., Microfluidic sample preparation: cell lysis and nucleic acidpurification. *Integrative Biology* 2009, *1* (10), 574-586.

34. Kim, C.-J.; Park, J.; Sunkara, V.; Kim, T.-H.; Lee, Y.; Lee, K.; Kim, M.-H.; Cho, Y.-K., Fully automated, on-site isolation of cfDNA from whole blood for cancer therapy monitoring. *Lab on a Chip* 2018, *18* (9), 1320-1329.

35. Sonnenberg, A., *et al.*, Rapid Electrokinetic Isolation of Cancer-Related Circulating Cell-Free DNA Directly from Blood. *Clinical Chemistry* 2014, *60* (3), 500-509.

36. Sonnenberg, A.; Marciniak, J. Y.; Skowronski, E. A.; Manouchehri, S.; Rassenti, L.; Ghia, E. M.; Widhopf, G. F.; Kipps, T. J.; Heller, M. J., Dielectrophoretic isolation and detection of cancer-related circulating cell-free DNA biomarkers from blood and plasma. *Electrophoresis* 2014, *35* (12-13), 1828-1836.

37. Sonnenberg, A.; Marciniak, J. Y.; McCanna, J.; Krishnan, R.; Rassenti, L.; Kipps, T. J.; Heller, M. J., Dielectrophoretic isolation and detection of cfc-DNA nanoparticulate biomarkers and virus from blood. *Electrophoresis* 2013, *34* (7), 1076-1084.

38. Atkins, P.; De Paula, J., *Atkins' Physical Chemistry*. 8th ed.; Oxford University Press: Oxford, 2006.

39. Lee, J.; Park, S.; Choi, K.; Kim, G., Nano-scale patterning using the roll typed UV-nanoimprint lithography tool. *Microelectronic Engineering* 2008, *85* (5), 861-865.

40. Ahn, J.; Kwon, S.; Jung, S.; Lee, W. S.; Jeong, J.; Lim, H.; Shin, Y.-B.; Lee, J., Fabrication of Pyrrole-Based Electrochemical Biosensor Platform Using Nanoimprint Lithography. *Advanced Materials Interfaces* 2018, *5* (8), 1701593.

41. Lee, T.; Wi, J.-S.; Oh, A.; Na, H.-K.; Lee, J.; Lee, K.; Lee, T. G.; Haam, S., Highly robust, uniform and ultra-sensitive

surface-enhanced Raman scattering substrates for microRNA detection fabricated by using silver nanostructures grown in gold nanobowls. *Nanoscale* 2018, *10* (8), 3680-3687.

42. de Planell-Saguer, M.; Rodicio, M. C., Detection methods for microRNAs in clinic practice. *Clinical Biochemistry* 2013, *46* (10), 869-878.

43. Taft, R. J.; Pang, K. C.; Mercer, T. R.; Dinger, M.; Mattick, J. S., Non-coding RNAs: regulators of disease. *Journal of Pathology* 2010, *220* (2), 126-139.

44. Fang, L.*, et al.*, MicroRNA miR-93 promotes tumor growth and angiogenesis by targeting integrin-β8. *Oncogene* 2010, *30*, 806.

45. Larrea, E.*, et al.*, New Concepts in Cancer Biomarkers: Circulating miRNAs in Liquid Biopsies. *Int. J. Mol. Sci.* 2016, *17* (5), 627.

46. Izzotti, A.; Carozzo, S.; Pulliero, A.; Zhabayeva, D.; Ravetti, J. L.; Bersimbaev, R., Extracellular MicroRNA in liquid biopsy: applicability in cancer diagnosis and prevention. *American Journal of Cancer Research* 2016, *6* (7), 1461-1493.

47. Tissot, C.*, et al.*, Circulating free DNA concentration is an independent prognostic biomarker in lung cancer. *European Respiratory Journal* 2015, *46* (6), 1773-1780.

48. Phallen, J.*, et al.*, Direct detection of early-stage cancers using circulating tumor DNA. *Science Translational Medicine* 2017, *9* (403), eaan2415.

49. Pfaffl, M. W., A new mathematical model for relative quantification in real-time RT–PCR. *Nucleic Acids Res.* 2001, *29* (9), e45-e45.

50. Porterfield, J. Z.; Zlotnick, A., A simple and general method for determining the protein and nucleic acid content of viruses by UV absorbance. *Virology* 2010, *407* (2), 281-288.

51. Wilfinger, W. W.; Mackey, K.; Chomczynski, P., Effect of pH and Ionic Strength on the Spectrophotometric Assessment of Nucleic Acid Purity. *BioTechniques* 1997, *22* (3), 474-481.

52. Crowley, E.; Di Nicolantonio, F.; Loupakis, F.; Bardelli, A.,

Liquid biopsy: monitoring cancer-genetics in the blood. *Nature Reviews Clinical Oncology* 2013, *10* (8), 472-484.

53. Heitzer, E.; Ulz, P.; Geigl, J. B., Circulating Tumor DNA as a Liquid Biopsy for Cancer. *Clinical Chemistry* 2015, *61* (1), 112-123.

54. Xue, X.; Wang, X.; Zhao, Y.; Hu, R.; Qin, L., Exosomal miR-93 promotes proliferation and invasion in hepatocellular carcinoma by directly inhibiting TIMP2/TP53INP1/CDKN1A. *Biochemical and Biophysical Research Communications* 2018, *502* (4), 515-521.

55. Ali, H. E. A.; Abdel Hameed, R.; Effat, H.; Ahmed, E. K.; Atef, A. A.; Sharawi, S. K.; Ali, M.; Abd Elmageed, Z. Y.; Abdel Wahab, A. H., Circulating microRNAs panel as a diagnostic tool for discrimination of HCV-associated hepatocellular carcinoma. *Clinics and Research in Hepatology and Gastroenterology* 2017, *41* (4), e51-e62.

56. Farina, N. H.; Wood, M. E.; Perrapato, S. D.; Francklyn, C. S.; Stein, G. S.; Stein, J. L.; Lian, J. B., Standardizing Analysis of Circulating MicroRNA: Clinical and Biological Relevance. *Journal of Cellular Biochemistry* 2014, *115* (5), 805-811.

57. Smeets, R. M.; Keyser, U. F.; Dekker, N. H.; Dekker, C., Noise in solid-state nanopores. *Proceedings of the National Academy of Sciences of the United States of America* 2008, *105* (2), 417-21.

58. Thermo Scientific NanoDrop Spectrophotometers User Manual. Thermo Fisher Scientific: 2010.

59. Schrader, C.; Schielke, A.; Ellerbroek, L.; Johne, R., PCR inhibitors – occurrence, properties and removal. *Journal of Applied Microbiology* 2012, *113* (5), 1014-1026.

60. Leeman, M.; Choi, J.; Hansson, S.; Storm, M. U.; Nilsson, L., Proteins and antibodies in serum, plasma, and whole blood—size characterization using asymmetrical flow field-flow fractionation (AF4). *Anal. Bioanal. Chem.* 2018, *410* (20), 4867-4873.

61. Steinbock, L. J.; Krishnan, S.; Bulushev, R. D.; Borgeaud, S.; Blokesch, M.; Feletti, L.; Radenovic, A., Probing the size of proteins with glass nanopores. *Nanoscale* 2014, *6* (23), 14380-7.

Chapter 5

Conclusion

In this work, sensitivity and device reliability issues in the solid-state nanopore platform were discussed with a new application of nanopores and nanopore-related devices, all in relation to electrokinetics in DNA transport. Although the subjects have continuously been studied in the nanopore research field, the previous works were reported based on simple and empirical ideas that a more systematic and physical approach was still in need.

To enhance the DNA sensitivity of solid-state nanopore, a structural modification of the guide structure was introduced to the device. From the experiment, ΔG and t_d of DNA translocation signals through the guide-inserted nanopore device increased from those in the conventional nanopore device. Explaining the experimental result, the role of the guide structure was successfully identified in the electrokinetics simulations using FEM. The guide structure provided an extra geometric hindrance to the ion movement by the DNA segments inside the guide structure, increasing ΔG. A strong electroosmotic flow generated inside the guide structure acted as an extra drag on the remaining DNA parts to slow down its translocation.

In improving the reliability of the nanopore device against nonspecific DNA surface adsorptions, the plasma polymerization strategy was adopted to deposit PEG on the nanopore membrane. The gas-phase deposition was advantageous in terms of fabrication efficiency, controllability, and reproducibility over the self-assembly method conventionally used to create polymer-functionalized nanopores. The time to adsorption concept was introduced, which better reflected the real nanopore experiment situations in evaluating the reliability of the device than the maximum device operation times discussed in the previous reports. The polymer-coated surface was ~2 times more resistant to DNA adsorptions during nanopore detections owing to the repulsive nature of PP-PEG against DNA. Furthermore, surface interaction modes of PP-PEG and SiN_x with DNA were taken into consideration in the physical study of the DNA adsorptions near a nanopore and in the analysis of DNA translocation behavior on the different surfaces.

Following the nanopore multiplexing trend in the application field of the solid-state nanopore platform, the electrophoretic nucleic acid preparation system using the nanofilter membrane device was proposed. The goal of the system was to electrically enrich nucleic acid from a biosample, suppressing the transport of other particles having positive charges or sizes larger than the nanoporous structure. The principle and the stability of the electrophoretic enrichment system were validated experimentally using short miR93-5p. Lastly, its applicability to clinical blood serum samples and compatibility to qPCR were confirmed in the liquid biopsy demonstration using the electrophoretic nucleic acid preparation system.

This thesis pursued to maintain physical and electrokinetic point of view as best as possible in understanding DNA translocation in nanopores and in developing the new application of the nanoporous structure. Undoubtedly, all three suggestions made in this thesis require future works to improve and practically utilize the modified devices and the system. For instance, more delicate design on the electroosmotic flow in the *cis* chamber could be attempted for fine control of the DNA translocation speed. Likewise, the fabrication conditions of the PP-PEG deposited nanopore device would be fine-tuned so that the device performances, including antifouling property and the electrical noise, could be further enhanced. Last but not least, the transport yield and the purity of the collected nucleic acid must be greatly improved for the electrophoretic preparation system to be utilized in practice. Yet, the three sets of analyses were successful in suggesting the physical ideas and approaches, covering a wide range in solid-state nanopore research.

국 문 초 록

본 학위논문에서는 솔리드 스테이트 나노포어(solid-state nanopore, 나노포어) 분야의 현존하는 세 가지 쟁점에 대해 논의하고 이에 대한 접근법으로 DNA 의 전기동역학적인 이동에 대한 물리적인 분석을 채택하였다. 현재 활발히 연구가 진행되고 있는 솔리드 스테이트 나노포어의 세부분야는 (1) DNA 감도 향상, (2) 소자 신뢰성 강화, 그리고 (3) 전기적 감지 외에 솔리드 스테이트 나노포어 및 파생된 시스템의 다른 활용 분야를 찾는 것이다. 위의 이슈에 대한 기존의 연구 결과들과 소자의 노이즈에 관련된 연구 결과들을 본 학위논문에 요약하였다. 한편 기존 연구들은 주로 비교적 간단하거나 실험적인 접근에서 이루어진 것이므로, 솔리드 스테이트 나노포어 플랫폼의 성능을 향상하기 위한 체계적이며 물리적인 연구가 지속적으로 필요한 상황이다.

이에 첫째로, 나노포어의 DNA 감도를 향상하기 위해 '가이드 구조물' 로 명명된 구조를 기존의 나노포어에 삽입한 새로운 소자가 제작되었다. 또한 이 구조물이 나노포어를 통한 DNA 분자 이동(translocation)에 미치는 영향을 파악하기 위해 유한요소해석법을 이용한 전기동역학적 시뮬레이션을 수행하였다. DNA 감도 향상은 translocation 시그널의 크기(ΔG) 및 지속 시간(t_d)의 증가를 목적으로 하게 되는데, 가이드 구조물이 삽입된 경우에는 두 목표를 모두 달성할 수 있었다. 구체적으로, DNA가 나노포어를 통과할 때 가이드 구조물 내에 잔존하는 DNA의 부분들이 이온의 흐름을 추가적으로 방해해서 시그널 크기가 증가하였다. 그리고 시뮬레이션으로부터 가이드 구조물 내에는 강한 전기 삼투 유동(electroosmosis flow)이 DNA 이동의 역방향으로 발생하며, 이 유동이 DNA의 나노포어 통과 중에 속도를 늦추는 요소로 작용하였음도 밝혔다.

둘째로, 소자의 신뢰성과 관련된 기존 연구 결과에서 발전하여 본 연구에서는 poly(ethylene glycol)(PEG)이 액상의 자가조립법 대신 기상의 플라즈마 중합 방식으로 나노포어 멤브레인 위에 증착되었다. 기상 증착 방식은 액상 코팅법에 비해 작업의 효율, 작업 상의 조절, 재현성 등의 측면에서 장점을 가지고 있음이 알려져 있다. 플라즈마 중합 PEG(PP-PEG)와 일반 실리콘 나이트라이드(SiN_x) 표면의 DNA 흡착 방지 특성을 실제 나노포어 실험 상황을 고려해 평가하기 위해

time to adsorption 이라는 새 개념을 고안하고 도입하였다. 그 결과, PP-PEG 표면이 코팅된 경우 약 2 배 더 긴 시간 동안 DNA 의 표면 흡착 없이 실험이 가능했다. 여기에는 DNA 와 PP-PEG 간의 서로 밀어내는 상호 작용력이 영향을 주었으며, 이 상호 작용은 DNA translocation 시그널 상의 변화를 일으키기도 하였다. 여기에 더하여 상호 작용력을 고려해 나노포어 표면에 DNA가 흡착되는 현상을 물리적 및 미시적으로 분석하였다.

셋째로, DNA 가 전기적으로 나노포어를 통과하는 것으로부터 파생하여 새로운 바이오시료 전처리 방법인 전기영동 핵산 추출법을 고안하였다. 이 방법에서는 바이오시료 속 핵산이 공정을 통해 제작된 나노 다공성 막을 통해 전기적으로 이동하게 되며, 반대로 양의 전하를 띠거나 막의 구멍보다 더 큰 입자들은 막의 반대편으로 이동하지 못하게 된다. 이 원리를 구현하는 시스템을 마련한 이후, 전기영동 핵산 추출의 원리를 microRNA 를 사용한 실험을 통해 확인하였고 시스템의 안정성 또한 확보하였다. 여기에 더하여 사람의 혈청 샘플을 이용한 액상 생검의 시연을 통해 전기영동 핵산 추출법의 실용성을 평가하였다.

본 학위논문은 솔리드 스테이트 나노포어를 통과하는 DNA 의 전기적인 움직임을 물리적 및 구조적으로 이해하고, 그 이해를 바탕으로 해당 시스템의 새로운 활용을 고안하였다. 반대로 솔리드 스테이트 나노포어 성능의 체계적인 변화와 개선을 위해서는 DNA 의 전기적인 이동에 미치는 물리적인 영향들을 분석하는 것이 중요하다는 점이 본 학위논문의 논의를 통해 드러났다.